

1-1-2000

Comparative study of zinc bis-quinolates and lithium mono-quinolates: Investigation of the effect of coordination geometry on electroluminescence performance

Flocerfida Lalo Endrino
University of Nevada, Las Vegas

Follow this and additional works at: <https://digitalscholarship.unlv.edu/rtds>

Repository Citation

Endrino, Flocerfida Lalo, "Comparative study of zinc bis-quinolates and lithium mono-quinolates: Investigation of the effect of coordination geometry on electroluminescence performance" (2000). *UNLV Retrospective Theses & Dissertations*. 1242.
<http://dx.doi.org/10.25669/gzon-8670>

This Thesis is protected by copyright and/or related rights. It has been brought to you by Digital Scholarship@UNLV with permission from the rights-holder(s). You are free to use this Thesis in any way that is permitted by the copyright and related rights legislation that applies to your use. For other uses you need to obtain permission from the rights-holder(s) directly, unless additional rights are indicated by a Creative Commons license in the record and/or on the work itself.

This Thesis has been accepted for inclusion in UNLV Retrospective Theses & Dissertations by an authorized administrator of Digital Scholarship@UNLV. For more information, please contact digitalscholarship@unlv.edu.

INFORMATION TO USERS

This manuscript has been reproduced from the microfilm master. UMI films the text directly from the original or copy submitted. Thus, some thesis and dissertation copies are in typewriter face, while others may be from any type of computer printer.

The quality of this reproduction is dependent upon the quality of the copy submitted. Broken or indistinct print, colored or poor quality illustrations and photographs, print bleedthrough, substandard margins, and improper alignment can adversely affect reproduction.

In the unlikely event that the author did not send UMI a complete manuscript and there are missing pages, these will be noted. Also, if unauthorized copyright material had to be removed, a note will indicate the deletion.

Oversize materials (e.g., maps, drawings, charts) are reproduced by sectioning the original, beginning at the upper left-hand corner and continuing from left to right in equal sections with small overlaps.

Photographs included in the original manuscript have been reproduced xerographically in this copy. Higher quality 6" x 9" black and white photographic prints are available for any photographs or illustrations appearing in this copy for an additional charge. Contact UMI directly to order.

ProQuest Information and Learning
300 North Zeeb Road, Ann Arbor, MI 48106-1346 USA
800-521-0600

UMI[®]

COMPARATIVE STUDY OF ZINC BIS-QUINOLATES AND LITHIUM MONO-
QUINOLATES: INVESTIGATION OF THE EFFECT OF COORDINATION
GEOMETRY ON ELECTROLUMINESCENCE PERFORMANCE

by

Flocerfida Endrino

Bachelor of Science
University of Nevada, Las Vegas
1999

A thesis submitted in partial fulfillment
of the requirements for the

Master of Science Degree
Department of Chemistry
College of Sciences

Graduate College
University of Nevada, Las Vegas
May 2001

UMI Number: 1405099

Copyright 2001 by
Endrino, Flocerfida Lalo

All rights reserved.

UMI[®]

UMI Microform 1405099

Copyright 2001 by Bell & Howell Information and Learning Company.

All rights reserved. This microform edition is protected against
unauthorized copying under Title 17, United States Code.

Bell & Howell Information and Learning Company
300 North Zeeb Road
P.O. Box 1346
Ann Arbor, MI 48106-1346



Thesis Approval
The Graduate College
University of Nevada, Las Vegas

April 20 , 2001

The Thesis prepared by

Flocerfida Lalo Endrino

Entitled

Comparative study of Zinc Bis-Quinolinolato and Lithium

Mono-Quinolinolates: Investigation of the Effect of

Coordination Geometry on Electroluminescence Performance.

is approved in partial fulfillment of the requirements for the degree of

Master of Science

Examination Committee Chair

Dean of the Graduate College

Examination Committee Member

Examination Committee Member

Graduate College Faculty Representative

ABSTRACT

Comparative Study of Zinc Bis-Quinolates and Lithium Mono-Quinolates: Investigation of the Effect of Coordination Geometry on Electroluminescence Performance

By

Flocerfida Endrino

Dr. Linda S. Sapochak, Examination Committee Chair
Assistant Professor of Chemistry
University of Nevada, Las Vegas

Metal (8-quinolinolato) (Mq_n) chelates have proven to be viable for use in organic light-emitting devices (OLEDs), both as the active emitter layer and as the electron-transporting host in dye-doped OLEDs. Whether serving as the emitter layer or host material the energy level-alignment affecting charge injection efficiency and charge mobility properties are of equal importance. Substitution of the 8-quinolinolato ligand or substitution of different metal ions has been shown to shift absorption and emission energies, which can modify the relative energy level alignments of the HOMO and LUMO levels at charge injection interfaces in an OLED. Furthermore, substitution of metal ions of different oxidation states will result in differing coordination geometries of the resulting metal chelates. For Alq_3 , the electron transport properties and the good thermal stability of vapor-deposited films have been attributed to its octahedral geometry. In this work, we present a comparative study of the photophysical (absorption and emission) properties and thermal stability properties of methylated zinc bis-quinolates and lithium mono-quinolates.

Results are related to aluminum tris-quinolates and implications on electroluminescence performance will be discussed.

TABLE OF CONTENTS

ABSTRACT.....	iii
LIST OF FIGURES	vii
LIST OF TABLES.....	ix
ACKNOWLEDGEMENTS.....	x
CHAPTER 1 ORGANIC ELECTROLUMINESCENCE.....	1
1.1 Introduction.....	1
1.2 Background.....	3
1.3 Previous Studies of Znq ₂ and Liq Materials	10
CHAPTER 2 MATERIAL SYNTHESIS AND CHARACTERIZATION.....	16
2.1 Synthesis of metal 8-quinolinolato chelates	16
2.2 Material characterization	20
2.3 Synthetic procedures.....	35
CHAPTER 3 X-RAY ABSORPTION SPECTROSCOPIC CHARACTERIZATION ...	42
3.1 Background.....	42
3.2 Introduction.....	43
3.3 Experimental method.....	45
3.4 Results and discussions.....	47
CHAPTER 4 PHOTOPHYSICAL STUDIES OF METAL CHELATES.....	57
4.1 Introduction.....	57
4.2 Experimental	59
4.3 Absorption spectroscopic results	60
4.4 Photoluminescence spectroscopic results	65
4.5 Discussion and conclusions	69
CHAPTER 5 ELECTROLUMINESCENCE DATA	72
5.1 Device fabrication.....	72
5.2 Device testing.....	74
5.3 Calculation of electroluminescence and power efficiencies	74
5.4 Electroluminescence results.....	75
CHAPTER 6 CONCLUSIONS	87

APPENDIX I FT-IR DATA	90
APPENDIX II THERMAL PROPERTIES DATA	91
APPENDIX III PHOTOPHYSICAL DATA.....	100
APPENDIX IV DEVICE PROPERTIES	106
APPENDIX V ¹ H-NMR DATA	112
VITA	114

LIST OF FIGURES

1.1	Aluminum Tris (8-Quinolinolato) (Alq_3).....	2
1.2	Organic Light Emitting Device.....	2
1.3	Proposed mechanism of organic electroluminescence	4
2.1	General synthetic scheme for zinc bis (8-quinolinolato) chelates	17
2.2	Synthesized zinc (8-quinolinolato) chelates	18
2.3	General synthetic scheme for lithium bis (8-quinolinolato) chelates	19
2.4	Synthesized lithium (8-quinolinolato) chelates	20
2.5	Interpretation for 2 sets of quinolate ligands arising in different solvents.....	21
2.6	FT-IR spectra of Znq_2	25
2.7	FT-IR spectra of Liq	25
2.8	DSC scans of Alq_3 and Znq_2 showing endothermic and exothermic scans.....	30
2.9	First and second heating cycles of Zinc bis (8-quinolinolato) chelates.....	31
2.10	Cyclic voltammograms for Alq_3 and Znq_2	35
3.1	C1s NEXAFS spectra of Alq_3 and Znq_2	49
3.2	Illustration of the effects of metal ion substitution on the electron distribution of the quinolate ligand	49
3.3	Schematic representation of the metal ligand (M-q) bonding character.....	50
3.4	C 1s and N 1s NEXAFS spectra of $nMeq_2 Znq_2$	51
3.5	C 1s and N 1s NEXAFS spectra of $nMeqLi$	54
3.6	O 1s NEXAFS spectra of $nMeqLi$	54
4.1	Absorption spectra of Mq_n in $CH_2 Cl_2$ and DMF	62
4.2	Absorption spectra of $nMeq_2 Zn$ and $nMeqLi$ in $CH_2 Cl_2$	63
4.3	Absorption spectra of $nMeq_2 Zn$ and $nMeqLi$ in DMF	64
4.4	Emission spectra of $nMeq_2 Zn$ in DMF	68
4.5	Emission spectra of $nMeqLi$ in DMF	68
5.1	Schematic representation of an organic light emitting device	73
5.2	α -NPD.....	73
5.3	IV Curve for $nMeq_2 Zn$ and Alq_3 as a reference.....	77
5.5	Light output vs. current for $nMeq_2 Zn$ and Alq_3 as a reference	78
5.5	IV Curve for $nMeq_3 Al$	78
5.6	Light Output vs. current for $nMeq_3 Al$	79
A-1	FT-IR spectra of Znq_2	91
A-2	FT-IR spectrum of $2Meq_2 Zn$	91
A-3	FT-IR spectra of $4Meq_2 Zn$	92
A-4	FT-IR spectra of $5Meq_2 Zn$	92
A-5	FT-IR spectra of Liq	93
A-6	FT-IR spectra of $4MeqLi$	93
A-7	FT-IR spectra of $5MeqLi$	94
B-1	Decomposition Temperature for Znq_2	96
B-2	Decomposition Temperature for $2Meq_2 Zn$	96

B-3	Decomposition Temperature for 4Meq ₂ Zn.....	97
B-4	Decomposition Temperature for 5Meq ₂ Zn.....	97
B-5	Decomposition Temperature for Liq.....	98
B-6	Decomposition Temperature for 4meqLi.....	98
B-7	Decomposition Temperature for 5MeqLi.....	99
B-8	DSC traces of first and second heating dynamic of nMeqLi.....	99
C-1	Absorbance spectra of nMeq ₂ Zn in MeOH.....	101
C-2	Absorbance spectra of nMeq ₂ Zn on film.....	101
C-3	Absorbance spectra of Liq on film.....	102
C-4	Emission spectra of nMeq ₂ Zn in CH ₂ Cl ₂	102
C-5	Emission spectra of nMeq ₂ Zn in MeOH.....	103
C-6	Emission spectra of nMeq ₂ Zn on film.....	103
C-7	Emission spectra of nMeqLi in CH ₂ Cl ₂	104
C-8	Emission spectra of nMeqLi in DMF.....	104
C-9	Emission spectra of nMeqLi on film.....	105
C-10	Absorption spectra of q and q ⁻ in DMF.....	105
D-1	IV curve for Znq ₂	107
D-2	IV curve for 2Meq ₂ Zn.....	107
D-3	IV curve for 4Meq ₂ Zn.....	108
D-4	IV curve for 5Meq ₂ Zn.....	108
D-5	Light output vs. current for Znq ₂	109
D-6	Light output vs. current for 2Meq ₂ Zn.....	109
D-7	Light output vs. current for 4Meq ₂ Zn.....	110
D-8	Light output vs. current for 5Meq ₂ Zn.....	110
D-9	IV curve for Alq ₃	111
D-10	Light output vs. current for Alq ₃	111
E-1	¹ H-NMR chemical shifts in ppm and coupling constants for nMeq and nMeqLi in DMSO-d ₆	113
E-2	¹ H-NMR chemical shifts in ppm and coupling constants for q and Liq in CDCl ₃	113

LIST OF TABLES

2.1	¹ H NMR Chemical shifts in ppm for Znq ₂	22
2.2	¹ H-NMR Chemical shifts in ppm for nMeq and nMeqLi in DMSO-d ₆	22
2.3	¹ H-NMR Chemical shifts in ppm for Liq and q in CDCl ₃	23
2.3	Chemical Shift change between 8-quinolinol and Liq in DMSO-d ₆ and CDCl ₃ .	24
2.4	Assignments of FT-IR peaks for zinc bis(8-quinolinolato)	26
2.5	Assignments of FT-IR peaks for zinc bis(8-quinolinolato)	26
2.6	Thermal analysis results.....	28
2.7	HOMO/LUMO levels and redox potentials of Alq ₃ and Znq ₂	34
3.1	C 1s NEXAFS Data for Mq _n chelates.....	50
3.2	C 1s NEXAFS Data for nMeq ₂ Zn chelates.....	52
3.3	N 1s NEXAFS Data for nMeq ₂ Zn chelates	52
3.4	C 1s NEXAFS Data for nMeqLi chelates.....	55
3.5	N 1s NEXAFS Data for nMeqLi chelates.....	55
3.6	O 1s NEXAFS Data for nMeqLi chelates.....	55
4.1	Absorption Data for nMeq ₂ Zn in different solvents	62
4.2	Absorption Data for nMeqLi in different solvents	62
4.3	Absorption λ _{max} and energy shifts from Mq _n	64
4.4	Photophysical Data of Mq _n in CH ₂ Cl ₂	65
4.5	Photophysical Data of Mq _n in DMF	66
4.6	Photophysical Data of nMeq _n M in CH ₂ Cl ₂	66
4.7	Photophysical Data of nMeq _n M in DMF	67
5.1	EL spectral data.....	75
5.2	EL device data.....	77

ACKNOWLEDGEMENTS

I would like to give my deepest thanks to Prof. Linda Sapochak, who have given me insurmountable support throughout my undergraduate, as well as graduate years. She has given me encouragement and taught me valuable skills and knowledge. Since she supported and trusted my independence laboratory, she has allowed me to think on my own, therefore, I have learned greatly from my own imagination, as well as mistakes. Thank you for allowing me to be in your group, it is an absolute pleasure working for and with you.

I wish to thank Prof. Lydia McKinstry, Prof. Dave Hatchett and Prof. Malcolm Nicol for being on my examination committee, and for providing invaluable advice and suggestions regarding my thesis.

A special mention must be made of Prof. Dennis Lindle and his post-doctorates, Dr. Oliver Hemmers and Dr. Ponnusamy Nachimuthu whose valuable guidance is deeply appreciated in carrying out NEXAFS experiments and in interpreting data.

I must thank Dr. Paul Burrows at Pacific Northwest National Laboratories for fabricating and testing my devices for the Znq_2 materials and also Prof. Stephen Forrest of Department the Electrical Engineering, Princeton University for fabricating and testing Alq_3 devices which was used in this thesis

I wish to thank the faculty and staff of Department of Chemistry, UNLV for making my six years stay here both pleasant and enjoyable. Special thanks to the Department

Chair, Prof. Kathleen Robins, Graduate Coordinator, Prof. Spencer Steinberg, and Office Manager, Ms. Juanita Lytel and Mark Miyamoto, for their support and assistance. Special thanks to the staff of the Graduate College: Carol Hoefle, Beverly Petrelis and Dr. Harriet Barlow for their kind hearted assistance throughout my graduate coursework.

I must thank my fellow graduate students Asanga Padmaperuma, Sanjini Nanayakkara and Asanga Ranasinghe along with undergraduates, Nancy Washton, Jeff Marshall, John Thornton, Daniel Fogarty, Greg Schmett, Shino Magaki, Joe Baker and James Cebe for all the assistance they gave me in my research and in writing this thesis.

Special thanks for the funding from NSF/CAREER – DMR, Research Corporation, ORAU, NSF/EPSCoR-Interface Science Program and DOE for the thermal analysis equipment in carrying out my research. I would also like to express my gratitude to Graduate College and the Department of Chemistry for financial support, which was most essential for my stay in USA.

I would like to thank my family. Since I left Philippines 8 years ago, even though I am almost 5,000 miles away from home, their spirits are always and forever within me. Edgardo Endrino and Florliza Endrino, my parents, who have provided their love, guidance and financial support. My sisters, Celeste, Florida, and Cassandra Mayer, although we have missed the company of one another, their love will always be cherished.

Finally, I would like to thank my soul mate, my best friend, my partner, and my love, Jasper Benincasa. Thank you for your unconditional love and for always believing in me, and supporting my dreams. You complete me.

CHAPTER 1

ORGANIC ELECTROLUMINESCENCE MATERIALS

1.1. Introduction

In the past decade there have been significant developments in the advancement of display technologies. Two of the most common types of displays that are found in almost every household are the cathode ray tube (CRT) and liquid crystal display (LCD). CRTs used for television sets and computer monitors are somewhat limited because they consume relatively large amounts of electricity. The single electron beam design is prone to misfocus. The CRTs high voltage electric circuits and strong electromagnetic fields can produce harmful electromagnetic radiation. Finally, CRTs are simply heavy and bulky.⁽¹⁾ These downfalls have led to a continuous evolution of display technology and ultimately to the development of the first flat panel display based on LCD technology in the 1970's.⁽¹⁾ Although LCD's are relatively lightweight and have low power consumption, they are beset by high prices, poor viewing angles, and low contrast and low luminance. A new technology that can be used in flat panel displays is based on organic electroluminescence (EL). Although organic electroluminescence from anthracene and other polymers was demonstrated much earlier, the rebirth of this technology marked by the demonstration of Tang and Van Slyke that efficient

electroluminescence can be achieved with an organic material, aluminum tris(8-quinolinolato) (Alq_3) (see Figure 1.1).⁽⁴⁾ By preparing organic materials as very thin films on a transparent anodic substrate (indium tin oxide coated glass) capped with a low work function metal cathode, these investigators showed that organic light-emitting devices (OLED's) can provide high brightness at drive voltages less than 10V (see Figure 1.2).

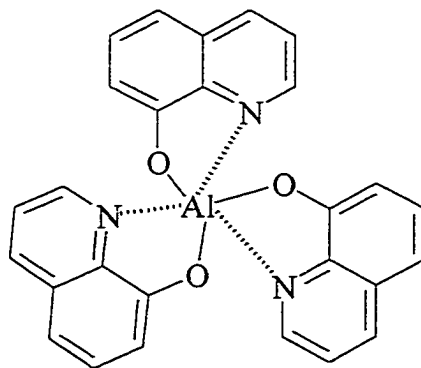


Figure 1.1. Aluminum tris-(8-quinolinolato) (Alq_3).

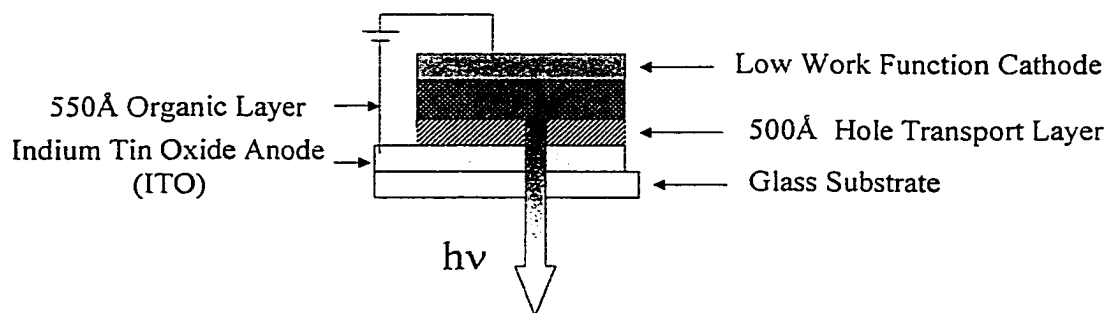


Figure 1.2. Organic Light-Emitting Device (OLED).

One of the advantageous properties of OLED's is that organic materials can be synthetically modified to provide light emission of all colors throughout the visible spectrum. Also, OLED's are relatively easy to fabricate, have low power consumption and high brightness, without high cost.⁽⁵⁾ Since the report by the Kodak researchers over a decade ago, advancements of research and developments of new materials and device architectures has led to products currently available in the marketplace based on organic EL.⁽¹⁾ However, the realization of a full-color flat-panel display requires a better understanding of the phenomenon of organic EL including optimization of the necessary properties of the constituent organic materials.

1.2 Background

OLED's can be fabricated in several ways. The most common configuration is still the one proposed by Tang and Van Slyke, which provided the first efficient electroluminescence from Alq₃ as shown in Figure 1.2. A hole-transporting layer (HTL) composed of a tertiary aromatic amine is deposited by thermal evaporation onto an indium-tin oxide (ITO) coated glass substrate, serving as the transparent anode. This is followed by thermal evaporation of the emissive layer, which also serves as the electron transport layer (ETL). The OLED is completed by capping with a low work function cathodic material, typically a Mg/Ag alloy. Electroluminescence (EL) occurs when electrons and holes are injected and transported through the device under an applied voltage and form excitons near the organic heterojunction, which decay to give light emission. The proposed mechanism of organic electroluminescence is depicted in Figure 1.3.

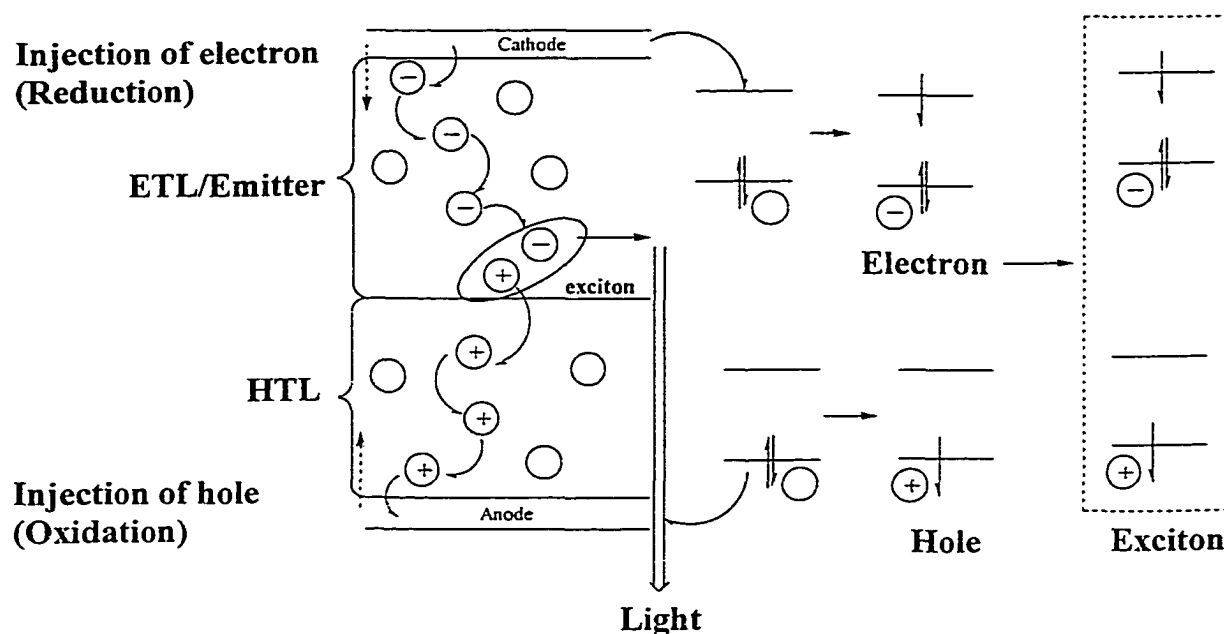


Figure 1.3. Proposed mechanism of organic electroluminescence.

For efficient EL the emissive material requires the optimization of several properties including: 1) high PL efficiency; 2) sublimation without chemical degradation; 3) appropriate energy-level alignment with the cathode and hole-transport layer (HTL) for efficient charge injection and transport; and 4) ability to form structurally stable films. All of these material properties depend on the molecular and electronic structure of the emitter molecule, as well as how it packs in the solid state. In fact all these material properties are so closely interrelated that often one property will be enhanced while another is sacrificed. Systematic studies of closely related materials are required to understand which properties are most important and to guide the design of optimized materials.

Many derivatives of Alq₃ have been investigated as emitter materials, including those in which with the metal ion has been substituted with other trivalent metals ($M^{+3} =$

Ga, In, and Sc)⁽⁶⁾ and with the 8-quinolinol ligands replaced with other substituents (F, Cl, NO₂⁽⁷⁾, CN⁽⁸⁾ and alkyl^(9,10) groups). Kido and Iisumi, recently showed that aluminum tris(4-methyl-8-quinolinolato) (4Meq₃Al) exhibited a larger EL efficiency⁽¹¹⁾ than Alq₃.⁽⁴⁾ Also, this material was later shown to exhibit both a higher photoluminescence (PL) quantum efficiency than Alq₃ both in solution and in the solid state.⁽¹²⁾ However, despite many experimental and theoretical studies of the archetypal Alq₃,⁽¹³⁾ systematic analyses of the effects of small chemical changes are sparse and we lack a roadmap for improving on the overall electroluminescence (EL) device performance of Alq₃.

We recently reported a systematic study on the effect of methylation at different positions of the 8-quinolinol ligand in metal tris(*n*-methyl-8-quinolinolato) chelates (nMeq₃M: *n* = 0, 3, 4, 5; M = Al⁺³ and Ga⁺³) on their photophysical, thermal and electroluminescence properties.⁽¹⁴⁾ In a series of homologous family of metal chelates where the metal ion is the same, we showed that methylation of the 8-quinolinol ligand decreased the crystalline melting point of the metal tris-chelates and increased the glass transition temperature of the amorphous materials, compared to the unsubstituted analogues; in both cases this was indicative of reduced intermolecular interactions. Although the 4Meq₃M chelates exhibited the highest PL and EL efficiencies, these characteristics were accompanied by higher EL device operating voltages in the corresponding OLED's.

The differences in EL performance of the nMeq₃M chelates was related to the changes in material properties caused by methylation of the ligand. The substantially larger PL efficiencies (ϕ_{PL}) for C-4 methylated derivatives contributed to their larger EL efficiencies (η_{EL}). However, for all methylated derivatives, if charge injection and

transport were similar and ϕ_{PL} was the dominating factor for high EL efficiencies, then the ratio of relative EL and PL efficiencies ($\eta_{\text{EL}}/\phi_{\text{PL}}$) should all be close to 1.0. Indeed, this ratio was < 1.0 for $4\text{Meq}_3\text{Al}$, but > 1.0 for $5\text{Meq}_3\text{Al}$. For the gallium series, all ratios were > 1.0 , with $4\text{Meq}_3\text{Ga}$ showing the smallest ratio. This data suggested that charge injection and/or transport efficiencies were not the same for these materials and was reduced by methylation of the pyridyl ring for both Alq_3 and GaQ_3 , as compared to the other methylated derivatives. This effect was less so for the $n\text{Meq}_3\text{Ga}$. Higher operating voltages required for OLED's utilizing $4\text{Meq}_3\text{Al}$ is also consistent with this data.

Since methylation of the pyridyl ring (C-4 position) causes only very small shifts in the absorption energy and thus does not significantly shift the energy of either the HOMO or LUMO compared to the unsubstituted analogues, it seemed likely that energy level matching of the Mq_n with the metal cathode and the HTL were similar to the unsubstituted analogues. As a result, it was less likely that charge-injection efficiency would be significantly affected by C-4 methylation. Therefore, the reason for the higher operating voltages was due to poorer electron transport through the metal/organic interface region.

The efficiency of charge-transport in organic molecular crystals is enhanced by strong intermolecular interactions of the polarizable π -system. There are two strong interactions in the solid state that must be accounted for: π - π stacking interactions and hydrogen bonding through the phenolic oxygen with the adjacent molecules. Although vapor-deposited films of Alq_3 and GaQ_3 are amorphous, crystallographic data for single crystals provided important information about their molecular packing preferences. For

example, Alq₃ and Gaq₃ showed strong dipolar π - π stacking interactions (3.5-3.9 Å) of the 8-quinolinol ligands between adjacent molecules with preferential overlap of the pyridyl rings.^(15,16,17) Since the pyridyl ring is the location of the LUMO, this explains the higher electron versus hole mobility in Alq₃ and related metal(8-quinolinolato) chelates. Therefore, it is expected that methylation of the 8-quinolinol ligand will decrease π - π stacking because of steric factors thereby reducing the cohesive forces between molecules.

On the other hand, hydrogen-bonding interactions between the phenolic oxygen with H-atoms at the C-5 and C-4 positions on adjacent molecules also have been identified for Gaq₃.⁽¹⁷⁾ Therefore, it is not unexpected that a decrease in π - π stacking due to steric factors, changes in polarity (via changes in the dipole moment of the ligand)⁽¹⁸⁾ and loss of hydrogen-bonding interactions of the metal chelates, will result upon methylation of the 8-quinolinol ligand. These changes will reduce the cohesive forces between molecules and analysis of the homologous series of methyl-substituted derivatives by thermal analysis revealed these differences.

In fact, 4Meq₃M chelates exhibited the lowest (~60°C vs. Alq₃) melting points of the series, clearly indicative of weaker intermolecular interactions. Glass transition temperatures were ~20°C higher than the unsubstituted analogues with no recrystallization of the amorphous state. This fact suggests that the entropic difference between the crystalline and amorphous states is small compared to Mq₃ materials. These differences in thermal properties result because C-4 methyl-substitution of the ligand acts to eliminate one of the H-bonding interactions, as well as to decrease the overlap between pyridyl rings of adjacent molecules. For 4Meq₃M chelates, a decrease in pyridyl ring

overlap therefore leads to inefficient electron transport properties since the pyridyl ring of the 8-quinolinol ligand is the site of the LUMO and, hence, the location of injected electrons.

The device operating voltage for 5Meq₃Al was also greater than that of Alq₃ but less so than for 4Meq₃Al chelates. The crystalline melting point of 5Meq₃Al was slightly lower than Alq₃, but it exhibited a high glass transition temperature with no recrystallization of the amorphous state, similar to 4Meq₃Al. C-5 methylation of the phenoxide ring will also result in decreased π - π stacking compared to Alq₃ with loss of the C-5 H-bonding interaction, but will not prevent preferential overlap of the pyridyl rings. Furthermore, unlike the 4Meq₃M chelates, in an OLED, hole-injection may be improved because the HOMO energy of Alq₃ is raised upon C-5 methylation. Therefore, 5Meq₃Al may also have closer energy level alignment with the HOMO of the HTL. We speculated, therefore, that both charge transport and hole injection efficiencies may be higher in 5Meq₃Al OLED's explaining why η_{EL}/ϕ_{PL} is much larger for 5Meq₃Al compared to 4Meq₃Al.

The effect of methylation of Gaq₃ on the thermal properties was similar to the aluminum series. However, the EL properties could not be explained in the same manner as Alq₃ and its methylated derivatives. Although the gallium series exhibited a decrease, approximately four times, in relative PL quantum efficiencies compared to the nMeq₃Al analogues, η_{EL}/ϕ_{PL} ratios were substantially larger for all nMeq₃Ga chelates. The gallium series were red-shifted in absorption energy, compared to the aluminum chelate analogues because of a higher HOMO energy resulting in improved energy level alignment and more efficient hole injection at the HTL/nMeq₃Ga interface. Since the

operating voltage depends on both charge injection and charge transport efficiencies, enhancement of the former may outweigh the effects of reduced charge transport caused by methylation of the ligand.

Our results suggested that by a judicious choice of both the type of substituent group and the position on the 8-quinolinol ligand it may be possible to improve overall EL efficiency of metal tris(8-quinolinolato) chelates and achieve a balance between high ϕ_{PL} , charge injection efficiency and charge transport ability. The conclusions drawn from the thermal analysis data are important for understanding how methylation affects the physical properties of the metal chelates. However, such an interpretation is only valid when comparing a homologous series of compounds, and similar comparisons of unrelated materials would not be as useful.

In this thesis work, these systematic studies have been extended to investigate the effect of ligand methylation in zinc bis(8-quinolinolato) (Znq_2) and lithium mono(8-quinolinolato) (Liq) chelate materials. Since the photophysical property of metal (8-quinolinolato) chelates is centered on the ligand (i.e., metal ion is not directly involved in the PL transition), we expected that the effect of methylation on PL energies and efficiencies should be similar. However, the oxidation state of Zn and Li are +2 and +1 respectively and the number of ligands in the resulting metal chelates are reduced, which significantly modifies how these materials pack in the solid state due to these changes in the coordination geometry. Therefore, we expected to observe significant differences in device performance with these materials compared to the metal tris(8-quinolinolato) chelates if indeed charge transport is the dominating property for enhancing EL efficiencies in OLED's.

1.3 Previous Studies of Znq₂ and Liq Materials

Although there are several reports on the photophysical,^(19,20,21,22,23) as well as electroluminescence properties^(22,23,24) of Znq₂ and its 2Meq₂Zn derivative, the results are inconsistent. One reason for the discrepancies in the photophysical data is that the structure of the metal chelate was in question. No purification of the resulting metal chelate had been performed, and elemental analysis suggested contamination from both unreacted ligand and partially chelated metal salt. More recent studies of Znq₂ have also lead to inconsistent reports of its absorption and photoluminescence energies in both solution and in the solid state.⁽²³⁾ One of the major obstacles in working with Znq₂ materials is their insolubilities and failed attempts to confirm the structure by single-x-ray crystallography, as has been done for the metal tris(8-quinolinolato) chelates of aluminum and gallium.⁽¹⁵⁾ Only the crystal structure for the dihydrate form of Znq₂ has been reported showing that the 8-quinolinolato rings were mostly planar because of repulsion by the water molecules coordinated to the zinc ion.⁽²⁵⁾ On the other hand, Kai reported structures for crystals grown by slow vacuum sublimation of Znq₂, as a tetrameric structure⁽²⁶⁾ rather than the bis-quinolate chelate. To date, it has not been confirmed whether this was an anomaly due to the method of crystal growth, or indeed the true form of Znq₂ anhydrous. Even molecular modelling of Mq₂ complexes using ZINDO and ESSF methods provided conflicting results as one supporting a distorted tetrahedral while the latter supports a planar structure for Znq₂.⁽²⁷⁾ ZINDO is a semi-empirical approach, while ESSF (Extensive Systematic Force Field) is a molecular mechanics approach.

The photoluminescence efficiency of Znq_2 is known to be inferior to that of Alq_3 because of the more ionic nature of the bonding of the metal ion with the ligand.⁽¹³⁾ However, some researchers have reported that Znq_2 exhibits higher luminance output compared to Alq_3 therefore surmising that Znq_2 may be a better electron transporting material.⁽²⁴⁾ However, no systematic studies of identical OLED devices or charge mobility studies have been reported.

Investigations of the electroluminescence device properties of Znq_2 have been previously reported by Hamada,⁽²²⁾ who reported that the luminance output of Znq_2 was higher and voltage requirement lower than for Alq_3 when both were used as emitter materials in OLEDs. It was inferred that the electron mobility in Znq_2 might be higher than in Alq_3 . However, it was not clear whether a direct comparison of identically prepared OLED's of Znq_2 and Alq_3 was conducted. Because the device properties are very sensitive to: the thickness of the layers; cleaning protocol of the ITO glass coated substrate; and exposure time to air; therefore, it is important to fabricate all devices such that the common layers of the device (HTL and cathode layers) are deposited simultaneously, as done here. For a systematic study, this eliminates any variation in device performance due to fabrication.

Although fewer studies on the Liq chelate materials are available, Kido has suggested that this material could be used to enhance electron injection into Alq_3 – based OLED's when deposited as a thin layer between the top cathode and the Alq_3 emitter layer.⁽²⁸⁾ More recently, Schmitz reported results for Liq and 2MeqLi materials as both electron injection materials for Alq_3 -based OLEDs and as blue emitter materials in OLED's.⁽²⁹⁾ However, material purity was again in question due to their inability to

obtain adequate elemental analysis. Thus, it is difficult to draw conclusions with regard to structure/function relationships.

The synthesis and characterization of anhydrous methylated zinc bis(*n*-methyl-8-quinolinolato) ($n\text{Meq}_2\text{Zn}$) and methylated lithium mono (*n*-methyl-8-quinolinolato) ($n\text{MeqLi}$), where $n = 2, 4, 5$ and their unsubstituted analogues, Znq_2 and Liq are presented in Chapter 2. After careful purification by high-vacuum temperature-gradient sublimation all materials were obtained with adequate elemental analyses. In the remaining chapters, analyses of differences in electronic structures via x-ray absorption spectroscopy (Chapter 3); photophysical properties (Chapter 4); and electroluminescence device performance (Chapter 5) are presented. In each chapter, the results for the zinc bis(8-quinolinolato) and lithium mono(8-quinolinolato) chelates will be compared and contrasted with the results obtained previously for the metal tris(8-quinolinolato) derivatives. We show that the metal ion, although not directly involved in the electronic transition responsible for PL and EL, has significant effects on EL performance of these materials via changes in coordination geometry of the resulting metal chelate. These effects also occur via electronic structure differences imparted by the character of the metal-ligand bond.

References

1. Kelly, S.M. Flat Panel Displays. Advanced Organic Materials (Royal Society of Chemistry: Cambridge) 2000.
2. Pope, M.; Kallamann, H.P. and Magnante, P.J. Electroluminescence in organic crystals. *J. Chem. Phys.*, **1963**, 38, 2042.
3. a) Kaneto, K.; Yoshino, K.; Koa, K. and Inuishi, Y. *Jpn. J. Appl. Phys.* **1974**, 18, 1023. b) Partridge, R.H. *Polymer*. **1983**, 24, 755.

4. Tang, C.W. and VanSlyke S.A. Organic electroluminescent diodes. *Appl. Phys. Lett.* **1987**, 51, 913.
5. Sheats, J.R.; Antoniadis, H.; Hueschen, M.; Leonard, W.; Miller, J.; Moon, R.; Roitman, D. and Stocking, A. Organic electroluminescent devices. *Science*. **1996**, 273, 884-888.
6. Burrows, P.E.; Sapochak, L.S.; McCarty, D.M.; Forrest, S.R and Thompson, M.E. Metal ion dependent luminescence effects in metal tris-quinolate organic heterojunction light emitting devices. *Appl. Phys. Lett.* **1994**, 64(20), 2718-2720.
7. Matsumura, M. and Akal, T. *Jpn. J. Appl. Phys.* **1996**, 35, 5357.
8. Burrows, P.E.; Shen, Z.; Bulovic, V.; McCarty, D.M.; Forrest, S.R.; Cronin, J.A. and Thompson, M.E. Relationship between electroluminescence and current transport in organic heterojunction light-emitting devices. *J. Appl. Phys.* **1996**, 79(10), 7991-8006.
9. Hamada, Y.; Sano, M.; Fujita, T.; Nishio, Y.; and Shibata, K. *Jap. J. Appl. Phys.* **1993**, 32(4A), L514.
10. Kido, J. and Iizumi, Y. Efficient electroluminescence from tris(4-methyl-8-quinolato)aluminum(III). *Chem. Lett.* **1997**, 963-964.
11. Kido, J. and Iizumi, Y. Fabrication of highly efficient electroluminescent devices. *J. Appl. Phys.* **1998**, 73(19), 2721-2723.
12. Murata, H.; Merritt, C.D.; Mattoussi, H.; and Kafafi, Z.H. Dye-doped molecular light emitting diodes with enhanced performance. *SPIE-Int. Soc. Opt. Eng.-Organic Light-Emitting Materials and Devices II*, **1998**, 3476, 88.
13. Chen, C.H. and Shi, J. Metal chelates as emitting materials for organic electroluminescence. *Coord. Chem. Rev.* **1998**, 171, 161-174.
14. Sapochak, L.S.; Padmaperuma, A.B.; Washton, N.M.; Endrino, F.L.; Schmett, G.T.; Marshall, J.B.; Fogarty, D.P.; Burrows, P.E.; and Forrest, S.R. Effects of Systematic Methyl-Substitution of Metal (III) Tris(n-Methyl-8-Quinololato) Chelates on Material Properties for Optimum Electroluminescence Device Performance, *J. Am. Chem. Soc.* **2001** in press.

15. Schmidbaur, H.; Lattenbauer, J.; Dallas, L.; Muller, W.G. and Kumberger, O. Model systems for Gallium extraction I, Structure and molecular dynamics of aluminum and gallium tris(oxinates). *Z. Naturforsch.* **1991**, 46b, 901-911.
16. Brinkmann, M.; Gadret, G.; Muccini, M.; Taliani, C.; Masciocchi, N.; and Sironi, A. *J. Am. Chem. Soc.* **2000**, 122, 5147.
17. Wang, Y., Zhang, W., Li, Y., Ye, L. and Yang, G. X-ray Crystal Structure of allium Tris- (8-hydroxyquinoline): Intermolecular - Stacking Interactions in the Solid State, *Chemistry of Materials*; **1999**; 11, 3, 530-532.
18. Bader, M. *J. Am. Chem. Soc.* **1992**, 114, 6575.
19. Lytle, F.E.; Story, D.R. and Juricich, M.E. Systematic atomic number effects in complexes exhibiting ligand luminescence. *Spectrochimica Acta.* **1973**, 29A, 1357-1369.
20. Bhatnagar, D. and Forster, L. The Luminescence of Oxinates and Metal Oxinates. *Spectrochimica Acta.* **1965**. 21, 1803-1807.
21. Hamada, Y.; Sano, T.; Fujita, N.; Fujii, T.; Nishio, Y.; and Shibata, K. Organic Electroluminescent Devices with 8-Hydroxyquinoline derivative-metal complexes as an emitter. *Jpn. J. Appl. Phys.* **1993**, 32, L514-L515.
22. Hopkins, T.A.; Meerholz K.; Shasheen, S.; Anderson, M.L.; Schmidt A.; Kippelen, B.; Padias, A.B.; Hall, K.H.; Peyghambrian, N.; Armstrong, N.R. Substituted aluminum and zinc quinolates with blue-shifted absorbance and luminance bands: synthesis and spectroscopic, photoluminescence, and electroluminescence characterization. *Chem. Mater*, **1996**, 8(2), 344-351.
23. Donze, N.; Pechy, P.; Gratzel, M.; Schaer, M.; and Zuppiroli, L. Quinolate Zinc Complexes as Electron Transporting Layers in Organic Light-Emitting Diodes. *Chem. Phys. Lett.* **1999**, 315, 405-410.
24. Merritt, L.L.; Cady, R.T. and Mundy B.W. The Crystal Structure of Zinc 8-hydroxyquinolate dihydrate. *Acta Cryst.* **1954**, 7, 473.
25. Kai, Y.; Moraita, M; Yasuka, N.; and Kasai, N. The Crystal and Molecular Structure of Anhydrous Zinc 8-Quinolate Complex. *Bull. Chem. Soc. Jpn.*, **1985**, 58, 1631-1635.

26. Nicolau, D.V. and Yoshikawa, S. Molecular Modelling of Me^{2+} (8-hydroxy-quinolate)₂ Complexes using ZINDO and ESSF methods. *J. Mol. Graph. and Mod.* **1998**, 16, 83.
27. Kido, J. Organic EL devices based on novel metal complexes. *SPIE Proceedings*, San Diego, CA. July **1997**.
28. Schmitz, C.; Schmidt, H. and Thelakkat, M. Lithium-quinolate complexes as emitter and interfaces materials in organic light-emitting diodes. *Chem. Mater.* **2000**, 12, 3012-3019.

CHAPTER 2

MATERIALS SYNTHESIS AND CHARACTERIZATION

2.1 Syntheses of Metal 8-Quinolinolato Chelates

Starting materials, 8-quinolinol, 8-hydroxyquinaldine, and reference materials, aluminum tris(8-quinolinolato) (Alq_3) and zinc bis(8-quinolinolato) (Znq_2) were obtained from Aldrich Chemical Co. The 4- and 5-methyl- 8-quinolinol ligands were prepared according to the published procedures reported previously by our research group.⁽¹⁾ We synthesized zinc bis(8-quinolinolato) (Znq_2) and lithium mono(8-quinolinolato) chelates, as well as its 4C- and 5C- methylated derivatives. Zinc bis(2-methyl-8-quinolinolato) ($2\text{Meq}_2\text{Zn}$) was also synthesized.

2.1.a Syntheses of Zinc Bis(8-Quinolinolato) Chelates

There are several published procedures for synthesizing Znq_2 .⁽²⁻⁸⁾ Utilization of diethyl zinc(II) in dry ether, as described by Hopkins⁽²⁾ was found to be impractical because of the moisture sensitive nature of diethyl zinc. Although this synthetic approach is reported to lead directly to anhydrous Znq_2 , it provided low yields of product.

On the other hand, hydrated zinc salts, such as $\text{Zn}(\text{OAc})_2$, ZnCl_2 and $\text{Zn}(\text{NO}_3)_2$, were more practical starting materials.⁽³⁻⁷⁾ All zinc chelates in this thesis were prepared by modifications of the synthetic procedure described by Nakamura,⁽³⁾ utilizing $\text{Zn}(\text{OAc})_2$ dihydrate, as depicted in Figure 2.1. In general, the zinc salt and ligand were

dissolved separately in methanol in a 1:2 molar ratio. The zinc salt solution was then added dropwise to the warm ligand solution with constant stirring to form a yellow amorphous precipitate. The resulting heterogeneous solution was then refluxed for 3 hours to complete the reaction. The metal chelate was isolated by filtration of the cooled reaction mixture and the resulting solid was washed first with a warm 50% aqueous solution of NaHCO_3 followed by warm methanol and then hexane. The crude dihydrate forms of the zinc bis(8-quinolinolato) chelates were isolated as solids in high yields (~80%), with the exception of $4\text{Meq}_2\text{Zn}$. The low yield in this case was most likely due to loss of product during washings, because of the higher solubility of the 4-methyl derivative, as reported previously for $4\text{Meq}_3\text{Al}$.⁽⁹⁾ The anhydrous metal chelates, identified by infrared spectroscopy and thermal analysis, were then obtained by heating the crude material at 110°C under vacuum for 24 hrs.

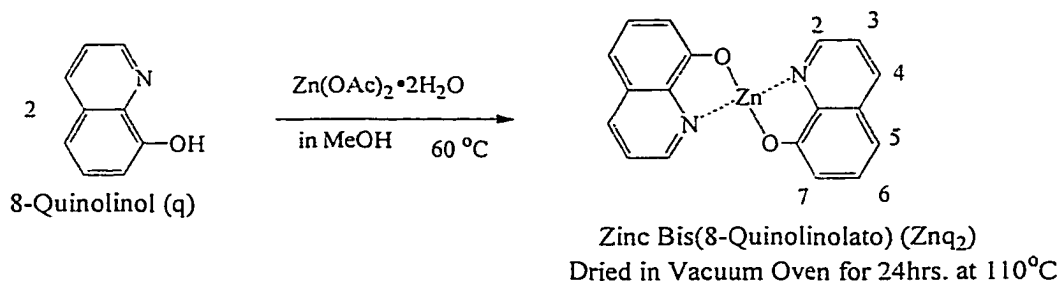


Figure 2.1. General synthetic scheme for zinc bis (8-quinolinolato) chelates.

The zinc bis(8-quinolinolato) chelates synthesized and characterized in this thesis are depicted in Figure 2.2. Elemental analyses were within standard publication limits which is $\pm 0.4\%$, for all materials with the exception of $2\text{Meq}_2\text{Zn}$. For this material, steric hindrance is imposed by the methyl group substituted at the 2-position of the 8-

quinolinol ring and significantly decreases the stability of the chelate as evidenced by the substantially lower thermal decomposition temperature compared to the other methylated zinc chelates. Therefore, this material may be less amenable to elemental analysis. Regardless, photophysical characterization was still performed and will be discussed. The exact structure of $2\text{Meq}_2\text{Zn}$ is still in question.

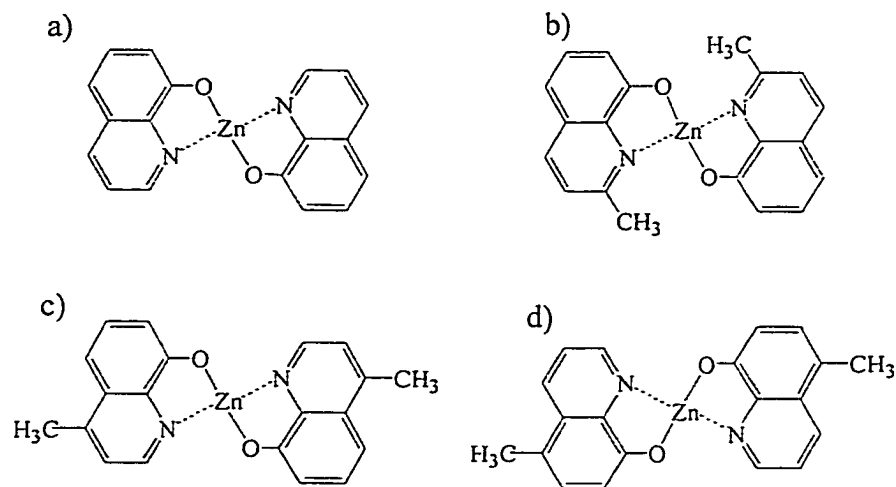


Figure 2.2. Synthesized zinc bis(8-quinolinolato) chelates: a) zinc bis(8-quinolinolato) (Znq_2); b) zinc bis(2-methyl-8-quinolinolato) ($2\text{Meq}_2\text{Zn}$); c) zinc bis(4-methyl-8-quinolinolato) ($4\text{Meq}_2\text{Zn}$); d) zinc bis(5-methyl-8-quinolinolato) ($5\text{Meq}_2\text{Zn}$).

2.1.b Syntheses of Lithium Mono (8-Quinolinolato) Chelates

There are few published procedures for synthesizing lithium mono(8-quinolinolato) chelates.⁽¹⁰⁻¹²⁾ Initial attempts to prepare Liq using the hydrated salts of LiCl or LiNO_3 were unsuccessful. A new synthetic procedure for preparing Liq and its methyl substituted derivatives from LiOH hydrate is described here. As illustrated in Figure 2.3, a 10% by wt. solution of LiOH hydrate in deionized water was added dropwise to a solution of the appropriate ligand dissolved in minimum amount of

absolute ethanol. The ligand solution was warmed and then was allowed to cool to room temperature before the lithium hydroxide solution was added. When a 1:1 molar ratio of the ligand to Li salt was used, the pH of the resulting solution was ~ 8 , and a precipitate formed almost immediately, except in the case of the, 4MeqLi which took ~ 30 min. The crude product was then filtered and washed with a minimum amount of warm deionized water and 90 % ethanol, air-dried, then recrystallized from absolute ethanol. The recrystallized Liq was subjected to vacuum sublimation at 150°C ($\sim 10^{-2}$ Torr) to remove the unreacted ligand, and the crude sublimate was further purified by high-vacuum temperature-gradient sublimation ($\sim 10^{-7}$ Torr) over a three-day period.

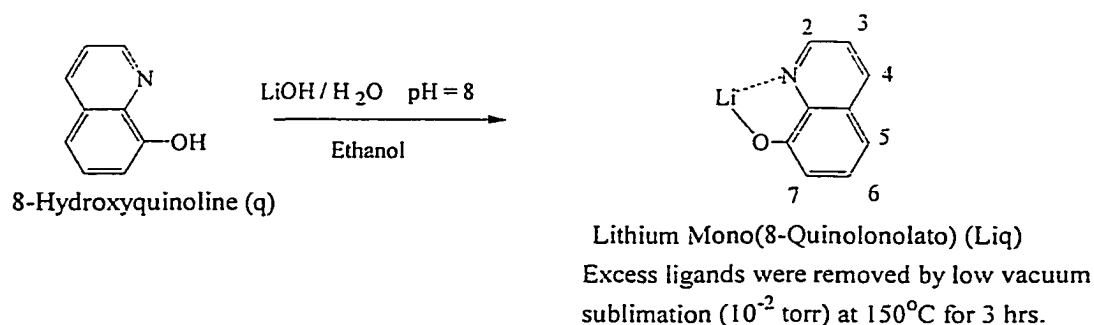


Figure 2.3. General synthetic scheme for lithium mono(8-quinolinolato) chelates.

For this thesis, all methyl- substituted lithium chelates, as depicted in Figure 2.4, were prepared and purified in a similar manner and gave adequate elemental analyses. In contrast to our results, Schmitz reported that adequate elemental analysis could not be achieved for Liq and 2MeqLi because of the hygroscopic nature of the materials.⁽¹²⁾ Schmitz prepared Liq from anhydrous LiOH in dry CH_2Cl_2 , which resulted in a white crystalline solid that was dried under vacuum but was not further purified. Their TGA

analysis gave two weight-loss steps identical to our results for the recrystallized Liq. However, they attributed the first weight loss to dehydration rather than sublimation of unreacted ligand, which is likely the reason for their elemental analysis discrepancies.

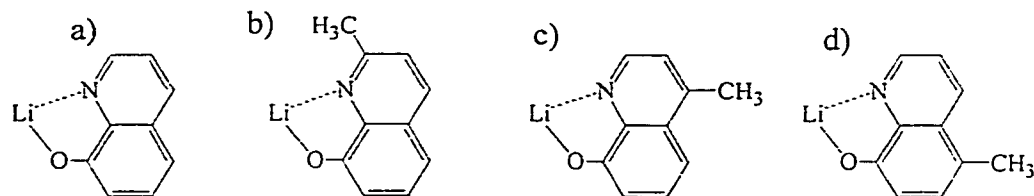


Figure 2.4. Synthesized lithium (8-quinolinolato) chelates: a) lithium(8-quinolinolato) (Liq); b) lithium (2-methyl-8-quinolinolato) (2MeqLi); c) lithium (4-methyl-8-quinolinolato) (4MeqLi); d) lithium (5-methyl-8-quinolinolato) (5MeqLi).

2.2 Material Characterization

The structures and physical properties were characterized by ^1H NMR (when possible), infrared spectroscopy, thermal analysis and elemental analysis obtained from NuMega Resonance Laboratories. The exact masses of the C, N, and H that was used to calculate the theoretical %C, %N and %H for elemental analysis was derived from the average mass from the % abundance of all the isotopes. The results are found to be adequate and they are within $\pm 0.4\%$, except for $2\text{Meq}_2\text{Zn}$. The oxidation and reduction potentials of Alq_3 and Znq_2 were also determined by cyclic voltammetry.

2.2.a NMR Spectroscopic Characterization

There are limited reports of the ^1H -NMR characterization of zinc and lithium (8-quinolinolato) chelates.^(2,12,13) The ^1H -NMR spectrum of Znq_2 synthesized in this thesis work was obtained using a Bruker AMX 400 MHz NMR by heating Znq_2 in DMSO-d_6

directly in the NMR tube to dissolve the material. The resulting NMR spectrum exhibited broad peaks, but the chemical shift values were consistent with those previously reported by Baker (Table 2.1).⁽¹³⁾ Peak broadening at elevated temperatures has been observed previously by Schmidbauer for aluminum and gallium tris(8-quinolinolato) chelates.⁽¹⁴⁾ This broadening was attributed to a ligand-equilibrating process, where the more labile metal-nitrogen bond was believed to break and reform. However, more recently, Hopkins⁽²⁾ reported that Znq_2 exhibited two sets of aromatic protons in $CDCl_3$ but only one set of broad peaks in $DMSO-d_6$. This was explained by suggesting that Znq_2 may exist as a tetramer in the solid-state, as reported previously.⁽¹⁵⁾ According to single crystal x-ray analysis of crystals formed by high-vacuum sublimation of Znq_2 , four Zn ions were shown to be coordinated with a total of eight ligands via bridging by the phenoxide oxygens of the ligand. Two of the Zn ions were hexacoordinate, and the other two were pentacoordinate, which could give rise to two different sets of aromatic protons in the 1H NMR spectrum. Therefore, Hopkins surmised that the tetramer may be stable in the less polar $CDCl_3$ and partially dissociated to the bis-quinolinolato form in $DMSO-d_6$. As described in chapter 4 of this thesis, Znq_2 materials have strong interactions with the solvents. We believe this result is more consistent with an equilibrium between a tetrahedral and octahedral in solution. (See Figure 2.5)

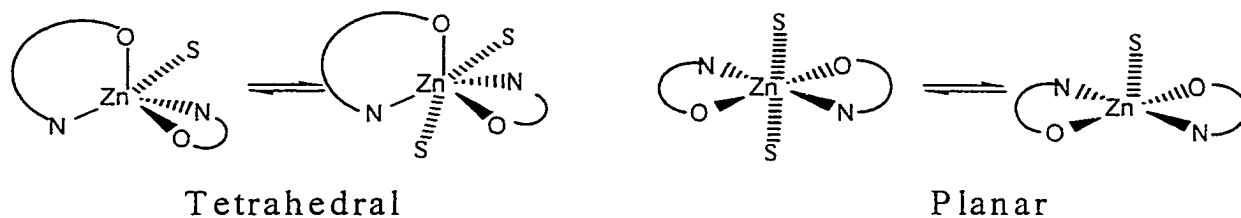


Figure 2.5. Two sets of peaks for quinolate ligands may arise in different solvents due to solvent (S) coordination thus allowing equilibrium between a hexacoordinate (planar) and pentacoordinate (tetrahedral) metal.

Table 2.1 ^1H NMR Chemical Shifts in ppm for Znq_2 .

	Znq_2	
	Baker ⁽¹³⁾ DMSO- d_6 ± 0.01 ppm	Endrino DMSO- d_6
δH_2	8.44	8.47
δH_3	7.33	7.34
δH_4	8.22	8.27
δH_5	6.91	7.04
δH_6	7.21	7.25
δH_7	6.82	6.87
δHMe	----	----

Unfortunately, attempts to obtain ^1H NMR spectra of the methylated derivatives of Znq_2 chelates in CDCl_3 and $\text{DMSO-}d_6$ were unsuccessful, because of the insolubility of the materials and the inability to conduct variable temperature NMR analysis. Even the most soluble material, $4\text{Meq}_2\text{Zn}$ would precipitate out of solution during the experiment giving poor results.

Table 2.2 ^1H NMR Chemical Shifts in ppm for $n\text{Meq}$ and $n\text{MeqLi}$ in $\text{DMSO-}d_6$.

	Na^+/q^- Baker ⁽¹³⁾	q	Liq	4Meq	4MeqLi	5Meq	5MeqLi
δH_2	8.39	8.91	8.45	8.31	8.71	8.87	8.44
δH_3	7.16	7.59	7.30	7.15	7.41	7.60	7.34
δH_4	7.92	8.36	8.07	----	----	8.40	8.14
δH_5	6.48	7.45	6.62	6.68	7.49	----	----
δH_6	7.09	7.50	7.20	7.20	7.48	7.28	7.01
δH_7	6.47	7.19	6.54	6.54	7.10	6.99	6.35
δHMe	----	----	----	2.53	2.66	2.54	2.38

Not all lithium mono(8-quinolinolato) chelates were sufficiently soluble in CDCl_3 to obtain ^1H NMR spectra, but all were soluble in DMSO-d_6 . However, as indicated by UV-Vis absorption spectroscopy experiments (see Chapter 4), the Liq chelates seem to dissociated to the Li^+ cation and quinolate $^-$ anion in the polar DMSO solvent, therefore the ^1H NMR of these materials is more representative of the solvated ion-pair rather than the actual chelate. The ^1H NMR spectra of all n-methyl-8-quinolinol ($n = 0, 2, 4, \text{ and } 5$) ligands and lithium chelates were obtained in DMSO-d_6 , and the chemical shift values, referenced from TMS = 0.00 ppm, and coupling constants are reported in Table 2.2

Table 2.3 ^1H NMR Chemical Shifts in ppm for Liq and 8-quinolinol (q) in CDCl_3 .

	q	Liq
δH_2	8.78	8.45
δH_3	7.38	7.30
δH_4	8.10	8.07
δH_5	7.30	6.62
δH_6	7.44	7.20
δH_7	7.21	6.54
δHMe	----	----

The proton resonances of Liq and 5MeqLi were shielded compared to the corresponding neutral ligands, 8-quinolinol (q) and 5Meq. The largest shielding effects (0.4-0.8 ppm upfield shifts) occurred for protons H2, H5, and H7 for Liq and H2 and H7 for 5MeqLi. These chemical shift values are consistent with those reported by Baker for 8-quinolinol and the 8-quinolinol anion prepared by addition of aqueous NaOH in DMSO (Table 2.2).⁽¹³⁾ The anionic form of the ligand can donate electron density into the aromatic ring system via the lone pair electrons on oxygen, thus shielding the aromatic

protons. In contrast, all protons, including the methyl group are deshielded in the 4MeqLi NMR spectrum compared to the neutral ligand where the largest deshielding effects were observed for H2, H5 and H7.

Table 2.4 Chemical Shift Change in ppm between 8-quinolinol and Liq in DMSO-d₆ and CDCl₃.

Sample	δ H2 (ppm)	δ H3 (ppm)	δ H4 (ppm)	δ H5 (ppm)	δ H6 (ppm)	δ H7 (ppm)
DMSO-d ₆	0.46	0.29	0.29	0.83	0.30	0.65
CDCl ₃	0.32	0.08	0.12	0.78	0.24	0.67

Table 2.4 lists the difference of the chemical shift of 8-quinolinol (q) and Liq in DMSO-d₆, more polar, and CDCl₃, less polar (See Table 2.3), solvents. The larger difference observed for DMSO-d₆ indicates that the aromatic protons are more shielded in the more polar solvent, indicative of stronger solvent interaction. As presented in chapter 3 and 4, there is more ionic character in the metal quinolate ligand bond in Liq than in Znq₂ and Alq₃. The more shielded aromatic protons suggest that there is delocalization of the lone pair on the phenoxide oxygen into the quinolate ligand.

2.2.b Infrared Spectroscopic Characterization

The infrared spectra of the following metal (8-quinolinolato) chelates have been previously reported: Znq₂,^(2,15,16,17,18) 2Meq₂Zn,^(15,16) 4Meq₂Zn,⁽¹⁶⁾ Liq⁽¹²⁾ and 2MeqLi.⁽¹²⁾ In this thesis work, FT-IR spectra for zinc- and lithium- (8-quinolinolato) chelates were recorded as KBr pellets and as vapor-deposited films on NaCl plates on a Nicolet 210 FT-IR spectrometer. Consistent with the literature, metal (8-quinolinolato) chelates exhibit similar IR spectra with only small shifts in the peaks because of the metal ion and

change in coordination geometry. A comparison of the IR spectra of Znq_2 and Liq as a KBr pellets and as a vapor deposited films are shown in Figure 2.6 and 2.7. For all metal chelates reported here, no new peaks were observed in the film samples suggesting that no deleterious structural changes occur upon vapor deposition. IR spectra of the other metal chelates are presented in Appendix I and peak assignments are tabulated in Tables 2.5 and 2.6.

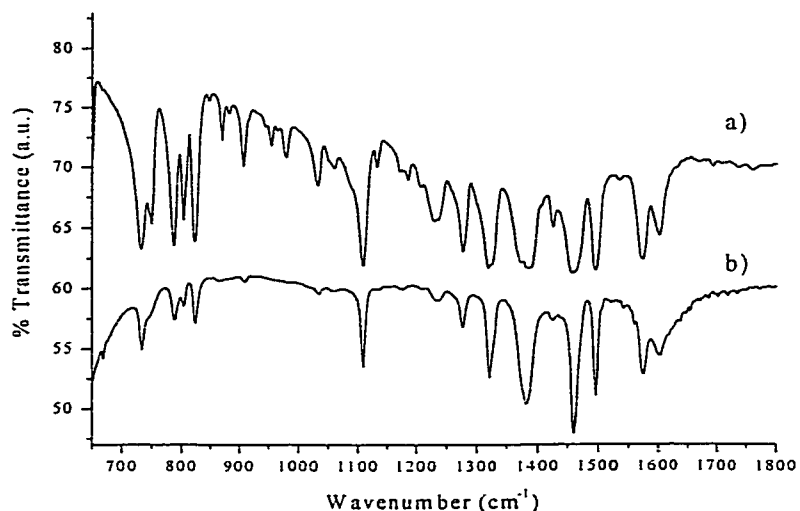


Figure 2.6. FT-IR spectra of Znq_2 : a) KBr pellet; b) vapor deposited film.

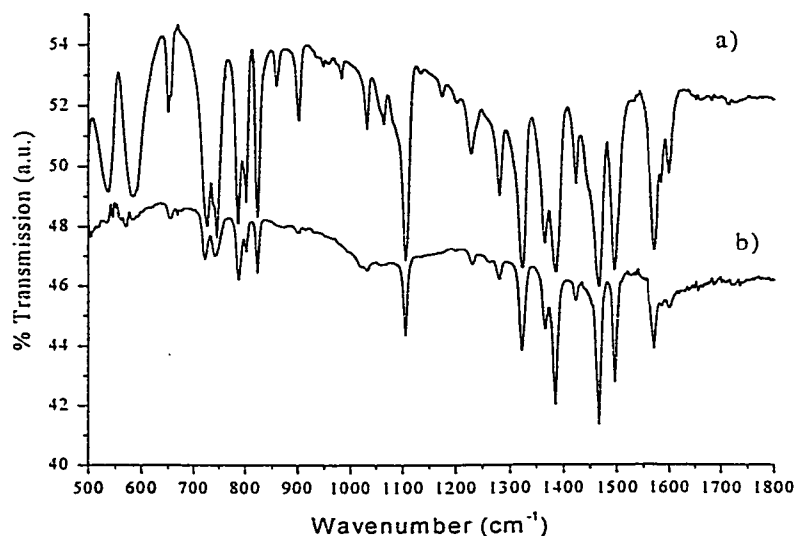


Figure 2.7. FT-IR spectra of Liq: a) KBr pellet; b) vapor deposited film.

Table 2.5 Assignments of FT-IR Peaks in cm^{-1} for Zinc bis(8-quinolinolato) Chelates.

Assignment	Znq ₂	2Meq ₂ Zn	4Meq ₂ Zn	5Meq ₂ Zn
C-O str + C-H bend	1110	1112	1101	1093
C-N str + C-H bend	1242	1238	1250	1242
Ring str + C-O str + C-H bend	1328	1329	1316	1319
Ring Stretching	1605	1608	1605	1602
Ring Stretching	1577	1571	1578	1577
Ring Stretching	1468	1465	1468	1466
Ring Stretching	1500	1506	1510	1506
	743	741	733	755
CH-wag	790	790	802	853
	821	829	840	786
M-O str + ring deformation	643	617	669	645

Table 2.6 Assignments of FT-IR Peaks in cm^{-1} for Lithium Mono(8-quinolinolato) Chelates.

Assignment	Liq	2MeqLi	4MeqLi	5MeqLi
C-O str + C-H bend	1105	1101	1105	1089
C-N str + C-H bend	1240	1243	1245	1240
Ring str + C-O str + C-H bend	1321	1333	1326	1322
Ring Stretching	1608	1589	1590	1571
Ring Stretching	1573	1563	1572	
Ring Stretching	1465	1460	1464	1467
Ring Stretching	1498	1504	1509	1504
	750	750	741	757
CH-wag	792	799	802	832
	823	830	817	784
M-O str + ring deformation	648	653	668	671

2.2.c Thermal Analysis Characterization

As discussed in Chapter 1, the morphological stability of an organic material in an OLED is a crucial property for device reliability and long operating lifetimes. Ideally, formation of stable glassy films with high glass transition temperatures (T_g) well above

room temperature, where recrystallization at higher temperatures does not occur is desired. The morphological stability of Alq_3 has been attributed to its intrinsic polymorphic (multiple packing behavior), racemic nature and strong dipolar interactions,⁽¹⁹⁾ giving rise to a large T_g (175°C).⁽²⁰⁾ We recently reported the thermal analysis characterization of Alq_3 , Gaq_3 and methyl-substituted derivatives.⁽⁹⁾ Only thermal decomposition properties of Zn bis(8-quinolinolato) dihydrate have been reported previously.⁽²¹⁾ Here we report the first detailed thermal analysis characterization of anhydrous zinc and lithium (8-quinolinolato) chelates.

Differential scanning calorimetry (DSC) and thermal gravimetric analysis (TGA) were performed simultaneously using a Netzsch Simultaneous Thermal Analyzer (STA) system. Pure polycrystalline samples (5-8 mg) were placed in aluminum pans and heated at a rate of $20^\circ\text{C}/\text{min}$ under a flow of N_2 gas at a rate of 50 mL /min. The temperatures of all phase transitions were measured including the melting temperature (T_m). Indium metal was used as the temperature standard. After the first heating, melted samples were cooled at a rate of $20^\circ\text{C}/\text{min}$ to form glasses. The glass transition (T_g) and the crystallization point (T_{cl}) were measured from a second heating of the glassy state. The T_{cl} is exothermic transitions and T_m is endothermic transitions. The maximum weight loss temperature (decomposition temperature) was determined for each sample and reported as the maximum peak of the DTG (derivative of the TGA curve), as well as the onset of the TGA curve.

The thermal properties of Znq_2 and Liq and their methyl-substituted derivatives are presented in Table 2.7. A comparison of the results with the metal tris-chelates including the effect of coordination geometry on metal chelate stability, melting behavior

and glass transition is discussed below. The thermal gravimetric analysis (decomposition temperatures) of all materials studied are in Appendix II.

Table 2.7 Thermal Analysis Results.

Metal Chelate	T_m (°C)	ΔH_{fusion} (kJ/mol)	T_g (°C)	T_{cl} Onset (°C)	<i>Max.</i> <i>Wt.</i> <i>Loss</i> <i>Temp.</i> (°C)(onset)	<i>Max.</i> <i>DTGA</i>
Znq ₂	366	26.14	177	272	402	435
2Meq ₂ Zn	362	40.73	149	240	357	390
4Meq ₂ Zn	333	24.09	191	n.o.	416	449
5Meq ₂ Zn	371	24.05	202	324	411	445
Liq	366	14.32	n.o.	n.o.	477	518
4MeqLi	397	19.53	n.o.	n.o.	484	524
5MeqLi	423	21.36	n.o.	n.o.	505	527

n.o. = not observable

Znq₂ exhibits several endothermic and exothermic transitions prior to a strong endothermic melting transition (T_m) at 364°C (see Figure 2.7). Similar transitions prior to T_m were observed for metal tris-quinolate chelates (Alq₃ and Gaq₃) and were attributed to polymorphic behavior.⁽⁹⁾ It is not unlikely that Znq₂ may exhibit polymorphic behavior because at least three polymorphic forms have been observed for copper bis(8-quinolinolato).⁽²²⁾ Liq, on the other hand, exhibits a single melting transition at 397°C.

For all Alq₃ and Gaq₃ chelates, T_m transitions were accompanied by 2-13% weight losses. This weight loss is due to sublimation of the sample prior to decomposition at temperatures approaching 500°C. Znq₂ also exhibits a weight loss immediately following T_m , but it is much smaller (~2%) compared to the metal tris-chelates. Liq shows no detectable weight loss. Similar trends are observed when comparing the methyl-substituted derivatives of the metal tris- and bis-(8-quinolinolato)

chelates suggesting that, in general the Znq_2 and Liq chelates are more difficult to sublime than the metal tris-chelates.

Upon methyl-substitution the T_m of the zinc bis(8-quinolinolato) chelates increases in the order $4Meq_2Zn \ll 2Meq_2Zn < Znq_2 < 5Meq_2Zn$. All the zinc chelates exhibit lower melting temperatures than the metal tris-chelates, but the effects of methyl-substitution on T_m are similar. For example, both $4Meq_3Al$ and $4Meq_3Ga$ melt at $\sim 60^\circ C$ lower temperature than the unsubstituted analogues, similarly $4Meq_2Zn$ melts at a $\sim 40^\circ C$ lower temperature compared to Znq_2 . In addition, multiple phase transitions were observed for $2Meq_2Zn$ and $5Meq_2Zn$, suggesting that these materials also exhibit polymorphism (see Figure 2.8).

For lithium mono(8-quinolinolato) chelates T_m increases in the order $Liq \ll 4MeqLi < 2MeqLi < 5MeqLi$. In this series, the 4Meq derivative does not exhibit the lowest melting transition, instead the unsubstituted material, Liq melts $\sim 30^\circ C$ lower than the methylated derivatives. Furthermore, both $4MeqLi$ and $5MeqLi$ melt at higher temperatures ($\sim 20-40^\circ C$ higher) than the corresponding methylated materials in the zinc bis- and aluminum tris-chelates. The T_m of $nMeqLi$ follows similar trend as the corresponding ligands.

The thermal stability trends for the Znq_2 chelates increases in the order $2Meq_2Zn \ll Znq_2 < 5Meq_2Zn \leq 4Meq_2Zn$, which is similar to what is observed for the corresponding metal tris-chelates. On the other hand, Li chelates exhibit the highest stability with thermal decomposition temperatures (maximum of DTGA) exceeding $500^\circ C$ for all materials.

Formation of the glassy state was accomplished by controlled cooling ($20^{\circ}\text{C}/\text{min}$) of the crystalline material immediately following the melting transition in the first heating cycle. Figure 2.9 illustrates the first and second heating cycle of Znq_2 chelates. In the second heating cycle, Znq_2 revealed a glass transition (T_g) at 177°C , a recrystallization exotherm (T_{c1}) at 272°C followed by three strong endothermic melting transitions. It is not known whether the three T_m peaks are due to polymorphism of the crystalline material or due to other species formed during the thermal experiment. Upon methyl substitution of Znq_2 , T_g increase in the order $2\text{Meq}_2\text{Zn} \ll \text{Znq}_2 < 4\text{Meq}_2\text{Zn} < 5\text{Meq}_2\text{Zn}$. Interestingly, the glass transition temperatures of Znq_2 and the methylated derivatives are almost identical to those of Alq_3 , Gaq_3 and its methylated derivatives. Furthermore, all Znq_2 chelates recrystallized upon heating beyond T_g , except $4\text{Meq}_2\text{Zn}$. Lithium mono(8-quinolinolato) chelates did not exhibit T_g nor other transitions in the second heating cycle.

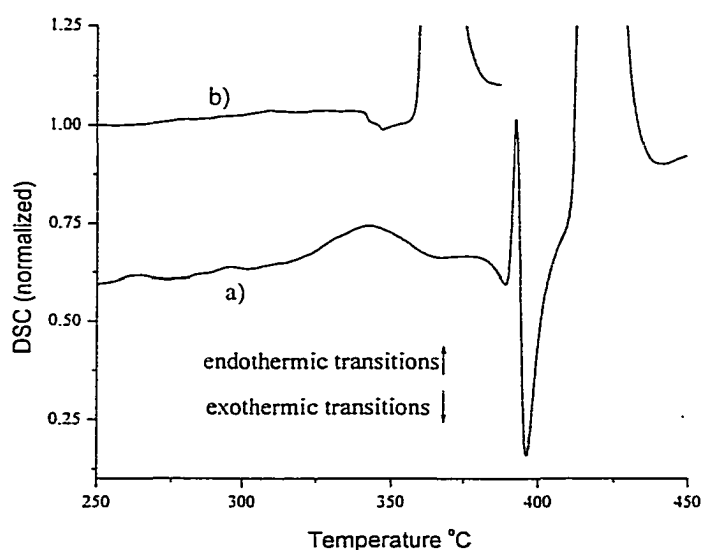


Figure 2.8. DSC scans showing distinct endothermic and exothermic transitions due to polymorphism for a) $\text{Alq}_3^{(25)}$ and less distinct transitions observed for b) Znq_2 .

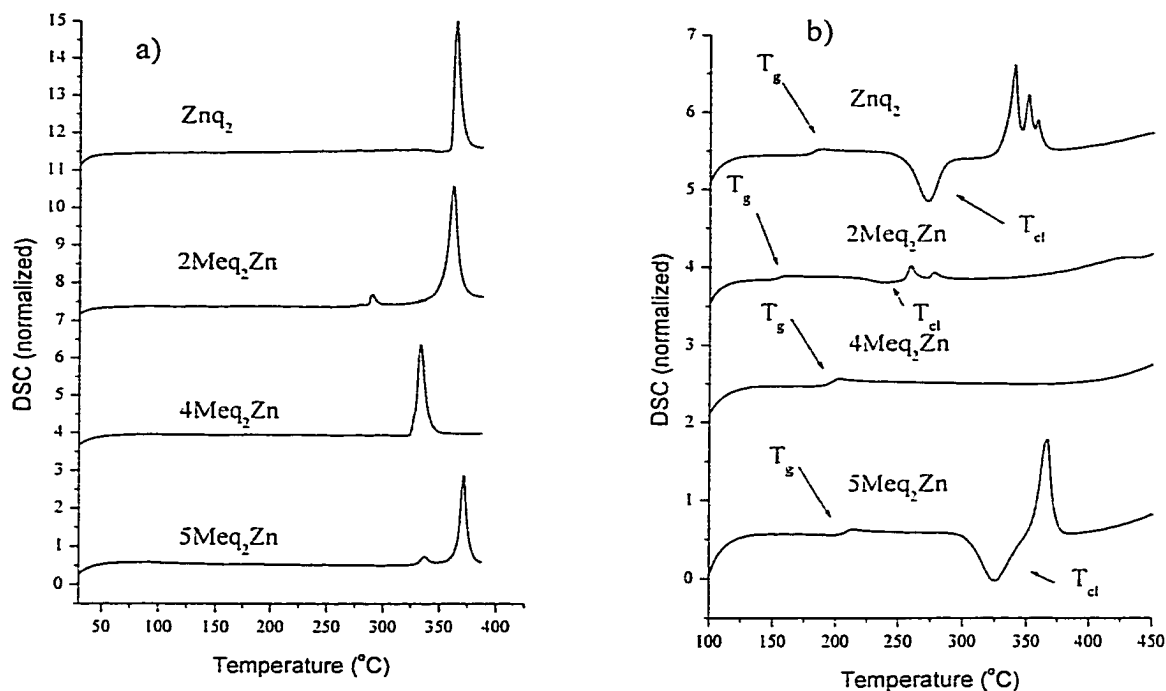


Figure 2.9. a) First heating cycle for $n\text{Meq}_2\text{Zn}$ chelates showing $4\text{Meq}_2\text{Zn}$ with lowest T_m ; and b) second heating cycle showing that $4\text{Meq}_2\text{Zn}$ forms a stable glass with no T_{cl} nor T_m transitions.

2.2.d Electrochemical Characterization

The use of solution electrochemical processes to describe electron transfer reactions in the condensed phase is based upon the assumption that the difference in ionization potentials and electron affinities of these molecules in solution are equal to or smaller than those same energy differences in the condensed phase. Although this is not the case, provided that we maintain constant experimental conditions for all the samples tested, results may be related to the material properties through the relative differences of oxidation and reduction within a series of sample.

In order to correlate the HOMO/LUMO energies of the metal quinolate chelates it was assumed that the relative difference of the HOMO/LUMO energies is approximately

equal to the difference of the oxidation/reduction potential. Since the reduction process is similar to electron injection (e^- put into LUMO) and the oxidation process is similar to hole injection (e^- taken out of HOMO).

$$E^{\circ'} = V_{\text{red}} - V_{\text{ox}} \approx \Delta(\text{HOMO-LUMO}) \quad (1)$$

All non-aqueous electrochemical measurements were performed using CH Instruments Model CH1660 and CH1680 potentiostat/galvanostat connected in series and controlled by the electrochemical software. The experiments were made in a one-compartment cell. The potential of the working electrode was measured against a 0.1 M Ag/Ag^+ reference electrode, and the counter electrode was a platinum sheet (6 cm^2). Solutions of Alq_3 and Znq_2 in dry acetonitrile (MeCN) at a 10^{-4} M concentration were prepared with 0.1 M tetrabutylammonium trifluoromethanesulfonate (TBATf) as a supporting electrolyte. The electrochemical cell was degassed at 5 min. with UHP nitrogen prior to analysis. The width of the potential window used for each experiment was selected such that the voltammetric peaks corresponding to oxidation and reduction processes were observed. Alq_3 and Znq_2 cyclic voltammograms were recorded with a scan rate of 1V/sec and 2V/sec, respectively

Alq_3 and Znq_2 were investigated under similar experimental conditions (i.e., concentration and degassing processes). At a single scan, Alq_3 exhibit a single oxidation reduction process. However, in order to acquire a CV scan that is representative of the solution, the sample must be allowed to equilibrate. Upon equilibration of Alq_3 and Znq_2 samples, these materials exhibited more than one redox process. Other reduction processes were not identified of its character or type of species. However, it is possible that they might be due to other oxidation processes for Alq_3 that have not been identified

or over oxidation which can lead to decomposition/speciation. The CV's for Alq₃ and Znq₂, which shows multiple scans, are depicted in Figure 2.10, where the oxidation and reduction peaks are emphasized. The oxidation and reduction potentials for Alq₃ were 2.40 V and +0.78 vs. Ag/Ag⁺ and were +2.4 V and -1.359 V vs. Ag/Ag⁺ for Znq₂. Other peaks are not identified. The peak potentials were used to estimate the differences in E° ($= V_{\text{red}} - V_{\text{ox}}$) values for the reduction and oxidation processes of Alq₃ and Znq₂ realizing that the peak potentials may deviate from the true E° 's by ± 0.05 V, because of the sweep rate dependence of the position of these voltammetric peaks.

Different authors have reported cyclic voltammogram and HOMO/LUMO energies for Alq₃ and Znq₂, but no direct comparison of their electrochemical analysis have been reported. It is important that samples are run under the same conditions in order to correlate the results, since cyclic voltammetry is diffusion dependent. Therefore, differences in concentrations, scan rates and instrumentation can significantly change the redox potentials. Anderson et al.⁽²³⁾ and Hopkins et al.⁽²⁾ reported the HOMO and LUMO energies for Alq₃ and Znq₂ determined from thin film and solution ultraviolet photoelectron spectroscopy (UPS) and absorbance/luminance data. The difference between the LUMO and the HOMO states should be the same or close to the value of the difference between the reduction and oxidation potentials based on the first assumption. The potential differences between the oxidation and reduction processes ($V_{\text{ox}} - V_{\text{red}}$) were very similar to the difference of the reported value for the $\Delta\text{HOMO/LUMO}$ for Alq₃,⁽²⁵⁾ but results for Znq₂ are not in agreement with the published $\Delta\text{HOMO/LUMO}$ differences via UPS (See Table 2.8). ¹H-NMR and UV-Vis spectroscopy experiments suggest that (see chapter 4), Znq₂ has strong solvent interactions, especially with polar solvents, such

as acetonitrile (which was used for CV characterization) that the oxidation and reduction potentials are probably not representative of a single Znq_2 species. However, if we look at the relative differences of the ΔG (Gibbs' Free Energy) values of Alq_3 and Znq_2 using the following equation:

$$\Delta G = -nFE^{\circ} \quad (2)$$

where n is the number of electrons transferred ($=1$); F (Faraday's Constant) = 9.64846×10^4 C/mol; and $E^{\circ} = V_{red} - V_{ox}$. The values found for Alq_3 and Znq_2 are -3.0682×10^5 J -3.6278×10^5 J, respectively. These values, if compared in terms of energies, might suggest that the variation for Znq_2 may be within the experimental error. Since this experiment was performed in solution, cyclic voltammetry may not be the best representation of the HOMO/LUMO energies of metal quinolates. However, if the experiment was carried out carefully and efficiently, results may be used to determine the relative differences and similarities in the reduction potentials that can be correlated to the charge injection properties of these materials. If accessible, a more accurate technique to extract HOMO/LUMO energies would be through x-ray spectroscopic experiments, which are carried out in the solid state.

Table 2.8 HOMO/LUMO Levels and Redox Potentials of Alq_3 and Znq_2 .

Metal Chelate	HOMO (eV) ± 0.15 eV	LUMO (eV) ± 0.15 eV	V_{red} vs. Ag/Ag^+ Expt. ^c	V_{ox} vs. Ag/Ag^+ Expt. ^c	$V_{ox} - V_{red}$ Expt. ^c	$\Delta_{HOMO-LUMO}$
Alq_3	6.65 ^a	3.43 ^a	-2.4	+0.78	3.18	3.22 ^a
Znq_2	6.42 ^b	3.16 ^b	-2.4	+1.3	3.76	3.26 ^b

^aAnderson, et. al.⁽¹⁵⁾ ^bHopkins, et. al.⁽²⁾ ^cResults from experiments.

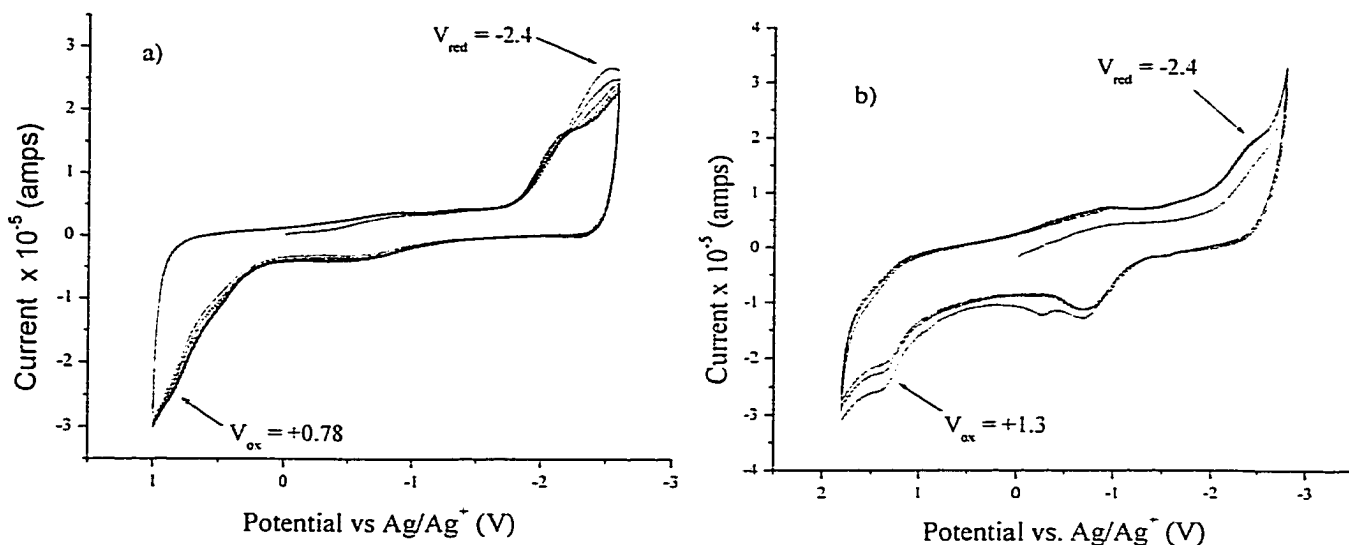


Figure 2.10. Cyclic voltammograms for a) Alq_3 and b) Znq_2 .

2.4 Synthetic Procedures

Zinc bis-(8-quinolinolato) (Znq): 0.89 g (4.0 mmol) of zinc acetate dihydrate was placed in a 150 mL Erlenmeyer flask and dissolved in 50 mL of methanol. In a separate flask, 1.16 g (8.0 mmol) of 8-quinolinol was dissolved in 200 mL of methanol. With stirring, the zinc salt solution was added to the ligand solution dropwise over a period of 5 minutes. Formation of a bright yellow precipitate was observed after the addition of ~ 5 mL of the zinc solution. The mixture was refluxed for three hours. After cooling, the precipitate was vacuum filtered and washed with concentrated sodium bicarbonate. It was then washed 3 times with alternating 20 mL increments of hot methanol and then warm deionized water. The crude material was air dried then dried under vacuum in the presence of desiccant at 110°C for 24 hours. The yield for the crude bright yellow amorphous dihydrated product was 1.41 g (88%). The material was purified by high-

vacuum gradient-temperature sublimation over a 3-day period ($\sim 10^{-7}$ Torr, up to 350°C). ^1H NMR (DMSO-d_6 , 25°C) $\delta\text{H}_2 = 8.47(\text{s})$; $\delta\text{H}_3 = 7.34$; $\delta\text{H}_4 = 8.27(\text{d})$; $\delta\text{H}_5 = 7.04$; $\delta\text{H}_6 = 7.25(\text{s})$; $\delta\text{H}_7 = 6.87$. $\text{C}_{18}\text{H}_{12}\text{O}_2\text{N}_2\text{Zn}$ (353.70), Calculated: C–61.13%; H–3.42%; N–7.92%; Experimental for purified compound: C–61.39%; H–3.55%; N–7.96%.

Zinc bis(2-methyl-8-quinolinolato) ($2\text{Meq}_2\text{Zn}$): Prepared according to a similar procedure described for Znq_2 , using 0.55 g (2.5 mmol) zinc acetate dihydrate dissolved in 25 mL methanol and 0.87 g (5.0 mmol) 2-methyl-8-quinolinol dissolved in 100 mL of methanol to yield 98% of an amorphous bright yellow precipitate. $2\text{Meq}_2\text{Zn}$ was purified by high-vacuum temperature-gradient sublimation in a three-day period (10^{-7} torr, up to 350°C). $\text{C}_{20}\text{H}_{16}\text{O}_2\text{N}_2\text{Zn}$ (381.74), Calculated: C–62.93%; H–4.22%; N–7.34%; Experimental for purified compound: C–58.22%; H–3.97%; N–6.41%.

Zinc bis(4-methyl-8-quinolinolato) ($4\text{Meq}_2\text{Zn}$): Prepared according to a similar procedure as described for Znq_2 , using 0.86 g (3.9 mmol) zinc acetate dihydrate dissolved in 50 mL methanol and 1.20 g (7.4 mmol) 4-methyl-8-quinolinol, as a ligand, dissolved in 200 mL of methanol. The mixture was refluxed for 3 hours. The precipitate was vacuum filtered and washed in similar manner as described for Znq_2 to yield 30% of an amorphous pale yellow powder. $4\text{Meq}_2\text{Zn}$ was purified by high-vacuum temperature-gradient sublimation over a three-day period (10^{-7} torr, up to 300°C). At 200°C , we observed a thin yellow film formation before crystal formation. As yellow crystal formed in the third cold zone, a purple colored microcrystals formed in the second zone which structural property was not identified. $\text{C}_{20}\text{H}_{16}\text{O}_2\text{N}_2\text{Zn}$ (381.74), Calculated: C–62.93%; H–4.22%; N–7.34%; Experimental for purified compound: C–62.80%; H–4.25%; N–7.32%.

Zinc bis(5-methyl-8-quinolinolato) (5Meq₂Zn): Prepared according to a similar procedure as described for Znq₂, using 0.28 g (1.3 mmol) zinc acetate dihydrate dissolved in 12.5 mL methanol and 0.40 g (2.5 mmol) 5-methyl-8-quinolinol, as a ligand, dissolved in 50 mL of methanol. The crude amorphous orange-yellow dihydrate 5Meq₂Zn was isolated in 92% yield. Purification by high-vacuum temperature-gradient sublimation was performed over a three-day period (10⁻⁷ torr, up to 320°C). As yellow-orange crystal formed in the third coldest zone, a red colored powder formed in the second zone which structural property was not identified. Samples that did not sublime and remained in the aluminum boat were also brownish-red powder. C₂₀H₁₆O₂N₂Zn (381.74), Calculated: C-62.93%; H-4.22%; N-7.34%; Experimental for purified compound: C-62.69%; H-4.10%; N-7.24%

Lithium (8-hydroxyquinoline) (Liq): 1.61 g (38 mmol) of LiOH hydrate was dissolved in 16 mL of deionized water to make a 10% w/w solution. In a separate Erlenmeyer flask 5.57 g (38 mmol) of the ligand, 8-hydroxyquinoline, was dissolved in 20 mL absolute ethanol with warming. The LiOH solution was added slowly to the cooled ligand solution. The ligand solution changed from brown to yellow after the addition of the LiOH solution. A white clumpy solid precipitate formed almost immediately. The heterogeneous solution was vacuum filtered immediately and the solid was washed with warm water and warm ethanol, alternately, to give a 95% crude yield. The crude solid material was recrystallized from absolute ethanol to give white needle-like crystal, which were subjected to a low vacuum sublimation and heated to 150°C in order to remove unreacted ligand. Final purification by high vacuum temperature-gradient was performed over a three-day period (10⁻⁷ torr, 350°C). The pure Liq was light yellow in color.

C₉H₆ONLi (151.09), Calculated: C–71.54%; H–4.00%; N–9.27%; Experimental for purified compound: C–71.29%; H–4.28%; N–9.27%.

Lithium (4-methyl-8-quinolinolato) (4MeqLi): 4MeqLi was prepared according to a similar procedure as described for Liq, using 0.8 g (3.6 mmol) LiOH dissolved in 8 mL deionized water to make 10% solution (w/w) and 0.6 g (3.5 mmol) 4-methyl-8-quinolinol, as a ligand, dissolved in 10 mL of absolute ethanol. LiOH solution was added dropwise into the ligand solution. A brownish precipitate formed ~30 minutes after all the LiOH solution was added. The precipitate was vacuum filtered and washed in similar manner as described for Liq to yield 28% of an amorphous greenish yellow precipitate. The resulting crude product was further purified by high-vacuum temperature-gradient sublimation in three-day period (10^{-7} torr, up to 350°C). C₁₀H₈ONLi (165.12), Calculated: C–72.74%; H–4.88%; N–8.48%; Experimental: C–72.35%; H–5.12%; N–8.50%.

Lithium (5-methyl-8-quinolinolato) (5MeqLi): 5me-Liq was prepared according to a similar procedure as described for Liq, using 1.3 g (31 mmol) LiOH dissolved in 13 mL deionized water to make 10% solution (w/w) and 5 g (31 mmol) 5-methyl-8-quinolinol, as a ligand, dissolved in 15 mL of absolute ethanol. LiOH solution was added dropwise into the ligand solution. Almost immediately, a yellow-orange precipitate formed. The precipitate was vacuum filtered and washed in similar manner as described for Liq to yield 88% of a crude amorphous yellow-orange precipitate. 5MeqLi was recrystallized from absolute ethanol and the orange micro crystalline solid was placed under low vacuum and heated to 150°C to remove unreacted ligand, then further purified by high-vacuum temperature-gradient sublimation in three day period (10^{-7} torr, up to 350°C) to

give a yellow microcrystalline solid. $C_{10}H_8ONLi$ (165.12), Calculated: C-72.74%; H-4.88%; N-8.48%; Experimental for purified compound: C-72.35%; H-4.70%; N-8.52%.

References

1. Padmaperuma, A. Substitution effects on metal quinolate chelate materials for organic electroluminescence applications. M.S. of Chemistry, University of Nevada Las Vegas, 2000.
2. Hopkins, T.A.; Meerholz K.; Shasheen, S.; Anderson, M.L.; Schmidt A.; Kippelen, B.; Padias, A.B.; Hall, K.H.; Peyghambrian, N.; Armstrong, N.R. Substituted aluminum and zinc quinolates with blue-shifted absorbance and luminance bands: synthesis and spectroscopic, photoluminescence, and electroluminescence characterization. *Chem. Mater*, 1996, 8(2), 344-351.
3. Nakamura, N; Wakabayashi, S; Miyairi, K; Fujii, T. A Novel Blue Light Emitting Material Prepared from 2-(o-hydroxyphenyl)benoxazol. *Chem. Lett.* 1994, 1741-1742.
4. Kai, Y.; Moraita, M; Yasuka, N.; and Kasai, N. The Crystal and Molecular Structure of Anhydrous Zinc 8-Quinolate Complex. *Bull. Chem. Soc. Jpn.*, 1985, 58, 1631-1635.
5. Hamada, Y.; Sano, T.; Fujita, N.; Fujii, T.; Nishio, Y.; and Shibata, K. Organic Electroluminescent Devices with 8-Hydroxyquinoline derivative-metal complexes as an emitter. *Jpn. J. Appl. Phys.* 1993, 32, L514-L515.
6. Hamada, Yuji. The Development of Chelate Metal Complexes as an Organic Electroluminescent Material. *IEEE Transactions on Electron Devices.* 1997, 44, 8, 1208.
7. Hamada, Y.; Sano, T.; Fujita, M; Fujii, T.; Nishio, Y.; and Shibata, K. Blue Electroluminescent in This Films of Azomethin-Zinc Complexes. *Jpn. J. Appl. Phys.* 1993, 32, 4A, L511-L513.

8. Hamada, Y.; Sano, T.; Fujii, H.; Nishio, Y.; Takahashi, H.; and Shibata, K. White-Light Emitting Material For Organic Electroluminescent Devices. *Jpn. J. Appl. Phys.* **1996**, 35, L1339-L1341.
9. Sapochak, L.S.; Padmaperuma, A.; Washton, N.; Endrino, F.; Schmett, G.; Marshall, J. and Fogarty, D. Effects of Systematic Methyl-Substitution of Metal (III) Tris(n-Methyl-8-Quinolinolato) Chelates on Material Properties for Optimum Electroluminescence Device Performance. *Submitted to J. Am. Chem Soc.* **2001**.
10. Cshulman, S. and Rietta, M. Formation of the Coordinate Complex between Lithium and 8-Quinolinol. *J. Pharm. Sci.* **1971**, 60, 11, 1763
11. Kathirgamanathan, P.; Electroluminescent Quinoltes. PCT/GB99/04024, Dec. **1998**
12. Schmitz, C.; Schmidt, H. and Thelakkat, M. Lithium-quinolate complexes as emitter and interfaces materials in organic light-emitting diodes. *Chem. Mater.* **2000**, 12, 3012-3019.
13. Baker, B. and Sawyer, D. Proton Nuclear Magnetic Resonance Studies of 8-Quinolinol and Several of its Metal Complexes. *Anal. Chem.* **1968**. 40, 13, 1945.
14. Schmidbaur, H.; Lattenbauer, J.; Dallas, L.; Muller, W.G. and Kumberger, O. Model Systems for Gallium Extraction I, Structure and Molecular Dynamics of aluminum and gallium tris(oxinates). *Z. Naturforsch.* **1991**, 46b, 901-911.
15. Kai, Y.; Morita, M.; Yasuoka, N. and Kasai, N. The Crystal Structure of Anhydrous Zinc 8-Quinolinolate Complex, $[Zn(C_9H_6NO)_2]_4$. *Chem. Soc. Jap.* **1985**. 58, 1631-1635.
16. Tackett, J.E. and Sawyer, D.T. Properties and Infra-red Spectra in the Potassium Bromide Region of 8-quinolinol and its Metal Chelates. *Inorg. Chem.*, **1964**, 8 692-696.
17. Magee, R.J and Gordon Lewis. The Infra-red Spectra of Chelate Compounds II. *Talanta*, **1963**, 10, 961-966.
18. Charles, Robert.G; Freiser, Henry; Friedel, Robert; Hillyard, Leland E.; and Johnston, William D. Infra-red Absorption Spectra of Metal Chelates Derived

- from 8-hydroxyquinoline, 2-methyl-8hydroxyquinoline, and 4-methyl-8-hydroxyquinoline. *Spectrochimica Acta*. **1956**, 8, 1-8.
19. Brinkmann, M.; Gadret, G.; Muccini, M.; Taliani, C.; Masciocchi, N.; and Sironi, A. *J. Am. Chem. Soc.* **2000**, 122, 5147.
20. Naito, K. and Muira, J. *Phys. Chem.* **1993**, 97, 6240
21. Juis, S.A.; Leles, M.; Caires C.; Boralle, N. and Ionashiro M. Thermal Decomposition of the Magnesium, Zinc, Lead and Niobium Chelates Derived from 8-Quinolinol. *J. Therm. Anal.* **1997**, 50, 625-632.
22. Petit, S. and Coquerel, G. Mechanism of Several Solid-solid transformations between dihydrated and anhydrous copper(II) 8-hydroxyquinolates. Proposition for a unified model for the dehydration of molecular crystals. *Chem. Mater.* **1996**, 8, 2247-2258.
23. Anderson, J.; McDonald, M.; Lee, P.; Anderson, M.; Ritchie, E.; Hall, H.; Hopkins, T.; Mash, E.; Wang, J.; Padias, A.; Thayumanavan, S.; Barlow, S.; Marder, S.; Jabbour, G.; Shaheen, S.; Kipplen, B.; Peyghambarian, N.; Wightman, R. and Armstrong, N. Electrochemistry and Electrogenenerated Chemiluminescence Processes of the Components of Aluminum
24. Ohkaku, N. and Kazuo, N. Metal Isotope Effect on Ligand-Metal Vibrations. Metal Complexes of 8-Hydroxyquinoline. *Inorg. Chem.* **1971**. 10, 4, 798.

CHAPTER 3

X-RAY ABSORPTION SPECTROSCOPIC CHARACTERIZATION

3.1 Background

In one of the most common x-ray spectroscopic techniques, x-ray absorption spectroscopy (XAS), promotion of atomic core electrons by selective photon absorption into bound valence states (or unoccupied states) maps normally unoccupied electronic states. A complementary technique, x-ray emission spectroscopy (XES), monitors x-rays emitted as the sample relaxes to fill a core hole created by x-ray absorption. If the electrons that fill this core hole come from the valence shell of the sample, then XES will directly probe the occupied valence states in a way analogous to the simple picture, in which molecular orbitals are built up using a linear combination of atomic orbitals (the LCAO-MO picture). Together, XAS and XES are useful techniques for determining the energies of the HOMO and LUMO levels in organic materials, which are important for understanding charge injection processes at OLED interfaces.

Important chemical information can be derived from the distinctive spectral features of the absorption cross-section in the region of an x-ray absorption edge. This technique is known as near-edge x-ray absorption fine-structure spectroscopy (NEXAFS, but sometimes called XANES for x-ray absorption near-edge spectroscopy). If the

excitation energy is near an absorption edge, an electron excited from a core level by x-ray absorption can make a transition to an unoccupied valence state at energies near the ionization threshold. If the core-hole long lifetime, then the intrinsic energy width of a core level is narrow, and the absorption spectrum (peak position, shape, and intensity) maps the energy distribution of unoccupied states to which the electron is excited.

The density of states is a signature of the chemical bonding and surrounding crystal structure of the absorbing atom. For example, in the metal (8-quinolinolato) chelate materials, there may be distinctive differences in the absorption into orbitals determined by the chemical bonds in which the atoms are participating that might reflect differences in the electronic structure of the ligand, because of the bonding interaction with different metal ions. The near-edge x-ray absorption spectrum therefore serves as a chemical and structural fingerprint.

3.2 Introduction

Curioni reported the first detailed electronic-structure characterization of Alq_3 using NEXAFS.⁽¹⁾ Since there are three 8-quinolinolato ligands in Alq_3 , the carbon-edge of Alq_3 was very complicated and the peaks were broad because of the overlapping contributions from more than one orbital set. Curioni compared the NEXAFS spectrum of Alq_3 with the calculated photoabsorption spectrum and assigned only the first three spectral peaks at lowest energy as transitions from the 1s core orbital to various unoccupied states corresponding to four different LUMO “sets” (I-IV) generated by the theoretical treatment of the molecule. The lowest energy LUMO state [LUMO (I)] was shown to contain the majority of electron density (available unoccupied states) mainly on

the pyridyl ring. The higher energy unoccupied orbital sets included: the LUMO+1 state (II) containing a symmetric distribution of electron density on the carbon atoms of both rings; LUMO+2 state (III) containing electron density mainly on the phenoxide ring oxygen and carbons but with some density on the pyridyl nitrogen; and LUMO+3 state (IV) containing an almost symmetric distribution of electron density over both rings and all atoms.

The experimental carbon edge spectrum reported by Curioni⁽¹⁾ and later by Padmaperuma⁽²⁾ for Alq₃ contained three dominant peaks. (See Figure 3.1) The lowest energy transition was well defined in the NEXAFS spectrum and assigned to a single transition, C 1s to LUMO(I) with the major contribution from C4 of the pyridyl ring. Two higher energy peaks were broadened and assigned as mixtures of contributions from the C 1s to LUMO (I), LUMO +1 (II) and LUMO+2 (III) orbital sets. For the lower energy of the two peaks, the maximum relative intensity was assigned to the C 1s to LUMO +2 (III) mainly from C5 of the phenoxide ring. The higher energy peak was assigned to the C 1s to LUMO +2 (III) of the carbon atoms at position 8 (directly bonded to the phenolic oxygen). Padmaperuma showed that there was no change in the C 1s spectrum upon substitution of the heavier ion, Ga⁺³ for aluminum, except for a shift to higher energy of peaks not assigned by Curioni.

For the nitrogen edge, three dominant peaks were assigned to the following transitions and are listed in order of increasing energy: N 1s to LUMO (I) (highest intensity transition); N 1s to LUMO + 2 (III); and N 1s to LUMO + 3 (IV). As predicted by theory, no peak was observed for the N 1s to LUMO + 1(II) set because the electron density is distributed primarily on the carbon atoms.

For the oxygen-edge, similar peaks from the N-edge spectrum were observed. These three peaks were assigned as: O 1s to LUMO (I) (highest intensity transition); O 1s to LUMO + 2 (III); and O 1s to LUMO + 3 (IV). Unlike the N-edge spectrum, the highest intensity was the transition O 1s to LUMO + 3 (III) state as predicted by the electron distributions of the LUMO sets.

Since electroluminescence is based on electron injection and transport, we use NEXAFS spectroscopy to determine differences and similarities of the electronic structures of the materials under study. This tool is crucial to our understanding of the device performance, as well as device operation. In this thesis the NEXAFS spectra of the C-, N- and O- edge for the nMeq₂Zn and nMeqLi chelates are presented and compared with the results previously obtained by Padmaperuma for Alq₃ and its methylated derivatives.⁽²⁾ By reducing the number of 8-quinolinol ligands from 3 (Alq₃) to 2 (Znq₂) to (1) Liq, we hoped to simplify the NEXAFS spectra and to determine the orbital contributions of the higher energy transitions. However, we show that the NEXAFS spectra of both Znq₂ and Liq are similar to those of the metal tris-(8-quinolinolato) chelates but with significant changes in intensity of the transitions. For the Liq materials additional peaks are observed in all spectra. We interpret this data in terms of the increased ionic character of the metal-ligand bond for Liq than in Znq₂ and much less so for Alq₃.

3.3 Experimental Method

X-ray absorption spectroscopy experiments were performed at the Advanced Light Source (ALS), Lawrence Berkeley National Lab (LBNL). The storage ring at the

ALS has a stored electron beam with energy of 1.9 GeV. The available photon energies extend from the far IR to x-rays (15 KeV). The ring is optimized for extremely high brightness in the vacuum UV and soft x-ray ranges. All experiments were performed on beamline 6.3.2 which is a bending magnet beamline dedicated to extreme ultraviolet (EUV) and soft x-ray reflectometry and scattering with high spectral purity and wavelength accuracy. The beamline has a photon energy range from 50 to 1300 eV and photon flux of 10^{11} photons/sec/0.01%BW at 100 eV.⁽¹⁾

Unoccupied electronic states of metal chelates were probed using NEXAFS with a reflectometer chamber at the beamline 6.3.2. The order sorter was set at the off position during the experiments and exit slits were set to 50x50 micrometer. The sample was placed at 90° angle to the beam. The 600 lines/mm gratings were selected for all studies. Data was collected at a rise time of 100 ms and presample decay of 300 ms. All samples were run at single scan.

X-ray absorption was performed via the total electron yield method. When the x-ray beam impinges on the sample a core level electron (1s) is promoted to a higher unoccupied level. This gives rise to an excited molecule, which does not bear a charge, thus a core hole is created. This excited state can decay in many ways, including: recombination of the hole and the excited electron, production of photoelectrons, and Auger emission, the latter being the major pathway of decay. Depending on the penetration depth, these electrons can escape from the sample and are measured using detectors placed close to the sample. The current necessary to balance the charge, referred to as the drain current is proportional to the total amount of electrons emitted by the molecule. The total electron yield method is preferred over XAS via transmission

because there is no need to have a transparent substrate and there may be less charging up of the organic material that can lead to decomposition during the experiment.

NEXAFS spectra were generated as the change in drain current as a function of photon energy of the x-ray beam. There must be an electrical connection between the sample and the detector; thus the sample must be in contact with a conducting substrate. Vapor-deposited films on copper substrates were used. All absorption spectra were normalized to the incident photon flux, which was measured with a photodiode. The energy calibration was not done using standards; rather, an internal energy calibration was made through a carbon dip observed in the incident photon flux (I_0). This may have shifted the energies of all the spectra by a constant amount. The resolution of the peak energies is ± 0.1 eV. All the samples were run in the similar instrument; therefore general statements on the differences of the relative intensities of the peaks within the same spectra should be viable.

3.4 Results and Discussion

3.4.1 Effect of Metal Ion Substitution

The NEXAFS carbon K-edges of Alq_3 , Znq_2 and Liq are shown in Figure 3.1, where four major peaks are labeled (1)C – (3)C with a fourth peak observed only for Liq, labeled (4)C. The peak energies and intensities are listed in Table 3.1. Compared to Alq_3 , the lower energy peaks, (1)C and (2), of both Znq_2 and Liq were less intense than the higher energy peak (3)C. The most significant decrease in intensity was observed for peak (1)C, this peak was assigned by Curioni as the transition from $\text{C}1s$ to LUMO (I) state, where theoretical treatment of Alq_3 showed that LUMO (I) has the majority of the

available unoccupied states distributed over the pyridyl ring.⁽¹⁾ A decrease in intensity of this transition suggests that the electronic distribution on the pyridyl ring changes upon metal ion substitution to make this transition less probable. This may occur if the metal-ligand bonding becomes more ionic, so that the lone pair electrons on the phenoxide oxygen are delocalized into the quinolate ligand providing a more even electron distribution between the two ring systems, as shown by the resonance structures in Figure 3.1. The effect is largest for Liq, which is expected to exhibit the most ionic character. Figure 3.2 depicts a cartoon of the probable electron distribution on the quinolate ligands for the Mq_n , where darker shading means more electron distribution and lighter shade means less electron density. Figure 3.3 ranks the Mq_n according to the nature of the metal ligand (M-q) bond.

Interestingly, Liq exhibits an additional strong peak observed at 290 eV ((4)C), which was not observed for Alq₃ or Znq₂. Previous investigations of smaller organic molecules suggests that a peak appearing at 290 eV is characteristic of a transition to the unoccupied anti-bonding states of the π electrons present in the C=O functional group⁽⁴⁾, which could be possible if Liq is truly ionic (see Figure 3.1).

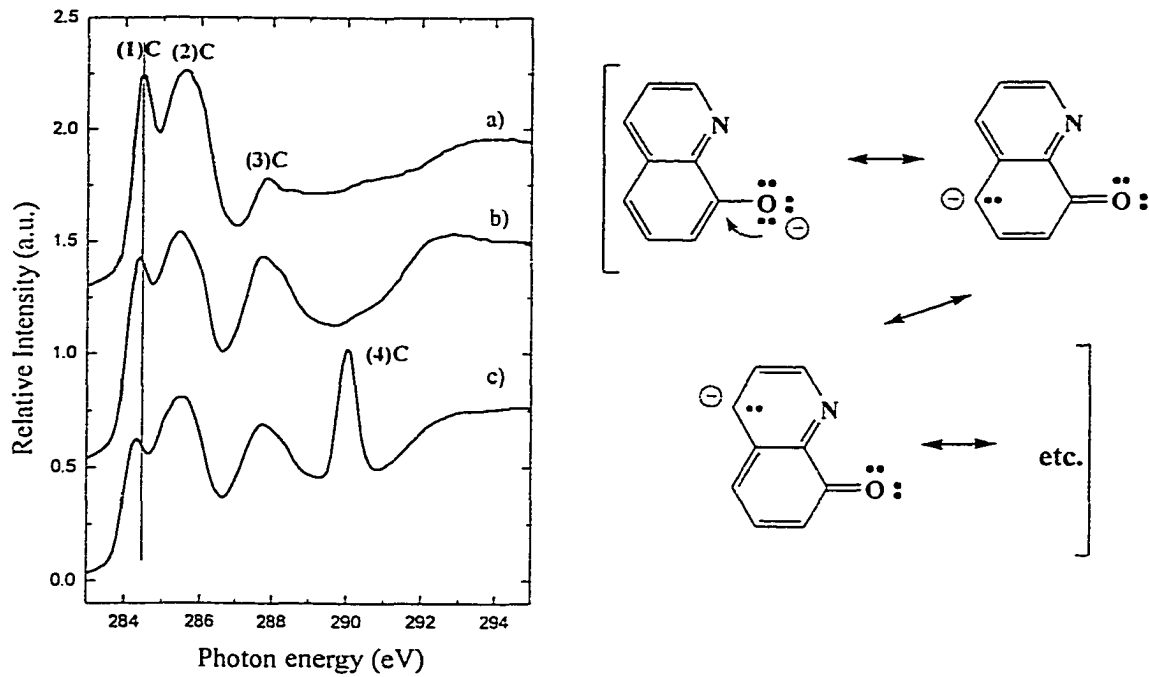


Figure 3.1 C 1s NEXAFS spectra of a) Alq₃; b) Znq₂ and c) Liq, and resonance structures of anionic 8-quinolinolate.

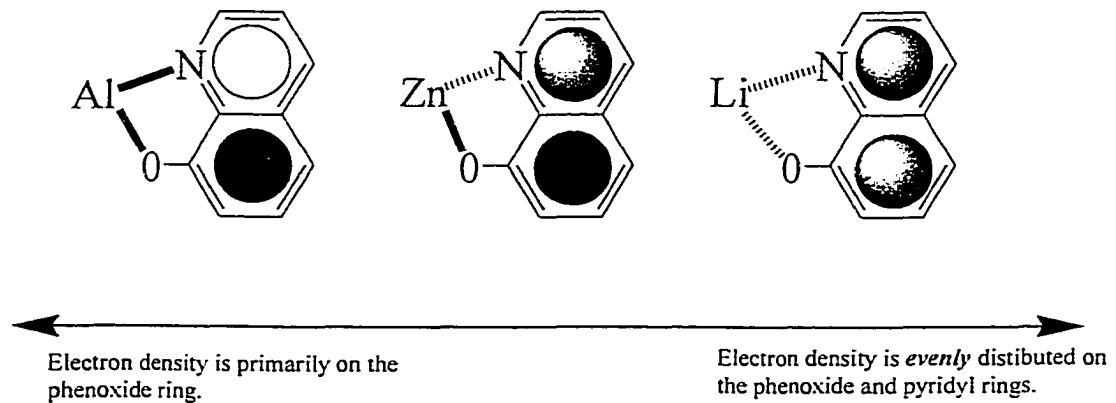


Figure 3.2. Illustration of the effects of metal ion substitution on the electron distribution of the quinolate ligand, where the circles within the aromatic rings represent electron density. A Dark shaded circle indicates high electron density, whereas a light shaded circle indicates low electron density.

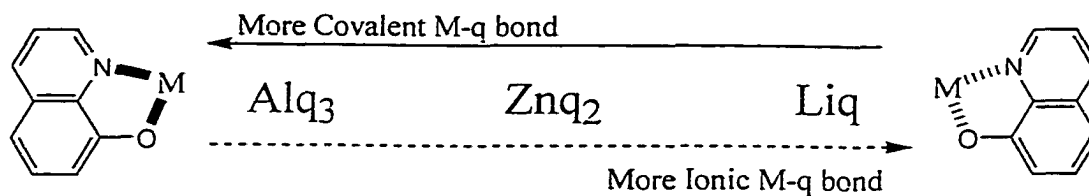


Figure 3.3. Schematic representation of the metal ligand (M-q) bonding character.

Table 3.1 C1s NEXAFS Data for Mq_n Chelates.

Peak	Alq ₃		Znq ₂		Liq	
	Energy (eV)	Intensity	Energy (eV)	Intensity	Energy (eV)	Intensity
(1)C	284.5	1.322	284.4	0.932	284.0	0.627
(2)C	285.6	1.342	285.4	1.042	285.5	0.808
(3)C	287.8	0.882	287.6	0.934	287.7	0.695
(4)C	n.o.	n.o.	n.o.	n.o.	290.0	1.025

n.o = not observed

3.4.2 Effect of Methyl Substitution

3.4.2.a Zinc Bis-Quinolinolato Chelates

The NEXAFS C 1s and N 1s spectra for the $nMeq_2Zn$ chelates are shown in Figures 3.4. The corresponding peak energies and relative intensities of the labeled peaks are listed in Tables 3.2 and 3.3.

The effect of ligand methylation of Znq_2 on the C 1s spectra were similar to that reported by Padmaperuma for Alq_3 and Gaq_3 methylated derivatives. The lowest energy peak ((1)C) was shifted to higher energy only for $4Meq_2Zn$. However, for both $4Meq_2Zn$ and $5Meq_2Zn$, the peak (2)C was shifted to lower energy, with an appearance of a

shoulder on the high energy side, and peak (3)C was shifted to higher energy compared to Znq_2 .

The N 1s spectra for $nMeq_2Zn$ chelates was also similar to what was observed for all $nMeq_3Al$ chelates previously.⁽²⁾ The lowest energy peak, (1)N was sharpest and had the highest intensity, and peak (3)N for $4Meq_2Zn$ was slightly shifted to lower energy compared to Znq_2 . Previously, Padmaperuma proposed two possible explanations for the shifts upon methylation at the C4-position. One, the electron donating character of methyl group may stabilize the nitrogen K-hole due to an increase of electron density on the nitrogen and two, upon methyl substitution, the electron distribution of this LUMO set is no longer similar to that of unsubstituted analogue. A theoretical treatment of the methyl-substituted metal chelates is necessary before answers can be established.

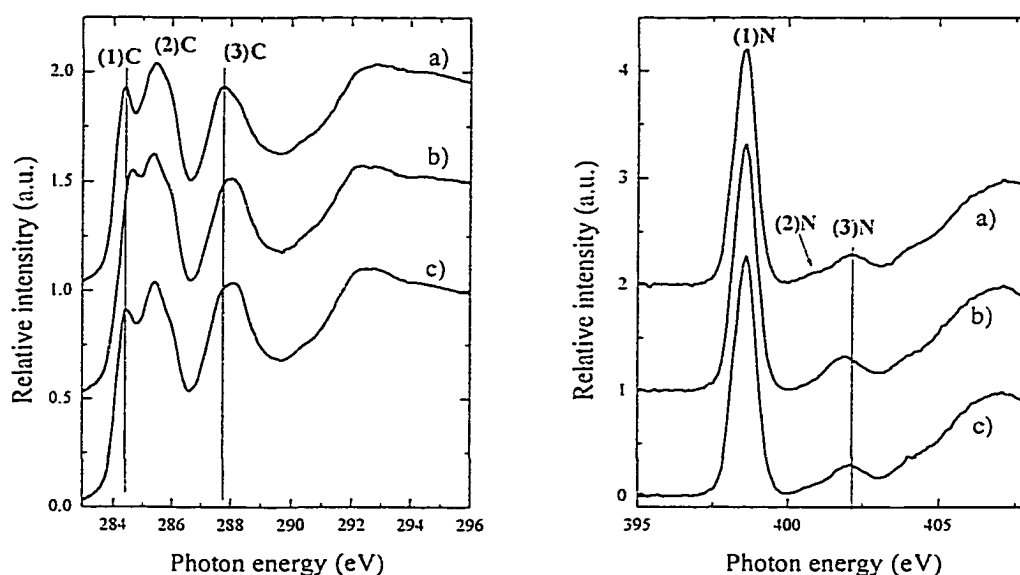


Figure 3.4. C 1s and N 1s NEXAFS spectra for a) Znq_2 ; b) $4Meq_2Zn$ and c) $5Meq_2Zn$. showing the effects of methylation of the ligand on peak energies.

Table 3.2 C 1s NEXAFS Data for nMeq₂Zn chelates.

Peak	Znq ₂		4Meq ₂ Zn		5Meq ₂ Zn	
	Energy (eV)	Intensity	Energy (eV)	Intensity	Energy (eV)	Intensity
(1)C	284.4	0.932	284.6	1.053	284.4	0.914
(2)C	285.4	1.042	285.3	1.112	285.3	1.043
(3)C	287.6	0.934	288.1	1.015	288.1	1.037

Table 3.3 N 1s NEXAFS Data for nMeq₂Zn Chelates.

Peak	Znq ₂		4Meq ₂ Zn		5Meq ₂ Zn	
	Energy (eV)	Intensity	Energy (eV)	Intensity	Energy (eV)	Intensity
(1)N	398.6	2.208	398.6	2.315	398.6	2.276
(2)N	400.8	0.117	400.8	0.093	400.8	0.109
(3)N	402.1	0.296	401.9	0.332	402.1	0.308

3.4.2.b Lithium Quinolinolato Chelates

The C 1s and N 1s NEXAFS spectra for nMeqLi chelates are shown in Figure 3.5 and the relative energies and intensities of the peaks are listed in Tables 3.4 and 3.5.

All nMeqLi exhibited the same peaks as shown for Liq. In addition, trends upon methyl substitution on the C 1s and N 1s spectra for Liq are similar to what was observed for all nMeq₃Al and nMeq₂Zn chelates as discussed above for Znq₂ materials, except for new peaks identified only for nMeqLi. Where methylation on the 4C- position shifts the (1)C peak to higher energy and (3)N peak to lower energy vs. Liq. Also, substitution on the 4C- and 5C- position shifts (3)C to lower energy, relative to the unsubstituted analogue. Compared to the metal tris- and bis- quinolates, new peaks were observed at higher energy (~290 eV) for C 1s NEXAFS and lower (~396.7 eV) and higher (~404.1

eV) for N 1s NEXAFS of nMeqLi chelates. Also, for Alq₃ and Znq₂, there were no observable changes in the relative intensities of the peaks upon methyl substitutions unlike nMeqLi chelates. In figure 3.5, C 1s NEXAFS for Liq shows that peaks for (1)C and (2)C have similar and higher intensity than (3)C. However, both 4MeqLi and 5MeqLi shows that peaks for (1)C and (2)C have lower intensities than (3)C. The reasons for the relative differences in intensities are not known. Therefore, theoretical treatment of this molecule is required in order to present different possibilities. Previous attempts to acquire the O 1s NEXAFS for Alq₃ and Znq₂ were unsuccessful due to the oxidation of the aluminum substrates used, which is known to cause interference in the data acquisition. Now that we are using copper substrates, we are more successful in performing these experiments. The O1s NEXAFS spectra of nMeqLi are depicted in Figure 3.6 and the peak energies and intensities are listed in Table 3.6. The only reference used to compare our results was the O 1s NEXAFS and calculated photoabsorption of Alq₃ reported by Curioni et al. Our O 1s NEXAFS for nMeqLi are very different (peak shapes and intensities) from the reported Alq₃. Peak energies and intensities are listed in Table 3.6. There were no significant shifts in the energies, as well as intensities upon methyl substitution of Liq.

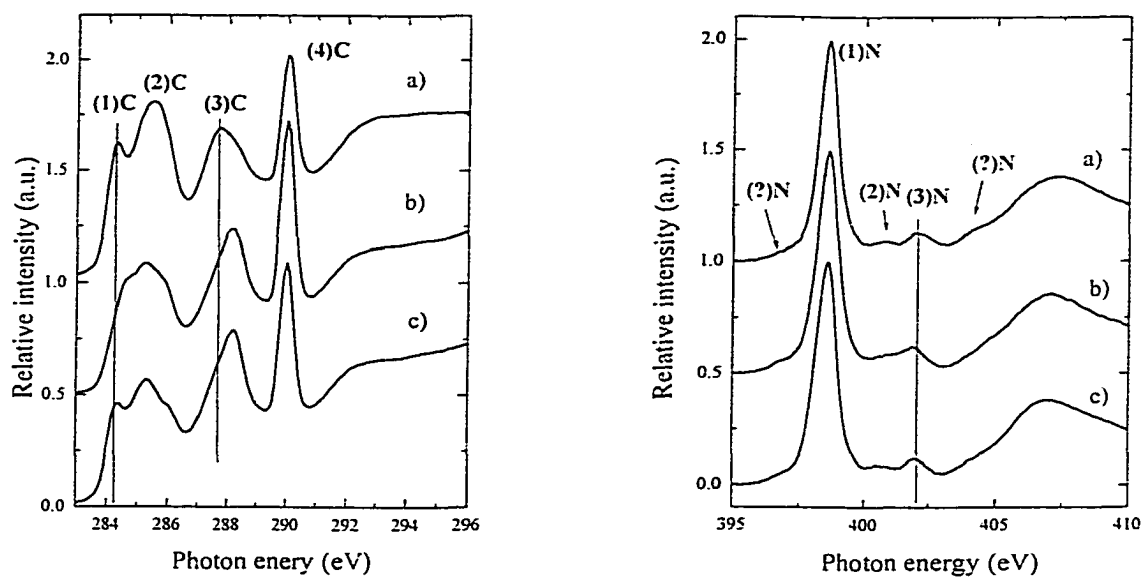


Figure 3.5. C 1s and N 1s NEXAFS of a) Liq; b) 4MeqLi; and c) 5MeqLi showing the effects of methylation of the ligand on the peak energies.

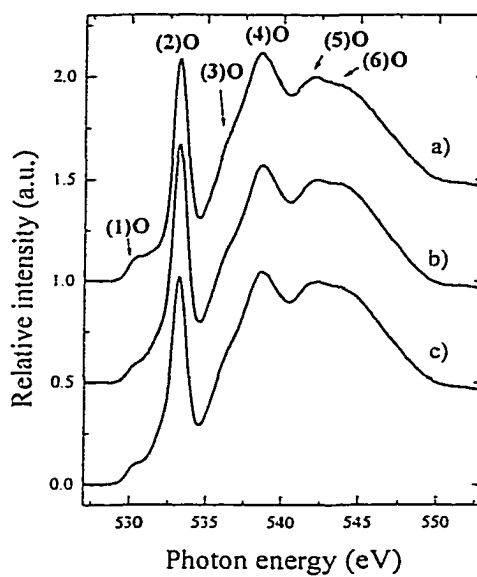


Figure 3.6. O 1s NEXAFS of a) Liq; b) 4MeqLi; and c) 5MeqLi showing no effects of methylation of the ligand on the peak energies.

Table 3.4 C 1s NEXAFS nMeqLi.

Peak	Liq		4MeqLi		5MeqLi	
	Energy (eV)	Intensity	Energy (eV)	Intensity	Energy (eV)	Intensity
(1)C	284.0	0.628	284.7	0.524	284.4	0.464
(2)C	285.5	0.808	285.3	0.587	285.3	0.571
(3)C	287.7	0.695	288.2	0.740	288.2	0.792
(4)C	290.0	1.025	290.0	1.227	290.0	1.092

Table 3.5 N 1s NEXAFS nMeqLi.

Transition	Liq		4MeqLi		5MeqLi	
	Energy (eV)	Intensity	Energy (eV)	Intensity	Energy (eV)	Intensity
(1)N	398.1	1.000	398.6	0.999	398.6	1.000
(2)N	400.8	0.089	400.9	0.086	400.9	0.086
(3)N	402.0	0.128	401.9	0.123	402.0	0.119

Table 3.6 O 1s NEXAFS nMeqLi

Peak	Liq		4MeqLi		5MeqLi	
	Energy (eV)	Intensity	Energy (eV)	Intensity	Energy (eV)	Intensity
(1)O	530.6	0.124	530.6	0.098	530.6	0.107
(2)O	533.2	1.089	533.2	1.173	533.2	1.022
(3)O	536.7	0.762	536.7	0.708	536.7	0.698
(4)O	538.6	1.116	538.7	1.070	538.7	1.045
(5)O	542.1	0.998	542.3	1.000	542.4	1.000
(6)O	543.8	0.960	543.9	0.978	543.8	0.971

Reference

1. Curioni, A.; Andreoni, W.; Treusch, R.; Himpsel, F. J.; Haskal, E.; Seidler, P.; Heske, C.; Kakar, S.; Van Buuren, T.; Terminello, L.J. Atom-resolved electronic spectra for Alq₃ from theory and experiment. *Appl. Phys. Lett.* **1998**, 72(13), 1575-1577.
2. Padmaperuma, A. Substitution Effects of Metal Quinolate Chelate Materials for Organic Electroluminescence Applications. M.S. in Chemistry, University of Nevada Las Vegas, **2000**.
3. Chen C.H and Shi, J. Metal chelates as emitting materials for organic electroluminescence. *Coor. Chem Rev.* **1998**, 171, 161-174.

CHAPTER 4

PHOTOPHYSICAL CHARACTERIZATION OF
METAL-QUINOLINOLATO CHELATES

4.1 Introduction

The optical transition responsible for photoluminescence in metal (8-quinolinolato) chelates is centered on the organic ligands. This transition is due to a π - π^* charge-transfer from the electron rich phenoxide ring (location of the HOMO) to the electron deficient pyridyl ring (location of the LUMO).⁽¹⁾ Theoretical calculations of the excited state energies suggest that substitution on the ligand moiety significantly change the photophysics of these materials.⁽²⁾ For example, substitution of an electron donating group on the pyridyl ring will raise the energy of the LUMO and that on the phenoxide ring will raise the energy of the HOMO. These effects will result in a blue- and red-shift of the absorption energies, respectively.

These energy shifts were confirmed experimentally through investigation of the photophysics of $n\text{Meq}_3\text{M}$ chelates. Upon methyl-substitution (weak electron donor) on the quinolate ligands of Alq_3 , the absorption energy shifts were largest for C-5 methylation (red-shift, $>1000\text{ cm}^{-1}$) and very small for C-3 and C-4 methylation (blue-shift, $<350\text{ cm}^{-1}$).^(3,4) Substitution of the heavier metal ion Ga^{+3} caused a red-shift of absorption compared to the $n\text{Meq}_3\text{Al}$ chelates because of the heavy atom effect discussed

previously,⁽⁵⁾ but the trends in absorption shifts upon methylation of the 8-quinolinol ligand were identical to the aluminum series. The effect of methyl-substitution on the photoluminescence (PL) emission energies were similar to those observed for absorption. 4Meq₃M (3 times Mq₃) had the highest PL efficiency (ϕ_{PL}), whereas the 5Meq₃M chelates exhibited significantly lower ϕ_{PL} (approximately 3 times less than Mq₃).

The large enhancement in ϕ_{PL} by C-4 methylation of the ligands in Al and Ga tris (8-quinolinolato) chelates was attributed to reduced energy loss in the excited state vibrational manifold, as indicated by the smaller Franck-Condon shifts (Δ 's) and narrower full width maxima (FWHM). This was supported by a study of the infrared absorption and photoluminescence of matrix-isolated and thin-film samples of Alq₃ and 4Meq₃Al compared to vibrational spectra based on density functional calculations.⁽⁶⁾ There, the PL spectra of matrix-isolated molecules revealed vibronic bands characterized as a combination of ring breathing and metal-ligand stretching modes. Kushto, noted that there was a lack of metal-ligand character in the vibrations for 4Meq₃Al as compared to Alq₃. This suggests that the stronger coupling of the metal-ligand stretching coordinates to the electronic transition in Alq₃ may provide additional paths for nonradiative decay. This pathway is less available for 4Meq₃Al, giving rise to a higher ϕ_{PL} .

Since photoluminescence results from an electronic transition centered on the 8-quinolinolato ligand, upon methyl substitution similar trends in the absorption energies, as well on relative ϕ_{PL} , were observed for nMeq₂Zn and nMeqLi. However, even though the metal ion is not directly involved in the electronic transition responsible for PL, the metal ion affects the photophysical properties through differences in coordination geometry and metal-ligand bonding character as compared to the tris-chelate series. For example, the

absorption energies of $n\text{Meq}_3\text{Al}$ chelates are almost identical in solvents of different polarities.⁽⁴⁾ For $n\text{Meq}_2\text{Zn}$ and $n\text{MeqLi}$ chelates, on the other hand, because the number of ligands coordinated to the metal ion is reduced, and therefore solvents are more susceptible to interact with both the ligand and the metal ion, thereby inducing strong solvent effects on the photophysical properties.

Furthermore, Chen have suggested that the metal ligand (M-q) bonding character of Znq_2 was more ionic than Alq_3 since the PL λ_{max} for Znq_2 was red shifted compared to Alq_3 .⁽²⁾ No additional experimental evidence was provided to support this conclusion. For Liq , it has not been well established whether the nature of the M-q bonding is covalent or ionic.⁽⁷⁾ Results from the x-ray spectroscopic experiments reported in chapter 3 of this thesis suggested that the electronic structure of the quinolinolato ligand changes upon metal ion substitution, and it was inferred that the electrons of the ligand are more evenly distributed over both the pyridyl and the phenoxide rings going from Alq_3 to Znq_2 to Liq (See Figure 3.2). The solvent dependences of the absorption spectra for Znq_2 and Liq chelates presented below provide additional support for the more ionic nature of the M-q bonding character of Znq_2 and Liq vs. Alq_3

4.2 Experimental

Absorption and photoluminescence (PL) characterization were performed on dilute ($\sim 10^{-5}$ M) methylene chloride (CH_2Cl_2), dimethyl formamide (DMF), and methanol (MeOH) solutions. Absorption spectra were recorded with a Varian Cary 3Bio UV-vis spectrophotometer and PL spectra were obtained with a SLM 48000 spectrofluorimeter. Extinction coefficients, $\epsilon(\lambda_{\text{max}})$ for the lowest energy absorption peak (λ_{max}) in Alq_3 ,

nMeq₂Zn and nMeqLi chelates were determined from solutions in CH₂Cl₂ at 10⁻⁵-10⁻⁴ M concentrations where the absorbance at λ_{max} was <0.5. Relative PL quantum efficiencies (ϕ_{PL}) were determined from DMF and CH₂Cl₂ solutions by adjusting the concentration of the sample so that the optical densities at 390 nm (excitation wavelength) were ~0.2. Quantum efficiencies (ϕ_{PL}) were also determined at 365 nm excitation wavelength and the differences are within the instrument's experimental error ($\lambda_{\text{max}} = \pm 3$ nm). PL quantum yields were calculated relative to the known value for Alq₃ in DMF ($\phi_{\text{PL}} = 0.116$)⁽⁸⁾ and CH₂Cl₂ are reported normalized to Alq₃ (Alq₃ = 1.0). The emission maxima (λ_{PL}), full width half maxima (FWHM), and the area under the emission spectra were calculated using the graphing software, Origin. Samples were run on the same day and all the instrument parameters were held constant. Each series of samples were measured in triplicate.

4.3 Absorption Spectroscopic Results

4.3a Effect of Metal Ion Substitution: Solvent Dependences of Absorption Spectra

Absorption spectra of Alq₃, Znq₂ and Liq in CH₂Cl₂ and DMF are depicted in Figure 4.1. All metal (8-quinolinolato) chelates exhibit a broad absorption peak accompanied by higher energy bands appearing as shoulders. The shapes of the absorption spectra of Alq₃, Znq₂ and Liq were virtually identical in CH₂Cl₂, but the longest wavelength transition (λ_{max}) was blue shifted (682 cm⁻¹ and 1928 cm⁻¹, respectively).

There were no differences between the absorption spectra of Alq₃ and all other metal tris(8-quinolinolato) chelates in CH₂Cl₂ and the more polar solvent, DMF.⁽³⁾

However, Znq₂ and Liq exhibited large red shifts for the longest wavelength transition with a decrease in intensity relative to the shortest wavelength transitions, which no longer appeared as shoulders in DMF. These results are depicted in Figure 4.1.

To further investigate the differences between the tris- and bis- chelates, the absorption spectra of Alq₃ and Znq₂ chelates were obtained in methanol (MeOH) (See Appendix III). Alq₃ and 2Meq₂Zn exhibited a large blue shift relative to the λ_{\max} (CH₂Cl₂) (965 cm⁻¹ and 1327 cm⁻¹, respectively), whereas Znq₂ and 4Meq₂Zn exhibited a small red shift (279 cm⁻¹ and 213 cm⁻¹, respectively). There were no differences between the absorption spectra for 5Meq₂Zn in MeOH and CH₂Cl₂. The solvent dependence of the absorption energies were also observed for all methylated zinc and lithium chelate derivatives (See Tables 4.1 and 4.2).

Absorption spectra of the nMeq₂Znq and nMeqLi chelates were also obtained for vapor-deposited films grown on quartz slides. The spectral features are very similar to those run in CH₂Cl₂ solution; therefore the PL properties in CH₂Cl₂ are more representative of the solid state.

The extinction coefficient (ϵ) for λ_{\max} in CH₂Cl₂, was also determined by using Beer's law (1), where A = absorption units at λ_{\max} ; b = path length (= 1 cm); and c = concentration (mol/L).

$$A = b c \epsilon \quad (1)$$

ϵ is indicative of the probability of the longest wavelength transition (λ_{\max}) and decreases in the order: Liq < Znq₂ < Alq₃.

Table 4.1 Absorption Data for nMeq₂Zn in Different Solvents.

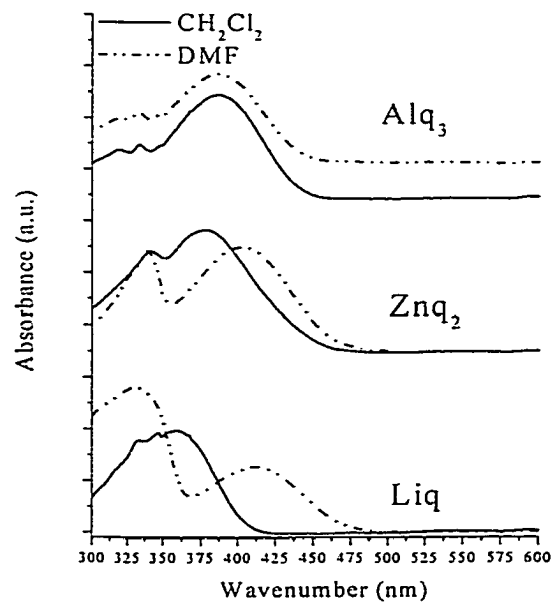
Metal Chelate nMeq ₂ Zn	Absorption CH ₂ Cl ₂ λ _{max} (nm)	Absorption DMF λ _{max} (nm)	Absorption MeOH λ _{max} (nm)	Absorption Film λ _{max} (nm)	ε
Znq ₂	341, 378	327 ^s , 339, 402	321 ^s , 324, 381	342, 381	4.559E+03
2Meq ₂ Zn	321, 340, 385	326 ^s , 340, 386	321 ^s , 340, 369	---	---
4Meq ₂ Zn	340, 371	326 ^s , 339, 398	321 ^s , 334, 377	342, 378	5.705E+03
5Meq ₂ Zn	346, 393	346, 419	328 ^s , 341, 393	345, 355, 397	4.716E+03

s = shoulder.

Table 4.2 Absorption Data for nMeqLi in Different Solvents.

Metal Chelate nmeqLi	Absorption CH ₂ Cl ₂ λ _{max} (nm)	Absorption DMF λ _{max} (nm)	Absorption Film λ _{max} (nm)	ε
Liq	331, ^s 361	309 ^s , 330, 412	338, 346, 359	1.249E+03
4MeqLi	334 ^s , 357	307 ^s , 329, 406	336 ^s , 346, 361	n.d.
5MeqLi	n.d.	340, 428	344, 376	n.d.

s = shoulder; n.d. = not determined because of insolubility.

**Figure 4.1. Absorption spectra of Mq_n in CH₂Cl₂ and DMF showing the effects of solvent polarity on the absorption energies and intensities.**

4.3b Effect of Methylation of the 8-Quinolinolato Ligand on Absorption Energies

Figures 4.2 and 4.3 show the absorption spectra of $n\text{Meq}_2\text{Zn}$ and $n\text{MeqLi}$ chelates in CH_2Cl_2 and DMF, respectively. Consistent with the absorption energy shifts upon methylation of the ligand for metal tris-chelates, the lowest energy absorption band was blue-shifted for C4-methylation and red-shifted for C5-methylation relative to the unsubstituted analogues for both the zinc and lithium chelates (see Table 4.3).

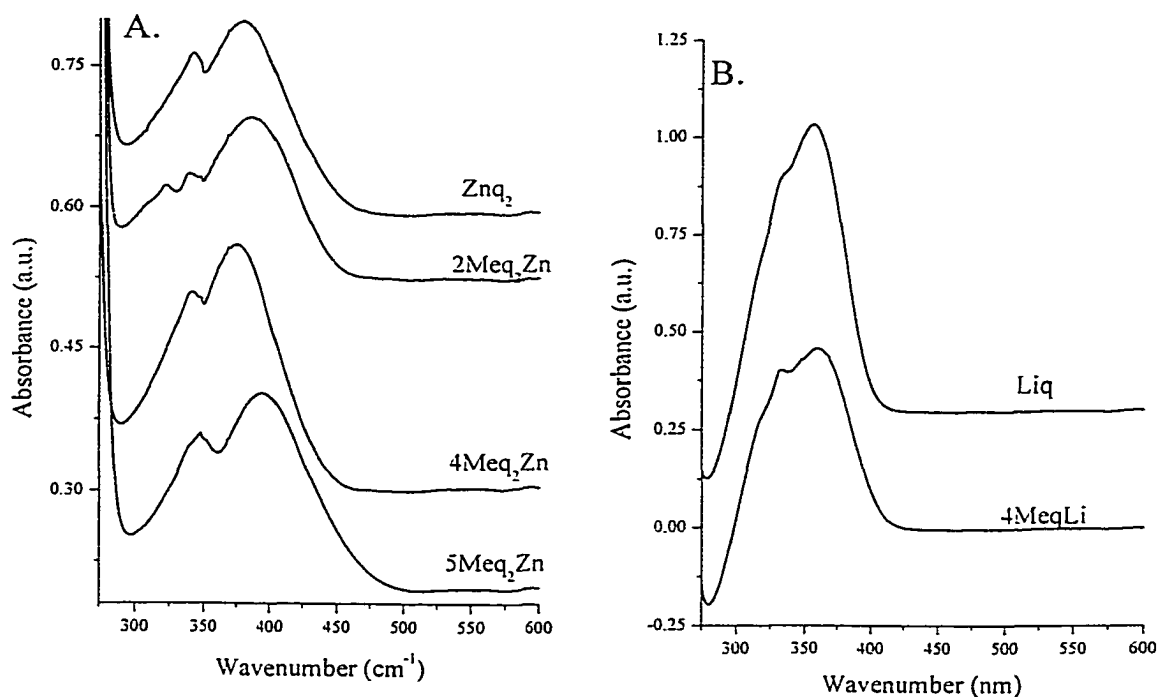


Figure 4.2. Absorption spectra of A. $n\text{Meq}_2\text{Zn}$ and B. $n\text{MeqLi}$ in CH_2Cl_2 showing the effects of methyl substitution on the absorption energies and intensities.

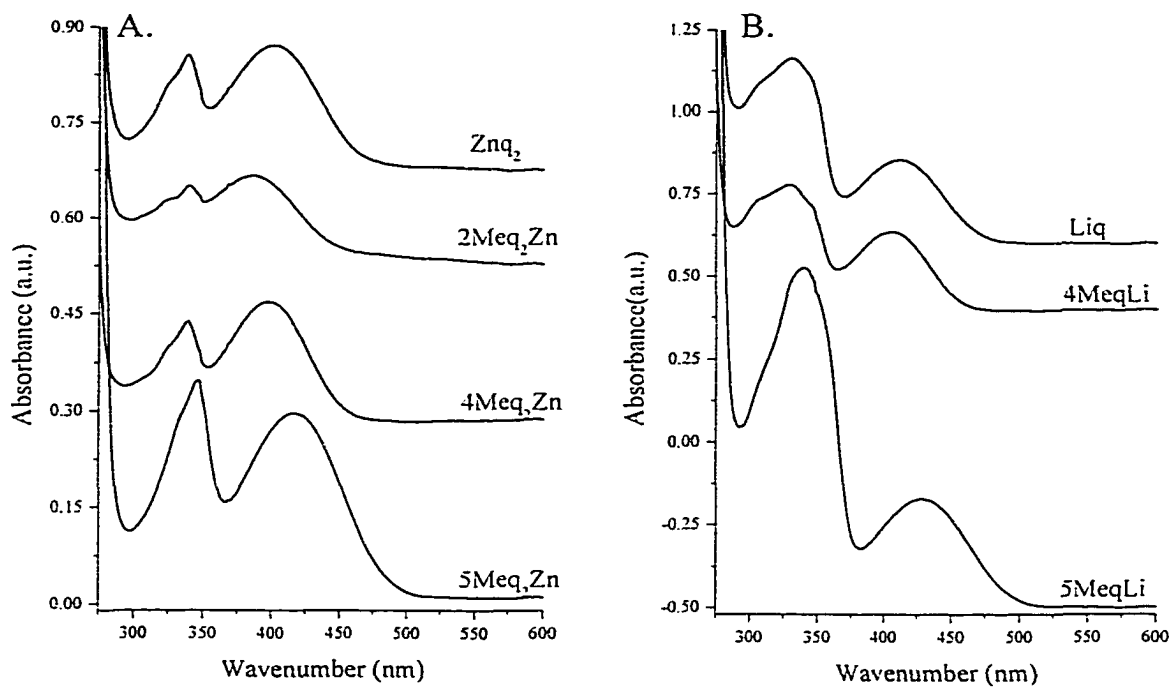


Figure 4.3. Absorption spectra of A. $n\text{Meq}_2\text{Zn}$ and B. $n\text{MeqLi}$ in DMF showing the effects of methylation of the ligand on the peak energies.

Table 4.3 Absorption λ_{max} and Energy Shifts from Mq_n .

Metal Chelate	Absorption CH_2Cl_2 λ_{max} (nm)	Absorption Energy Shift from Mq_n (cm^{-1})	Absorption DMF λ_{max} (nm)	Absorption Energy Shift from Mq_n (cm^{-1})
Znq_2	378		402	
$2\text{Meq}_2\text{Zn}$	385	-481	386	1031
$4\text{Meq}_2\text{Zn}$	371	499	399	187
$5\text{Meq}_2\text{Zn}$	393	-1010	419	-1009
Liq	361		412	
4MeqLi	357	310	406	359
5MeqLi	n.d.	n.d.	428	-907

n.d. = not determined

4.4 Photoluminescence Spectroscopic Results

4.4a Effect of Metal Ion Substitution: Solvent Dependencies of PL Properties

Tables 4.4 and 4.5 show the PL emission energies and relative ϕ_{PL} data for Alq₃, Znq₂ and Liq in CH₂Cl₂ and DMF, respectively. The full-width-at-half-maxima (FWHM) of PL emissions and the Franck-Condon (F-C) energy shifts (energy difference between absorption and emission) (Δ) are also included. Relative to Alq₃, in both solvents the λ_{max} (emission) was red shifted for Znq₂ (1681cm⁻¹/DMF and 1240 cm⁻¹/CH₂Cl₂) and blue shifted for Liq, (869 cm⁻¹/DMF and 2193 cm⁻¹/CH₂Cl₂). The FC-shifts increased in the order Znq₂ > Liq > Alq₃ and FWHM increased in the order Znq₂ > Alq₃ > Liq, suggesting that Znq₂ is the most vibrationally distorted in the excited state. Alq₃ exhibited essentially no change of F-C shifts in different solvents, whereas Znq₂ and Liq showed >1000 cm⁻¹ difference, with the larger shift observed in the less polar, and thus less interacting solvent.

In both solvents, ϕ_{PL} increased in the order Liq > Alq₃ > Znq₂. The reported quantum efficiencies of Alq₃ in DMF and CH₃Cl are 0.116⁽⁸⁾ and 0.02,⁽⁹⁾ respectively. Unlike Alq₃, both Znq₂ and Liq exhibited higher quantum efficiencies in the less polar solvent.

Table 4.4 Photophysical data of Mq_n in CH₂Cl₂.

Metal Chelate	Absorption CH ₂ Cl ₂ λ_{max} (nm)	Emission CH ₂ Cl ₂ λ_{max} (nm)	Emission Energy Shift from Alq ₃ (cm ⁻¹)	FWHM (nm)	Δ (cm ⁻¹)	Relative ϕ_{PL} Alq ₃ = 1.0
Alq ₃	388	514		102	6318	1.00
Znq ₂	378	549	-1240	111	8240	0.33
Liq	361	490	2193	92	7293	2.6

Table 4.5 Photophysical data of Mq_n in DMF.

Metal Chelate	Absorption DMF λ_{max} (nm)	Emission DMF λ_{max} (nm)	Emission Energy Shift from Mq_n (cm^{-1})	FWHM (nm)	Δ (cm^{-1})	Relative ϕ_{PL} $Alq_3 = 1.0$ ($Mq_n = 1.0$)
Alq_3	388	521		105	6623	1.0
Znq_2	402	571	-1681	110	7362	0.18
Liq	412	544	869	98	5889	1.1

4.4b Effect of Methylation of the 8-Quinolinolato Ligand on PL Properties

The photophysical data for the methylated derivatives of Znq_2 and Liq in CH_2Cl_2 and DMF are tabulated in Tables 4.6 and 4.7. Consistent with Mq_3 series, the effect of methyl-substitution on the PL emission energies was similar to those observed for absorption. However, where $5Meq_3Al$ and $4Meq_3Al$ exhibited the largest and smallest F-C shifts, respectively. However, for the methylated derivatives of Znq_2 and Liq the same result was not observed. Furthermore, all F-C shifts were significantly larger in the less interacting solvent, CH_2Cl_2 , with the exception of $2Meq_2Zn$.

Table 4.6 Photophysical Data of $nMeq_nM$ in CH_2Cl_2 .

Metal Chelate	Absorption CH_2Cl_2 λ_{max} (nm)	Emission CH_2Cl_2 λ_{max} (nm)	Emission Energy Shift from Mq_n (cm^{-1})	FWHM (nm)	Δ (cm^{-1})	Relative ϕ_{PL} $Alq_3 = 1.0$
Znq_2	378	549	0	111	8240	0.33
$2Meq_2Zn$	385	541	269	116	7490	0.42
$4Meq_2Zn$	371	530	653	102	8086	1.5
$5Meq_2Zn$	393	553	-132	134	7362	0.11
Liq	361	490	0	92	7293	2.6
$4MeqLi$	357	472	778	82	6825	4.9

Table 4.7 Photophysical Data of nMeq_nM in DMF.

Metal Chelate	Absorption DMF λ_{\max} (nm)	Emission DMF λ_{\max} (nm)	Emission Energy Shift from Mq _n (cm ⁻¹)	FWHM (nm)	Δ (cm ⁻¹)	Relative ϕ_{PL} Alq ₃ = 1.0
Znq ₂	402	571	0	110	7362	0.18
2Meq ₂ Zn	386	541	971	112	7422	0.5
4Meq ₂ Zn	399	546	802	103	6748	1.2
5Meq ₂ Zn	419	575	-122	169	6475	0.05
Liq	412	544	0	98	5889	1.1
4MeqLi	406	516	997	91	5251	3.3
5MeqLi	428	569	-808	106	5790	0.4

Figures 4.4 and 4.5 show the photoluminescence (PL) spectra obtained in DMF solution (see the Appendix III for PL spectra in CH₂Cl₂), where the relative intensities of the peaks correspond to the relative PL quantum efficiencies. Regardless of the metal ion substitution, upon methylation of the 8-quinolinolato ligand ϕ_{PL} increases in the order 4Meq_nM \gg Mq_n $>$ 5Meq_nM. Similar to 4Meq₂Zn, the 2Meq₂Zn derivative where substitution is on the pyridyl ring, also exhibited a substantially higher ϕ_{PL} compared to the C5-methylated and unsubstituted derivatives.

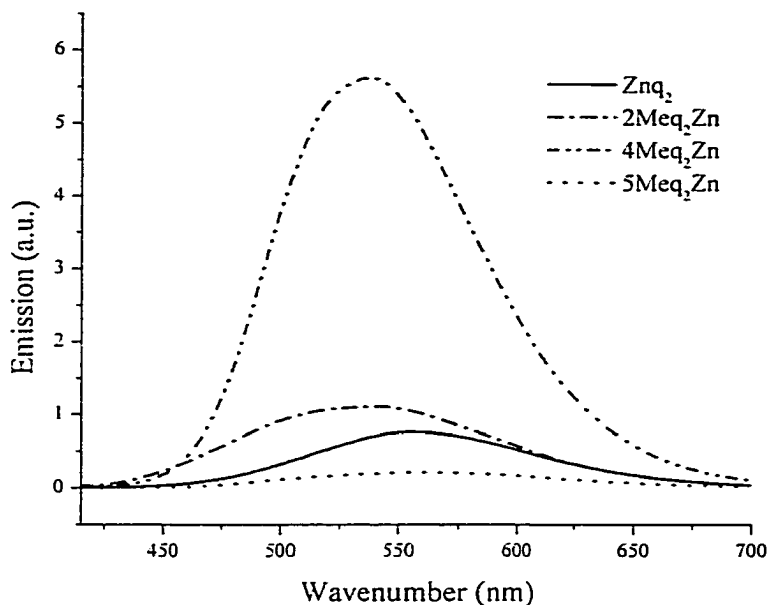


Figure 4.4. Emission Spectra of $n\text{Meq}_2\text{Zn}$ in DMF showing effects of methyl substitution on emission energies. The relative intensities are proportional to the relative intensities where there is a significant increase of ϕ_{PL} on $4\text{Meq}_2\text{Zn}$ and a decrease on $5\text{Meq}_2\text{Zn}$.

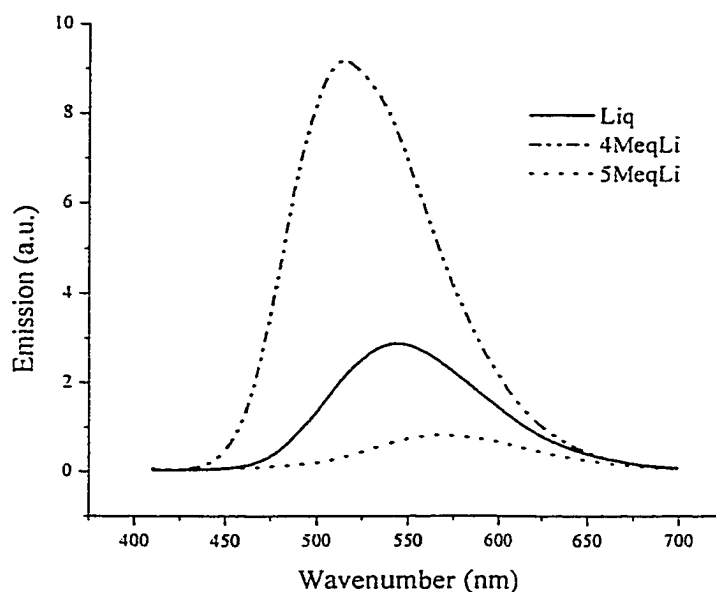


Figure 4.5. Emission spectra of $n\text{MeqLi}$ in DMF showing effects of methyl substitution on emission energies. The relative intensities are proportional to the relative intensities where there is a significant increase of ϕ_{PL} on 4MeqLi and a decrease on 5MeqLi .

4.5 Discussion and Conclusions

4.5a Effect of Metal Ion Substitution on Photophysical Properties

It is reasonable to conclude that in DMF, the red shift of the longest wavelength absorption energies for lithium mono(8-quinolinolato) chelates is caused by dissociation of the chelate by solvation or complexation with the polar solvent to form a ligand anion (q^-) / Li^+ metal cation pair. Three pieces of experimental evidence support this supposition: 1) the absorption spectrum of the deprotonated 8-quinolinol (q^-) in DMF, prepared by adding two drops of 10% NaOH to q dissolved in DMF was identical to the absorption spectrum of Liq (See Appendix III); 2) the chemical shifts of the aromatic protons in the 1H NMR spectra for Liq were more shielded in $DMSO-d_6$ vs. $CDCl_3$; and 3) the PL quantum efficiencies of $nMeqLi$ chelates in CH_2Cl_2 were larger than in DMF, because of the solvation of the anionic ligand results in a less rigid chelate structure.

On the other hand, the spectral changes in different solvents for Znq_2 are not so easily explained. The large blue shifts for Alq_3 and $2Meq_2Zn$ in the polar protic MeOH solvent most likely arise because of H-bonding between the quinolinolato oxygen with the solvent, thus stabilizing the ground state of these materials. The opposite effects observed for the other Znq_2 chelates suggest that the MeOH solvent interacts and Zn ion through its oxygen atom, rather than H-bonding, consistent with the formation of the dihydrated form of Znq_2 obtained when synthesized from aqueous solutions.

The $2Meq_2Zn$ chelate did not show the same effects in MeOH and DMF as the other $nMeq_2Zn$ because of the position of methyl substitution. Although the exact geometry (tetrahedral vs. square planar) of the $nMeq_2Zn$ chelates is not established, it is expected that the $2Meq_2Zn$ material would be the least likely to exist in a square planar

structure because of steric hindrance of methyl substitution at the C2-position and it has the least solvent interaction among all the $n\text{Meq}_2\text{Znq}_2$ chelates. In fact, because of the steric hindrance by the methyl group on the 2C- position, the quinolinolato oxygens would be more likely to interact with MeOH through H-bonding because the methyl groups would block the Zn ion. This suggests that the geometry of the ligands for the other $n\text{Meq}_2\text{Zn}$ chelates may be more planar. Therefore, in both polar solvents (DMF and MeOH) the excited state is more stabilized than the ground state. The red shifts of absorption in DMF are larger than in MeOH because DMF interacts by complexation (or solvation) of the ligand vs. the metal ion, and thus has a stronger effect on the energy of absorption than MeOH since the metal ion is not directly involved in the electronic transition.

These results suggest that for $n\text{Meq}_2\text{Zn}$ chelates, with the exception of $2\text{Meq}_2\text{Zn}$, there must be a larger difference in polarity between the ground and excited states compared to the metal tris-chelates. This would be true if indeed the electronic distribution on the ligand is more evenly distributed over both the pyridyl ring and phenoxide ring of the ligand in the ground state. This could be because of a more ionic character in the metal ligand bonding, as indicated by the NEXAFS data presented in Chapter 3, and thus the excited state would be more polar. However, additional experiments are necessary to confirm this supposition.

The effects of ligand methylation on the photophysical properties of the metal (8-quinolinolato) chelates were similar regardless of the metal ion. For all materials C4-methylation substantially increased the PL quantum efficiencies. For the $n\text{Meq}_3\text{M}$ chelates C4-methylation resulted in a doubling of ϕ_{PL} vs. the unsubstituted analogue,

Alq₃. An even larger increase of ϕ PL was observed for 4Meq₂Zn vs. Znq₂ (4.5 fold increase) and the increase for C-4 methylation for Liq was ~2 fold. The increase in ϕ PL for 4Meq₃Al vs. Alq₃ was attributed to decreased coupling of the metal-ligand stretching coordinates to the electronic transition responsible for PL. Since the infrared spectra of all metal (8-quinolinolato) chelates are similar (see Chapter 2) this decreased coupling of the vibrational modes to the electronic transition may be a common property for all C4-methylated derivatives.

References

1. Curioni, A.; Boero, M.; Andreoni, W.; *Chem. Phys. Lett.* **1998**, *294*, 263.
2. Chen, C.H. and Shi, J. *Coord. Chem. Rev.* **1998**, *171*, 161.
3. Padmaperuma. A. MS.in Chemistry, University of Nevada, Las Vegas, 2000.
4. Sapochak, L.S.; Padmaperuma, A.; Washton, N.; Endrino, F.;Schmett, G.; Marshall, J. and Fogarty, D. Effects of Systematic Methyl-Substitution of Metal (III) Tris(n-Methyl-8-Quinolinolato) Chelates on Material Properties for Optimum Electroluminescence Device Performance. *J. Am. Chem Soc.* in press. **2001**.
5. Burrows, P.E.; Sapochak, L.S.; McCarty, D.M.; Forrest, S.R and Thompson, M.E. *Appl. Phys. Lett.* **1994**, *64(20)*, 2718.
6. Kushto, G.P.; Iizumi, Y.; Kido, J.; and Kafafi, Z.H. *J. Phys. Chem.* 2000, *104*, 3670.
7. Shulman, S. and Rietta, M. Formation of Coordinate Covalent Complex between Lithium and 8-Quinolinol. *J. Pharm. Sci.* **1971**, *60*, 11, 1762.
8. Lytle, F.E.; Storey, D. R. and Juricch, M.E. Systematic atomic number effects in complexes exhibiting ligand luminescence. *Spectrochimica Acta.* **1973**. 29A,1357-1369.

CHAPTER 5

DEVICE FABRICATION AND ELECTROLUMINESCENCE CHARACTERIZATION

5.1 Device Fabrication

Dr. Paul Burrows at Pacific Northwest National Laboratories fabricated and tested the devices. All OLED's were fabricated simultaneously as depicted in Figure 5.1. Devices were grown on glass slides precoated with indium tin oxide (ITO) with a sheet resistance of $15\Omega/\text{cm}^2$. The ITO substrates were degreased in detergent, then boiled in 1,1,1-trichloroethane, rinsed with reagent grade acetone and finally rinsed with methanol before being dried in stream of UHP nitrogen. The substrates were then exposed to UV-Ozone for 5 minutes. A 500 Å layer of the preferentially hole transporting material (HTL), N,N'-diphenyl-N,N'-bis(1-naphthol) 1,1'-biphenyl-4,4'diamine (α -NPD) (See Figure 5.2), was deposited on the ITO substrate by thermal evaporation from a baffled Mo crucible at a nominal rate of 2-to-4 Å/s under a base pressure of $<2 \times 10^{-6}$ Torr. A 550 Å layer of the preferentially electron-transporting (ETL) zinc bis (n-methyl-8-quinolinolato) chelates, also serving as the emitter layer (EML), was then deposited on the HTL. A top electrode consisting of a 5 Å LiF layer deposited on the EML layer followed by a 1000 Å layer of Al metal was subsequently deposited by thermal evaporation through a mask as circular 1 mm diameter contacts. In order to have

minimal variation on the thickness of each layer, all devices were made at the same time, where the HTL was vapor deposited on all the devices, as well as the cathode layers. Thus, devices produced from different metal chelate materials were identical in all respects. An Alq₃ based OLED was also fabricated and tested simultaneously with the Znq₂ materials and used as the reference material in this study. A quartz crystal oscillator placed near the substrate was used to measure the thickness of the films. Film thicknesses were calibrated by ellipsometry of films grown on silicon.

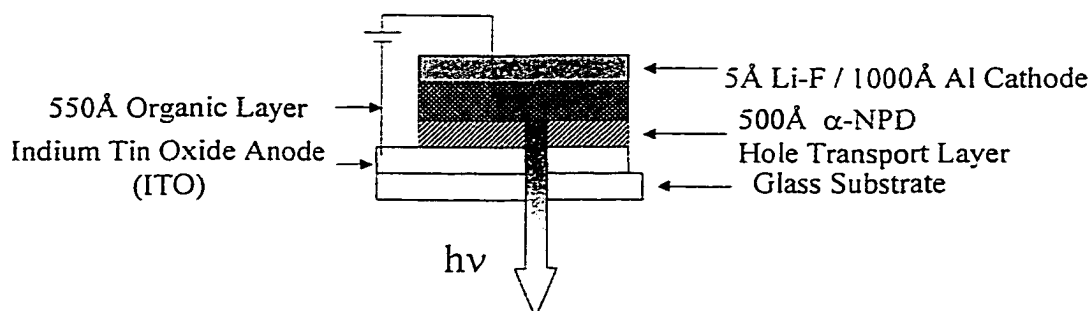


Figure 5.1. Schematic representation of an organic-light emitting device.

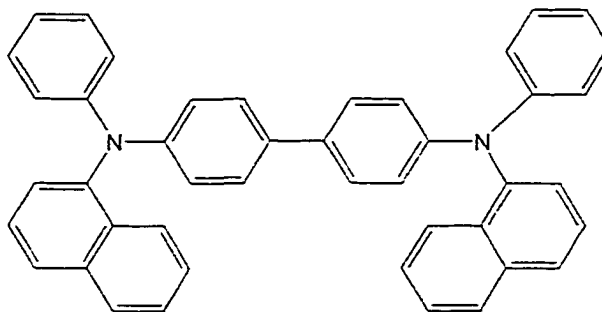


Figure 5.2. α-NPD.

5.2. Device Testing

Devices were tested in air with an electrical pressure contacts made by means of a 25 μm diameter Au wires. Current-voltage characteristics were measured with a Hewlett-Packard HP4145 semiconductor parameter analyzer, and EL intensities were measured with a Newport 835 optical power meter with a large area photodetector placed directly below the glass substrate. Thus, all efficiencies reported were measured directly from the backs of the devices with no corrections or assumptions regarding angular dependence of the electroluminescence. Spectra were recorded with an EG&G optical multichannel analyzer on a 0.25 focal length spectrograph.

5.3 Calculation of Relative Electroluminescence Efficiencies (Rel. η_{EL})

Electroluminescent quantum efficiencies (η_{EL} = photons emitted/electron injected) were calculated relative to devices prepared with Alq₃ as the EML with normalized $\eta_{\text{EL}}(\text{Alq}_3) = 1.0$. The applied voltage was increased gradually while measuring the light output and the current across the device. Data were collected from the pixilated device and average was acquired from at least three pixels on each device. Electroluminescence efficiencies were calculated from the optical output power (L) at a low current drive of 100 μA (current density of 13 mA/cm^2) using equation (1).

$$\text{Rel. } \eta_{\text{EL}} = \eta_{\text{EL}}(\text{ref})L_{\text{sample}}/L_{\text{ref}} \quad (1)$$

5.4 Electroluminescence Results

The electroluminescence energy shifts of the methylated Znq₂ materials were consistent with those observed for PL emission energies, where methylation of the

pyridyl ring (C2 or C4-methylation) resulted in a blue shift of emission and substitution of the phenoxide ring (C5-methylation) resulted in a red shift. The spectral data and colors of OLED light emission are shown in Table 5.1. Note that the 4Meq₂Zn material saturated the spectrograph detector; therefore, the reported λ_{\max} value is approximated.

Table 5.1 EL Spectral Data.

Metal Chelate	λ_{\max} (nm) of EL Emission	Color
Alq ₃	530	Green
Znq ₂	571	Yellow-green
2Meq ₂ Zn	560	Yellow-green
4Meq ₂ Zn	549*	green
5Meq ₂ Zn	578	Yellow-orange

*Estimated value from saturated spectrum.

The current versus voltage (IV) characteristics of OLED's composed of ITO/NPD/metal chelate/LiF-Al are shown in Figure 5.3. The device operating voltages (at a fixed current) increases in the order 4Meq₂Zn << Znq₂ ≤ Alq₃ < 5Meq₂Zn << 2Meq₂Zn. Although the voltage data were highly variable (largest variation was for 5Meq₂Zn), the relative differences in the voltage requirements between the metal chelate materials used as the EML in identically prepared OLED's were significant. (See the Appendix)

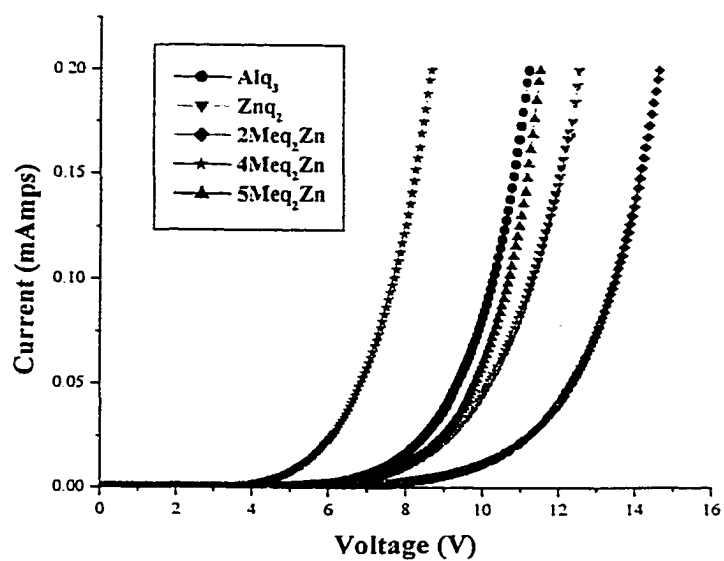
Figure 5.4 shows the dependence of the optical output power on drive current for each OLED. At a current of 100μA, the EL output increases in the order 5Meq₂Zn << 2Meq₂Zn < Znq₂ < Alq₃ << 4Meq₂Zn with less variability in the data compared to the I/V characteristics (see the Appendix).

The EL device data are tabulated in Table 5.2. The C4-methylated derivative of Znq_2 exhibited the highest relative EL quantum efficiency ($\sim 2X$ greater than the Alq_3 reference material) and the C5-methylated derivative the lowest. These results are consistent with the results for the metal tris(8-quinolinolato) series where the EL efficiencies were directly related to the PL efficiencies of the materials. However, $4\text{Meq}_2\text{Zn}$ also exhibited the lowest voltage requirement in the series. Previously, we showed that $4\text{Meq}_3\text{Al}$ had a higher EL efficiency than the unsubstituted derivative, Alq_3 , but with a higher voltage requirement. (See Figures 5.4 and 5.5)⁽²⁾

As discussed in Chapter 1, if PL efficiency is the dominating factor for high EL efficiency then the ratio, $\eta_{\text{EL}} / \phi_{\text{PL}}$ should be close to 1.0. As shown in Table 5.2, this ratio is greater than 1.0 for all Znq_2 materials investigated. This suggests that the other material properties, namely charge injection and transport efficiencies, must be different in these materials. This is not surprising because of the expected differences in geometry of the Znq_2 materials compared to the octahedral metal tris-chelates, which will have a large impact on solid-state packing. However, what is surprising is the significantly lower voltage requirement and higher light output exhibited by $4\text{Meq}_2\text{Zn}$. Explanations for these differences are discussed in the preceding section of this thesis; results are correlated to the differences in photophysical, thermal and electronic structure properties of these materials.

Table 5.2 EL Device Data.

Metal Chelate	Voltage (at $13\mu\text{m/s/cm}^2$)	Rel. η_{EL} ($\text{Alq}_3 = 1.0$)	$\eta_{\text{EL}}/\phi_{\text{PL}}$ ($\text{Alq}_3 = 1.0$)
Alq_3	7.5 ± 0.1	1.0	1.0
Znq_2	7.3 ± 0.4	0.73	2.2
$2\text{Meq}_2\text{Zn}$	10.1 ± 0.3	0.60	1.4
$4\text{Meq}_2\text{Zn}$	5.3 ± 0.1	1.9	1.3
$5\text{Meq}_2\text{Zn}$	7.6 ± 0.6	0.23	2.1

**Figure 5.3. Current vs. voltage (IV) curve for nMeq₂Zn and Alq₃ as reference.**

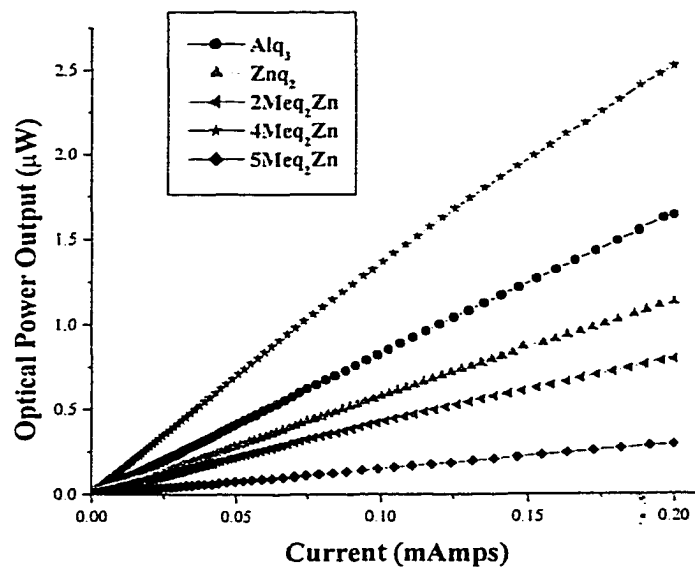


Figure 5.4. Light output vs. current for $n\text{Meq}_2\text{Zn}$ and Alq_3 as reference.

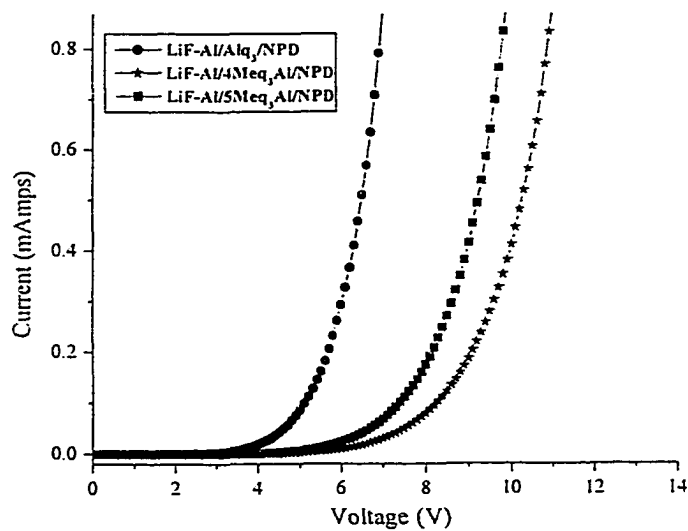


Figure 5.5. Current vs. voltage (IV) curve for $n\text{Meq}_3\text{Al}$.

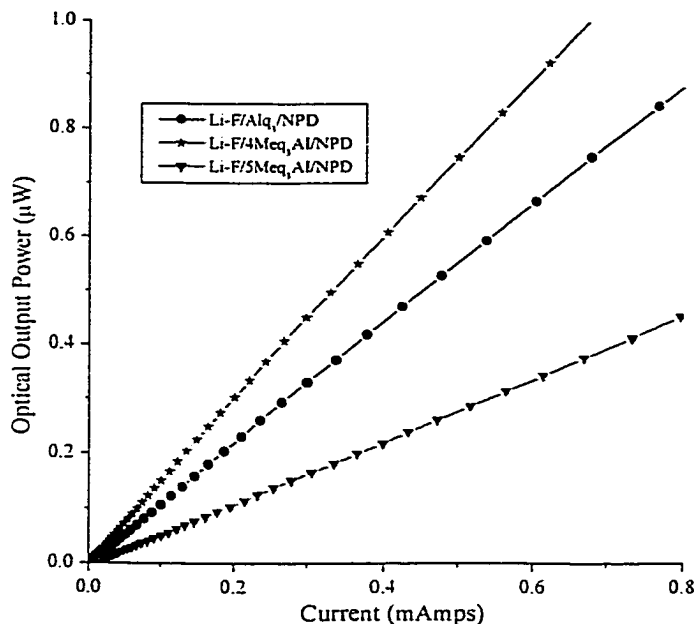


Figure 5.6. Light output vs. current for nMeq₃Al.

5.5 Discussions and Conclusion

Improving the electroluminescence efficiency of emitter materials requires better understanding of how the photoluminescence efficiency, the energy level alignment with the cathode and the hole transport layer and charge transport are affected by the molecular structure, electronic structure and bulk packing in the solid state. One way to establish structure/function relationships is through systematic studies of similar materials.

Alq₃ is the most studied emitter material for organic electroluminescence applications because it has the best balance of material properties leading to efficient and stable device performance. The high PL efficiency in the solid state (30 %)⁽⁴⁾ and high glass transition temperature (177°C)⁽⁵⁾ has been attributed to its nearly octahedral

structure. Unlike most organic materials used for EL, Alq₃ is a fairly good electron transporting material, which is due to the preferential overlap in the solid state of the electron deficient pyridyl rings, the likely site of electron injection and transport. Indeed, we have previously shown that methylation of the pyridyl ring of Alq₃ caused an increase in drive voltage in OLED devices.⁽⁶⁾ Therefore, significant changes in the coordination geometry of the ligands and changes in the electronic distribution on the pyridyl ring should have significant effects on charge transport properties of metal (8-quinolinolato) chelates. The purpose of this thesis was to investigate these effects through systematic study of tetracoordinated zinc (n-methyl-8-quinolinolato) and bicoordinated lithium (n-methyl-8-quinolinolato) chelates.

The thermal characterization showed that for all metal (n-methyl-8-quinolinolato) chelates, the C4-methylated derivatives had the lowest melting points, with the exception of the Liq chelates. The trend of the melting points for Liq chelates is similar to the T_m of the ligands. Low melting points for the 4Meq_nM are indicative of weaker cohesive forces in the solid states compared to their unsubstituted analogue. Also, 4Meq₂Zn, 4Meq₃Al and 5Meq₃Al had the highest glass transition temperatures with no other transitions observed above T_g unlike their unsubstituted analogues, which exhibited recrystallization before melting. This high stability of the glassy state is favorable for practical OLED applications. For the nMeqLi chelates no other thermal transitions were observed other than T_m , and therefore these materials were the most “salt-like” of all Mq_n.

The most intriguing result from the thermal characterization was that the glass transition temperatures were not significantly different between the zinc bis- and

aluminum tris- chelate series. Naito suggested that the high T_g of Alq_3 was because of its spherical shape. Therefore, if the glass transition were dependent on the shape of the molecule, we would expect a different trend for the more planar Znq_2 materials. However, all $nMeq_2Zn$ chelates exhibited almost exactly the same T_g as the corresponding $nMeq_3Al$ series, indicating that the nature of the ligand moiety has a stronger effect on the T_g than the metal chelate geometry.

Although the effects of methylation of the ligand on the photophysical properties and the electronic structure were similar for all metal (8-quinolinolato) chelates, substitution of the metal ion caused significant differences in the solvent dependencies of absorption and intensities of the carbon edge NEXAFS spectra. The inclusion of the Liq materials in these studies was important for understanding the nature of the differences between the Alq_3 and Znq_2 materials. The solvent dependences of absorption and emission energies were partially accounted to the geometry changes of the metal chelate, resulting in stronger interactions with solvent molecules. We also propose that, because of the differences in the ionic nature of the metal-ligand bond, a large red shift of the longest wavelength of absorption was observed in a more polar solvent. Indeed, the NEXAFS spectroscopy of the carbon K-edge of Mq_n supports an increasing ionic metal-ligand bonding character from $Alq_3 < Znq_2 < Liq$. The significant decrease of the intensity of the lowest energy transition (LUMO (I)) upon metal ion substitution is indicative of decrease of the probability of the LUMO (I) transition, which can occur if those LUMO states are more “filled.” One way to interpret this trend is that a more even electron distribution between the pyridyl ring and the phenoxide ring supports a more ionic character of the metal ligand bond of Liq than Znq_2 than Alq_3 .

In order to draw implications about the electroluminescence performances of the metal quinolate chelates, it is important to know the packing behavior of these materials. Unfortunately, the geometry of the ligands for Znq_2 has not been established because of the inability to obtain single crystals for x-ray diffraction analysis. However, molecular modeling suggests that the material has an intermediate geometry between a tetrahedral and square planar.⁽⁹⁾ However, crystal structures of the dihydrate form of Znq_2 and the anhydrous form of copper (8-quinolinolato) have been determined,^(10,11) where the geometries of the ligands were essentially planar. In the case of the dihydrate Znq_2 , the interaction of the water molecules in the axial position on the zinc atoms provided a strong influence on the planarity of the 8-quinolinolato ligand geometry, which may be significantly different in the anhydrous form. However, we propose that the $2Meq_2Zn$ chelate exhibits the least planar geometry than all other $nMeq_2Zn$ chelates studied. $2Meq_2Zn$ exhibited similar solvent dependences of the absorption and emission energies as the metal tris-(8-quinolinolato) chelates, which suggests that there are less solvent interaction for this material than the other $nMeq_2Zn$. This is also consistent with the steric hindrance induced by C2-methylation of the pyridyl ring of the ligand. Therefore, with a more planar structure for Znq_2 , $4Meq_2Zn$ and $5Meq_2Zn$, these materials can have close π - π stacking interaction. In fact, in the crystal structure reported for Cuq_2 , the π - π stacking interaction of the ligands was ~ 3.3 Å, which is less than the π - π stacking interaction in Alq_3 ⁽⁷⁾ (~ 3.5 Å).

Although the results from the photophysical and electronic characterization of Liq were important piece of the puzzle, time allowed us to carry out the device characterizations only for Znq_2 chelates. For the Znq_2 materials, a reduction of the

number of ligands coordinated to the metal ion should allow more room for better ligand overlap in the solid state. As a result there may be both positive and negative implications on electroluminescence performance. For example closer π - π stacking interactions can lead to excimer and/or exciplex formation in the solid state, which is known to quench efficient light generation⁽³⁾, but this close interaction may enhance charge transport properties. For all metal chelates studied in this thesis, there was no evidence for excimer or exciplex formation neither from the photophysical studies of solid-state films nor from the electroluminescence spectra from OLEDs.

On the other hand, substitution of Zn atom, which will have more ionic metal-ligand bonding character, should reduce the number of electron trapping sites. For all metal (8-quinolinolato) chelates, it is believed that electrons are injected and transported through the electron deficient, pyridyl ring of the ligand. However, no discussions of electron trapping differences among these materials have been reported. There are two ways we believe that electrons can become trapped in the metal (8-quinolinolato) materials. The crystal structure for Alq_3 ⁽⁷⁾ showed that two of the three ligands were closely interacting ($<3.5\text{\AA}$), where the third ligand was less interacting ($>3.5\text{\AA}$) with adjacent molecules. If an electron is transported into the third ligand, it can act as an electron trap and may result in an increase in drive voltage. This form of electron trap is less likely for the Znq_2 chelates because all ligands may closely interact with an adjacent ligand. Another possible mechanism for electron trapping may be due to the relative electron affinity of the pyridyl ring acceptor of the ligand. For both the zinc and lithium chelates studied in this thesis, x-ray spectroscopic studies suggest that the electrons were more evenly distributed between the two ring systems of the ligand, which would

decrease the electron affinity of the pyridyl ring. If so, the electron can be more easily transported to the adjacent ligand, enhancing electron transport because of shallower traps.

Previously, we have showed that, for the aluminum metal tris-quinolates, 4Meq₃Al has the highest light output and the 5Meq₃Al has the lowest light output, relative to Alq₃, which is consistent with the trends in their ϕ_{PL} . However, although 4Meq₃Al have the highest light output, it requires a much larger drive voltage than Alq₃. We proposed that the larger drive voltage upon methyl substitution on the 4-C position is a consequence of impedance matching by preferential overlap of the pyridyl rings. Therefore, charge transport may be less favorable. For the Znq₂ chelates, similar to Alq₃, 4meq₂Zn gave the highest light output and 5Meq₂Zn exhibited the lowest light output, consistent with the trends in their ϕ_{PL} . However, unlike Alq₃, in addition for its high light output, 4Meq₂Zn (~5.3 V) also required the least drive voltage requirement compared to Znq₂ and Alq₃. The drive voltages of Znq₂ (~7.3 V) and 5Meq₂Zn (~7.6 V) were similar to Alq₃ (~7.5 V), while 2Meq₂Zn (~10.1 V) had the highest. If photoluminescence is the dominating factor for the EL performance of all metal (8-quinolinolato) chelates and electron injection/transport and charge injection are similar for all metal (8-quinolinolato), then we would expect a similar trends in EL efficiencies, where $\eta_{\text{EL}}/\phi_{\text{PL}}$ should be close to 1.00. However, $\eta_{\text{EL}}/\phi_{\text{PL}}$ for 4Meq₃Al and 5Meq₃Al are 0.40 and 1.3, respectively. We propose that the charge transport and/or injection of metal quinolinolato chelates are enhanced with ratios >1.00 and less favorable with ratios < 1.00. The $\eta_{\text{EL}}/\phi_{\text{PL}}$ ratios for all Znq₂ were all > 1.00. Therefore, electron injection and/or transport are enhanced in the Znq₂ materials. Indeed, if the anhydrous form of Znq₂ is

more planar than tetrahedral, closer π - π stacking interaction should lead to better electron transport properties compared to Alq₃. This explains the similarities of the drive voltage requirements of Alq₃ with Znq₂ and 5Meq₂Znq. For 2Meq₂Zn, the larger drive voltage requirement was accounted to the less planar geometry, which may prevent efficient overlap of the ligand moieties in the solid state and hinders charge transport. 4Meq₂Zn exhibits a substantially lower voltage requirement than all other nMeq₂Zn chelates studied. Our rationalization to this result is that this material may have reduced trapping ability of the injected electrons, because of the placement of the methyl group on the pyridyl ring causing a decrease in electron affinity.

References

1. Padmaperuma, A. Substitution effects of metal quinolate chelate materials for organic electroluminescence applications. M.S. in Chemistry, University of Nevada, Las Vegas, **2000**.
2. Sapochak, L.S.; Padmaperuma, A.; Washton, N.; Endrino, F.; Schmett, G.; Marshall, J. and Fogarty, D. Effects of Systematic Methyl-Substitution of Metal (III) Tris(n-Methyl-8-Quinolinolato) Chelates on Material Properties for Optimum Electroluminescence Device Performance. *J. Am. Chem Soc.* in press. **2001**.
3. Burrows, P.E.; Sapochak, L.S.; McCarty, D.M.; Forrest, S.R and Thompson, M.E. Metal ion dependent luminescence effects in metal tris-quinolate organic heterojunction light emitting devices. *Appl. Phys. Lett.* **1994**, 64(20), 2718-2720.
4. Chen C.H and Shi, J. Metal chelates as emitting materials for organic electroluminescence. *Coor. Chem Rev.* **1998**, 171, 161-174.
5. Sapochak, L.S.; Padmaperuma, A.; Washton, N.; Endrino, F.;Schmett, G.; Marshall, J. and Fogarty, D. Effects of systematic methyl-substitution of metal

- (III) tris(n-methyl-8-quinolinolato) chelates on material properties for optimum electroluminescence device performance. *J. Am. Chem. Soc.* in press. **2001**.
6. Burrows, P.E.; Shen, Z.; Bulovic, V.; McCarty, D.M.; Forrest, S.R.; Cronin, J.A.; and Thompson, M.E. Relationship between electroluminescence and current transport in organic heterojunction light-emitting devices. *J. of Appl. Phys.* **1996**, *79*, 7991-8006.
 7. Brinkmann, M.; Gadret, G.; Muccini, M.; Taliani, C.; Masciocchi, N.; and Sironi, A. *J. Am. Chem. Soc.* **2000**, *122*, 5147.
 8. a) Hamada, Y.; Sano, T.; Fujita, N.; Fujii, T.; Nishio, Y.; and Shibata, K. Organic electroluminescent devices with 8-hydroxyquinoline derivative-metal complexes as an emitter. *Jpn. J. Appl. Phys.* **1993**, *32*, L514-L515. b) Hamada, Y.; Sano, M.; Fujita, T.; Nishio, Y.; and Shibata, K. *Jap. J. Appl. Phys.* **1993**, *32(4A)*, L514.
 9. Nicolau, D.V. and Yoshikawa, S. Molecular modelling of Me^{2+} (8-hydroxyquinolate)₂ complexes using ZINDO and ESSF methods. *J. Mol. Graph. and Mod.* **1998**, *16*, 83.
 10. Merritt, L.L. Jr.; Cady, R. and Mundy, B. The crystal Structure of zinc 8-hydroxyquinolate dihydrate. *Acta. Cryst.* **1954**, *7*, 473.
 11. Petit, S. and Coquerel, G. Mechanism of Several Solid-solid transformations between dihydrated and anhydrous copper(II) 8-hydroxyquinolates. Proposition for a unified model for the dehydration of molecular crystals. *Chem. Mater.* **1996**, *8*, 2247-2258.

CHAPTER 6

CONCLUSIONS

The work presented here represents only a small piece of a much larger puzzle. The long-range goal is to have more detailed understanding of the structure function relationships in organic materials derived from metal quinolate chelates and how we can optimize the metal quinolate materials. In order to achieve this goal, much more work is necessary concerning the characterization of metal quinolate chelates in general. Specifically, with regard to the present study concerning Znq_2 and Liq, many questions remain unanswered. Solutions to these questions may be found through further investigations and the following discussion outlines the future direction of this research.

To begin, more structural characterization must be performed on the Znq_2 materials such as variable temperature NMR or solid state NMR. This would provide more information regarding the structure. In addition, packing behavior and coordination geometry of Znq_2 needs to be determined in order to truly establish a structure/function relationship. This information could also be substantiated with x-ray powder diffraction data.

To strengthen our interpretation from the electronic characterization and photophysical properties that a more ionic metal ligand bonding character exists in Liq compared to Znq_2 and much less so in Alq_3 , several experiments must be performed.

First, the comparison of the solution FT-IR and solid FT-IR of Liq, Znq₂ and Alq₃ will provide insights into the differences and similarities between the C=O and C-O⁻ stretches, which may provide some indication about whether there is partial dissociation of the Liq. Also, if indeed Liq has the most ionic metal ligand bonding character and there is some delocalization of the phenolic oxygen lone pairs towards the quinolate ligand, we would observe a significant C=O stretch for Liq materials. Another experiment that may be performed is color titration of the Mq_n. This experiment would provide information about the relative ionic character of these materials provided that an appropriate solvent is found for the Znq₂ materials. Results from this experiment will also allow us to compare the relative ease to which these materials dissociate in solution.

Although the overall results from this thesis work suggests that Znq₂ might be a better electron transporter material than Alq₃, more experiments with similar materials must be carried out in order to understand the properties that can affect charge transport and electron transport. For example, because the voltage requirements will be dependent on both charge injection and charge transport, charge mobility studies should be performed to determine which modification (methyl vs. metal ion substitution) would have a larger effect. In addition, more x-ray spectroscopic studies must be carried out to determine the HOMO/LUMO energies, in comparison to theoretical treatment of the metal quinolate chelates. Once the HOMO/LUMO energies are found, this information can then be correlated to the electron injection and hole injection phenomena. It will also provide a guide for determining which hole transporters and cathodes would be more appropriate and would have a better energy level matching with the electron transporter/emissive materials. Theoretical treatment and molecular modeling of the

metal quinolate chelates would also aid in the understanding of the transitions observed in the NEXAFS spectroscopy. Once this information becomes available, this may help in determining the transitions responsible for photoluminescence and/or electroluminescence. From there, we can determine the cause of the relative shifts and changes in intensities from the UV-Vis spectroscopy.

In the NEXAFS spectroscopy carried out for in this thesis, the reasons for the differences and similarities in the C and N peak energies and relative intensities are not well established. Since our interpretation may be one of many ways of interpreting the data, further investigations along these lines are recommended. One potential would involve comparing the O 1s NEXAFS of Mq_n . Results from this experiment would give some chemical information about the environment of the O, which may provide additional information about the nature of the metal ligand bond in these materials.

All in all, the important finding for this thesis is that, although the metal ion is not directly involved in the photoluminescence process of the metal quinolate chelates, directly it can affect the electroluminescence through a modified coordination geometry and electron distribution on the quinolate ligand, thereby affecting electron transport, electron injection and hole injection properties. However, only through systematic studies of similar materials would we derive the structure/function relationship of these materials.

APPENDIX I

FT-IR DATA

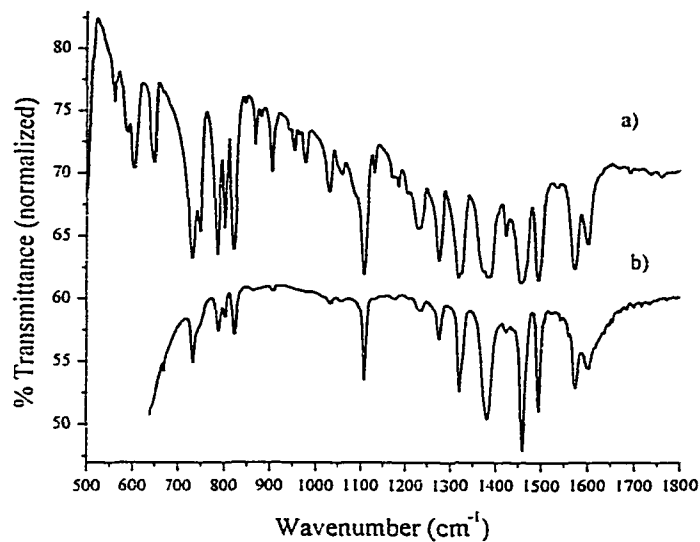


Figure A-1 FT-IR Spectra of Znq₂: a) KBr Pellet; b) Vapor Deposited Film.

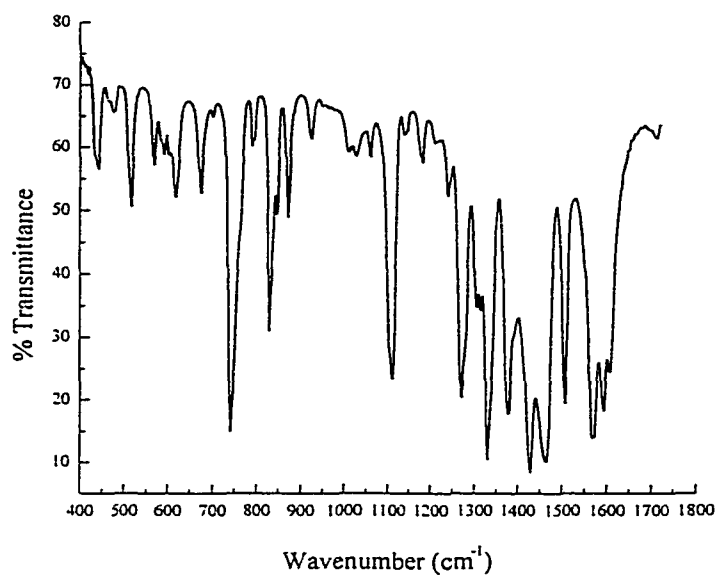


Figure A-2 FT-IR Spectra of 2Meq₂Zn on KBr Pellet.

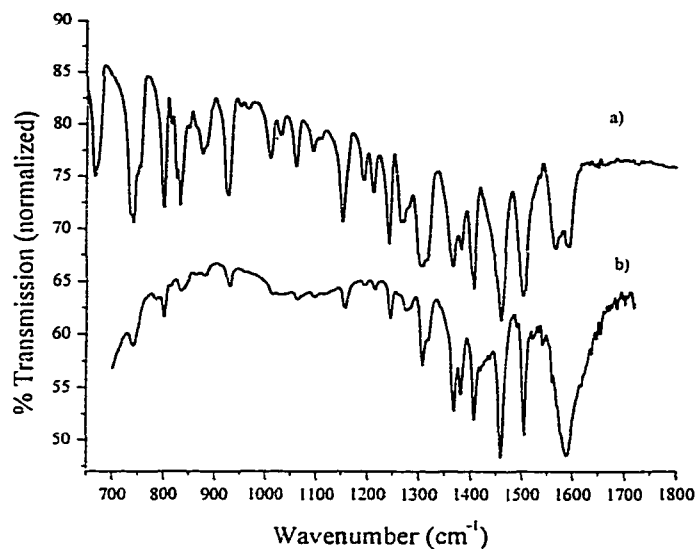


Figure A-3 FT-IR Spectra of 4Meq₂Zn: a) KBr Pellet; b) Vapor Deposited Film.

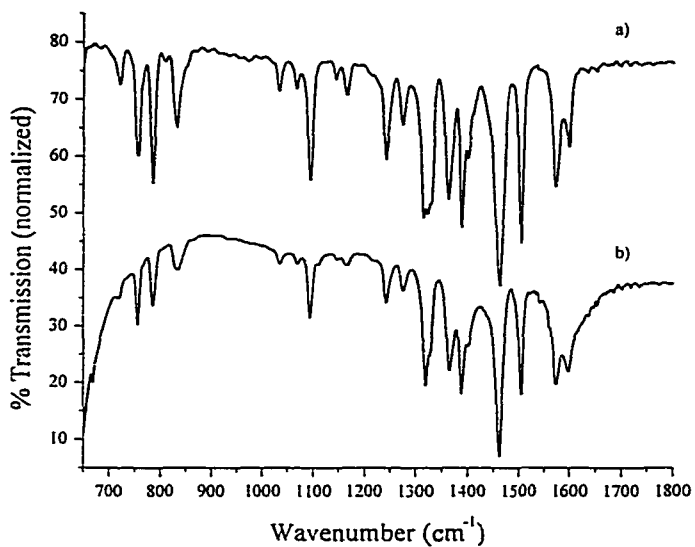


Figure A-4 FT-IR Spectra of 5Meq₂Zn: a) KBr Pellet; b) Vapor Deposited Film.

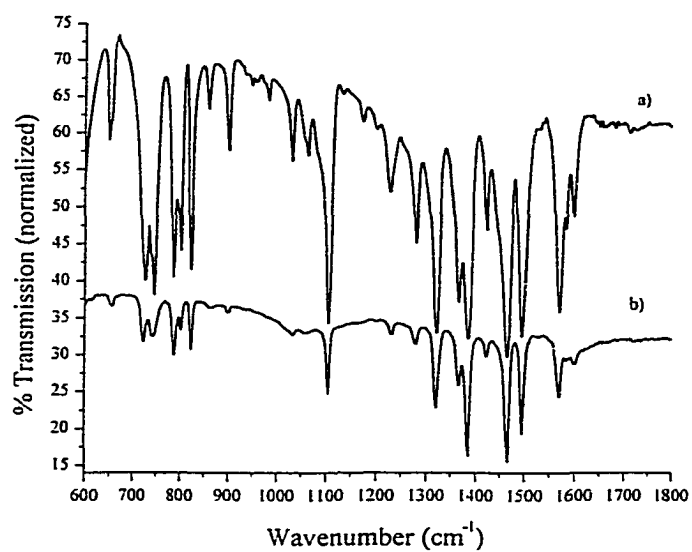


Figure A-5 FT-IR Spectra of Liq: a) KBr Pellet; b) Vapor Deposited Film.

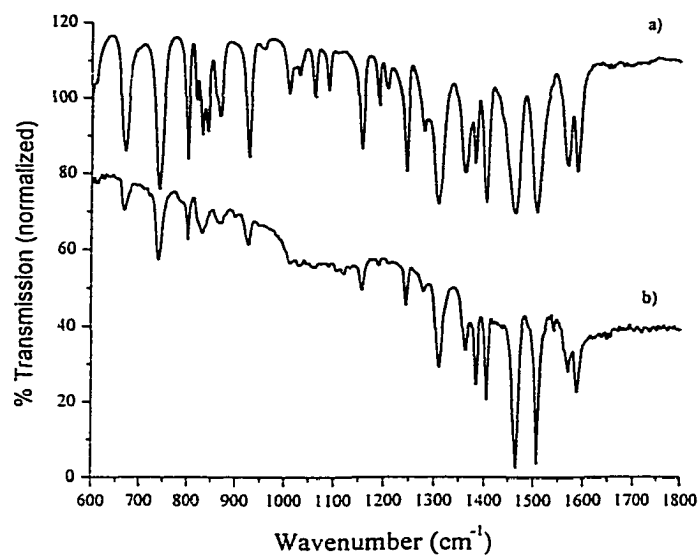


Figure A-6 FT-IR Spectra of 4MeqLi: a) KBr Pellet; b) Vapor Deposited Film.

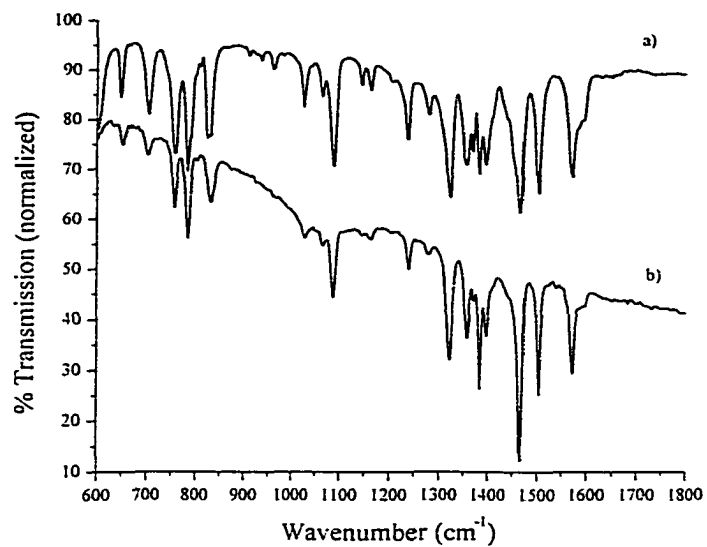


Figure A-7 FT-IR Spectra of 5MeqLi: a) KBr Pellet; b) Vapor Deposited Film.

APPENDIX II

THERMAL PROPERTIES DATA

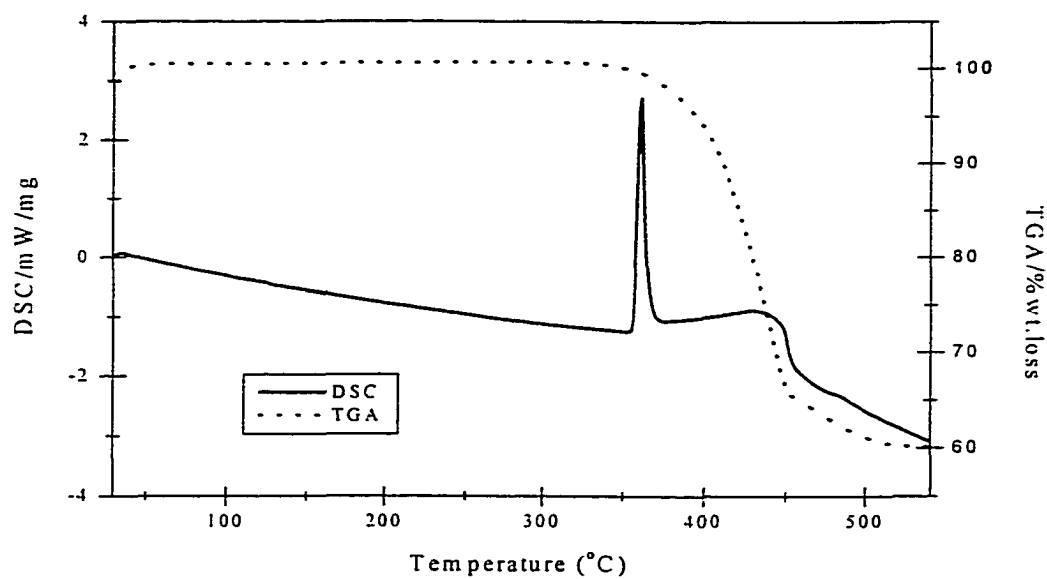


Figure B-1 Decomposition temperature for Znq_2 .

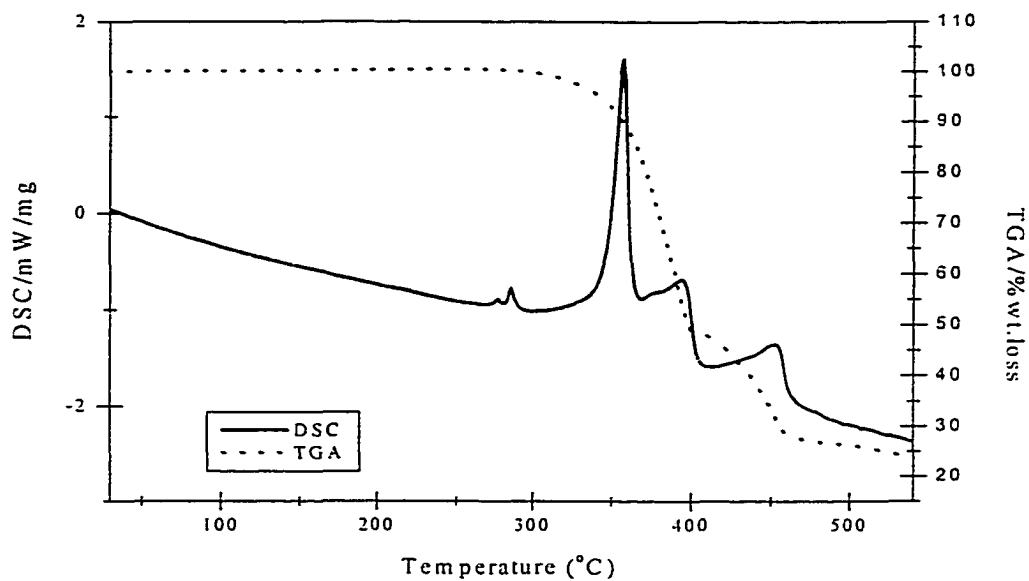


Figure B-2 Decomposition temperature for $2Meq_2Zn$.

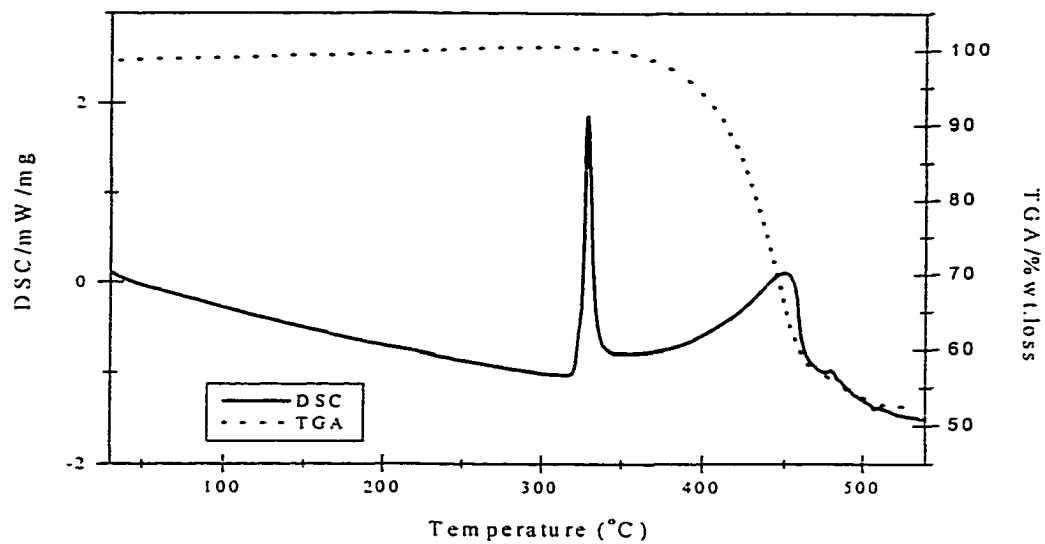


Figure B-3 Decomposition temperature for 4Meq₂Zn.

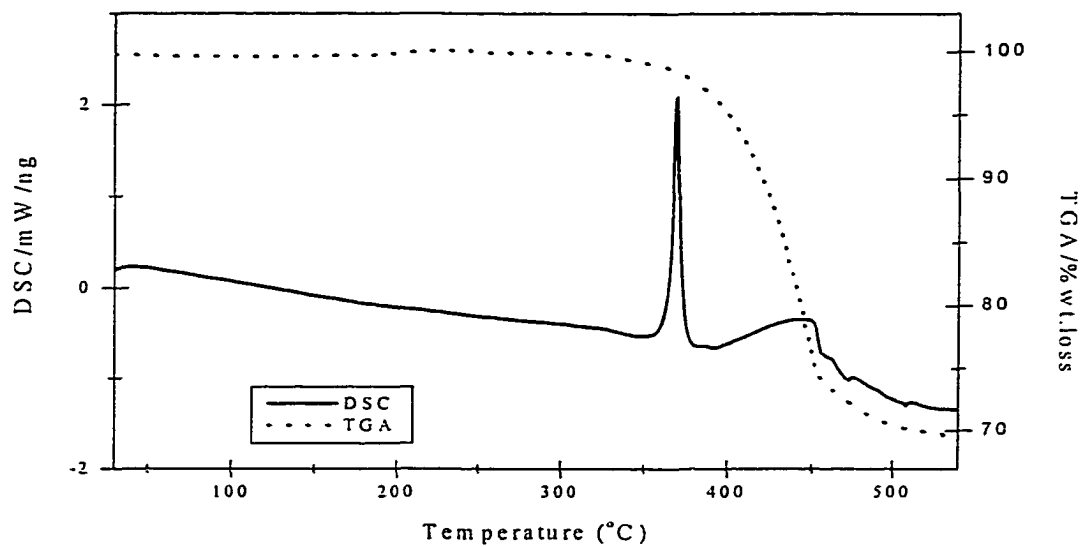


Figure B-4 Decomposition temperature of 5Meq₂Zn.

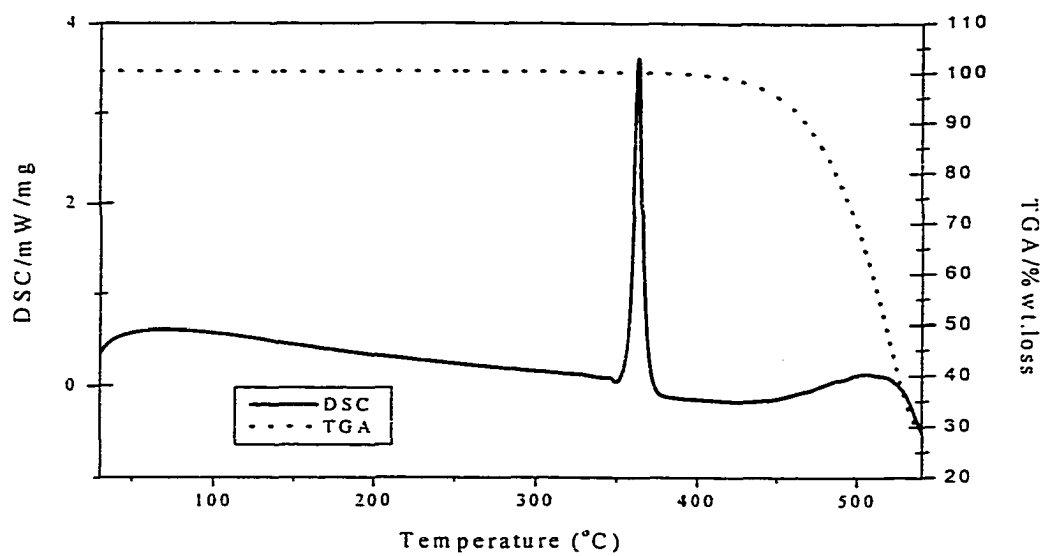


Figure B-5 Decomposition temperature of Liq.

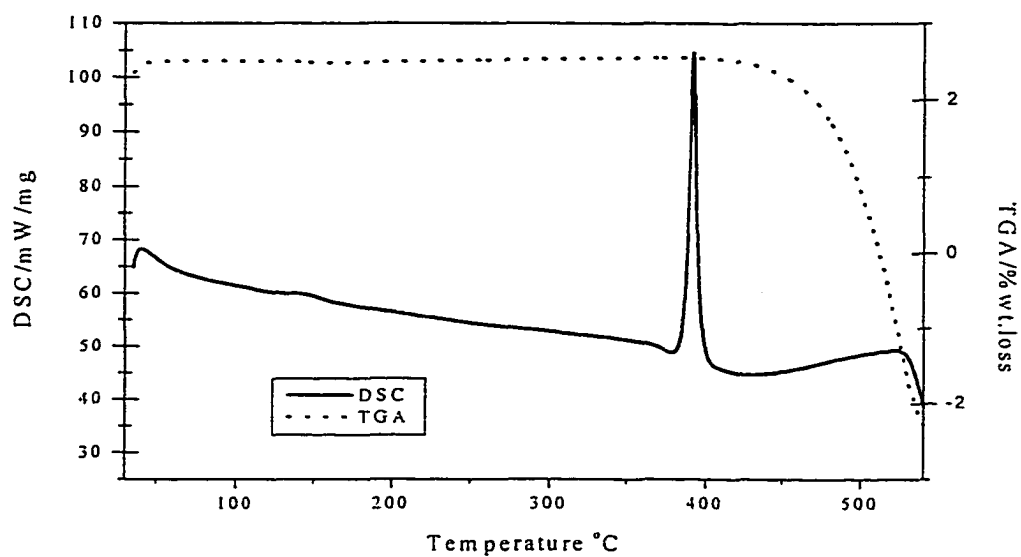


Figure B-6 Decomposition temperature of 4MeqLi.

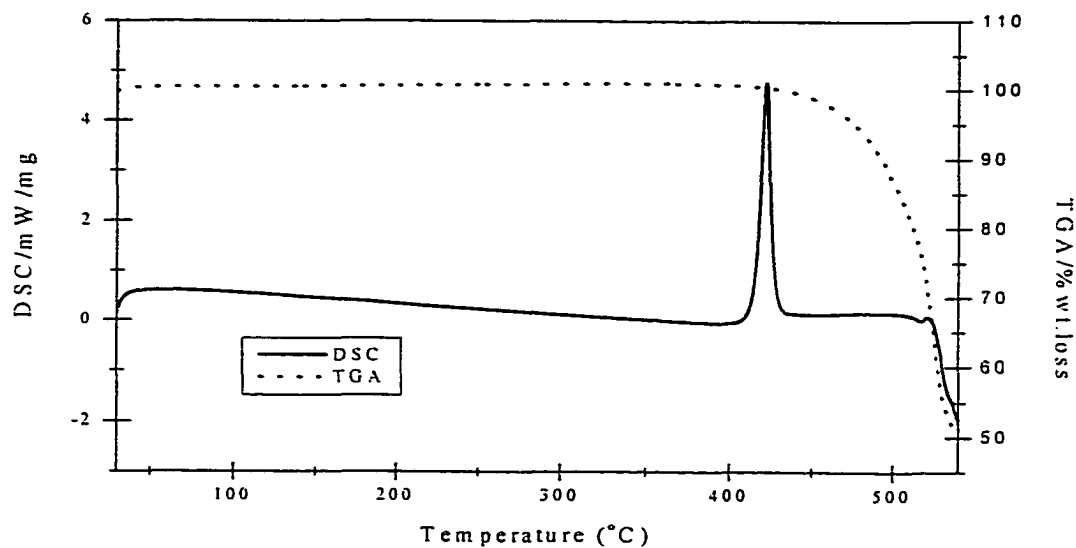


Figure B-7 Decomposition temperature of 5MeqLi.

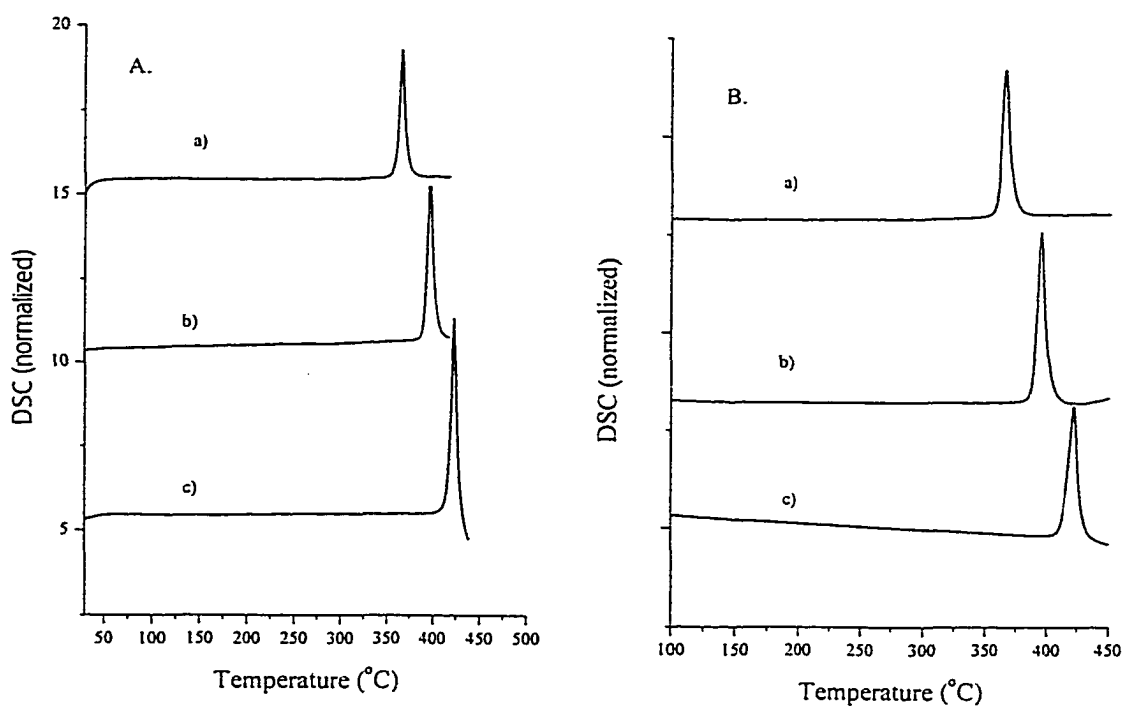


Figure B-8 DSC traces of A) first and B) second heating cycles of lithium mono-quinolinolato chelates: (a) Liq; (b) 4MeqLi and (c) 5MeqLi.

APPENDIX III

PHOTOPHYSICAL DATA

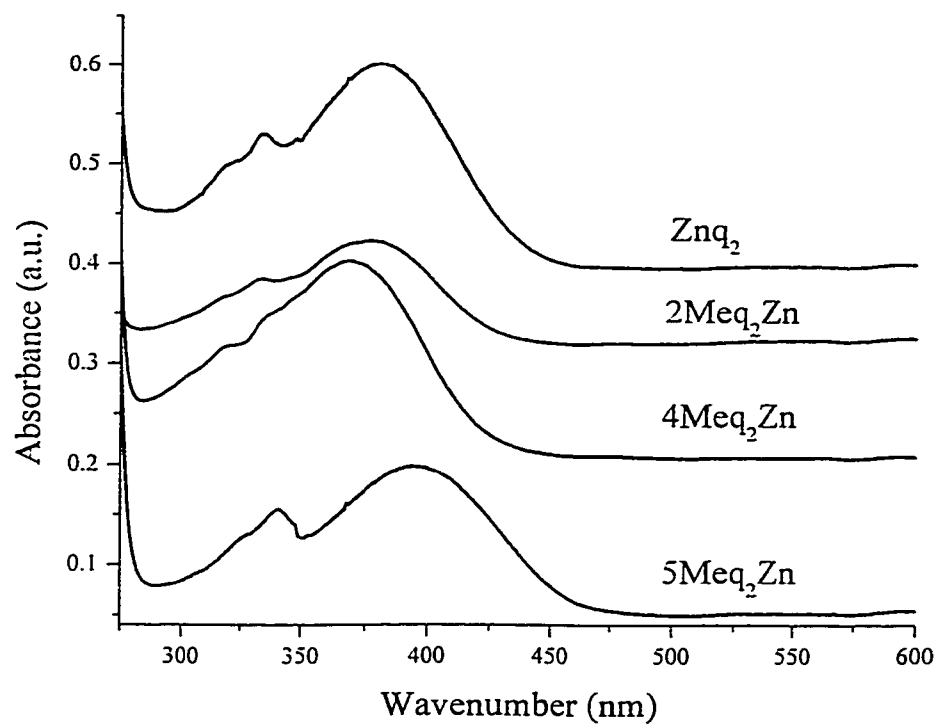


Figure C-1 Absorbance Spectra of nMeq₂Zn in MeOH.

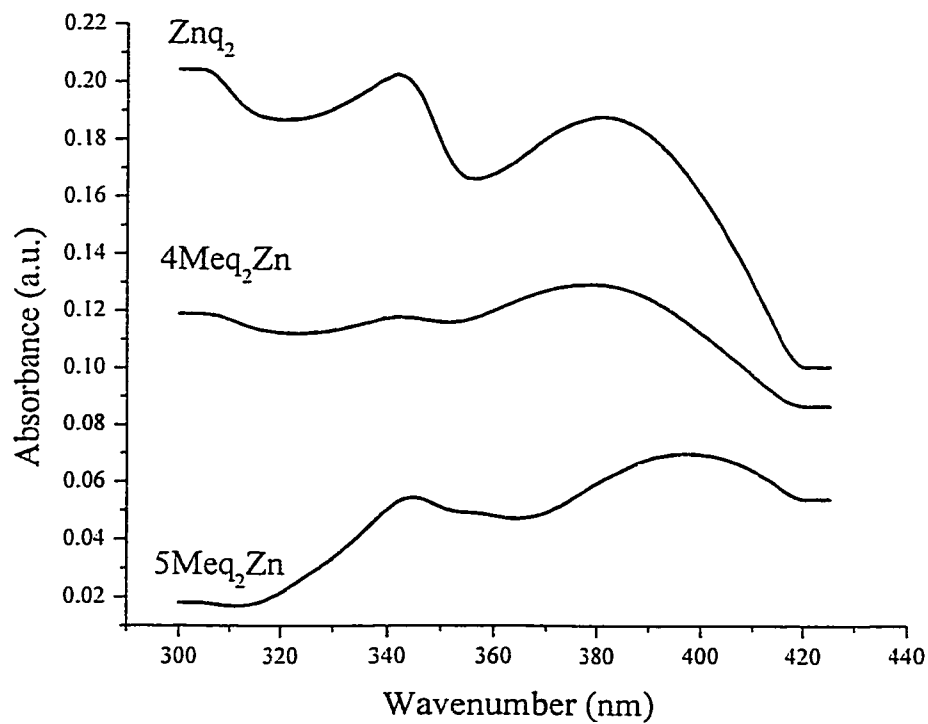


Figure C-2 Absorbance Spectra of nMeq₂Zn on Film.

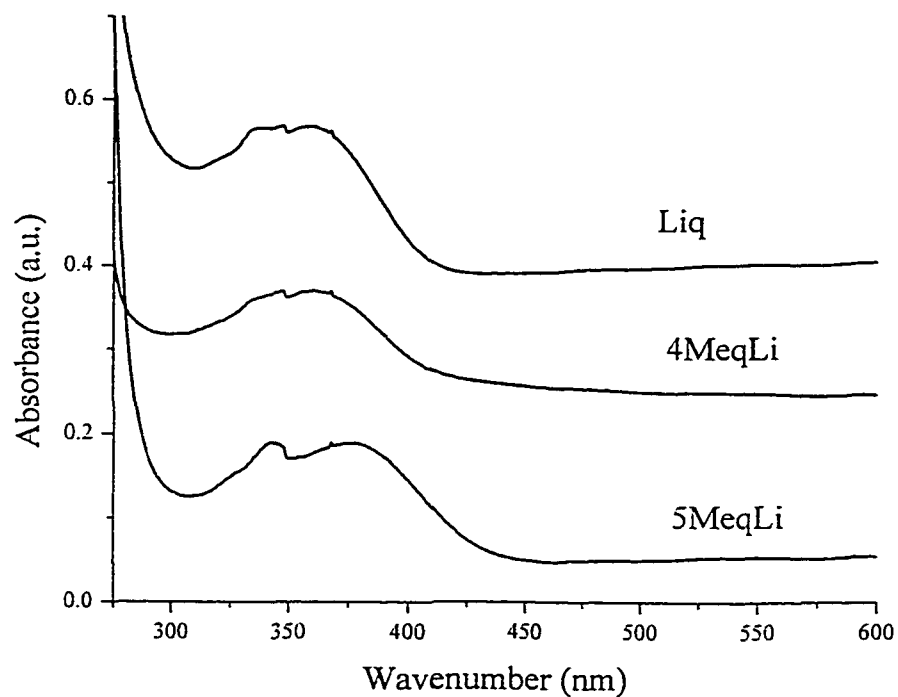


Figure C-3 Absorbance Spectra of nMeqLi on Film.

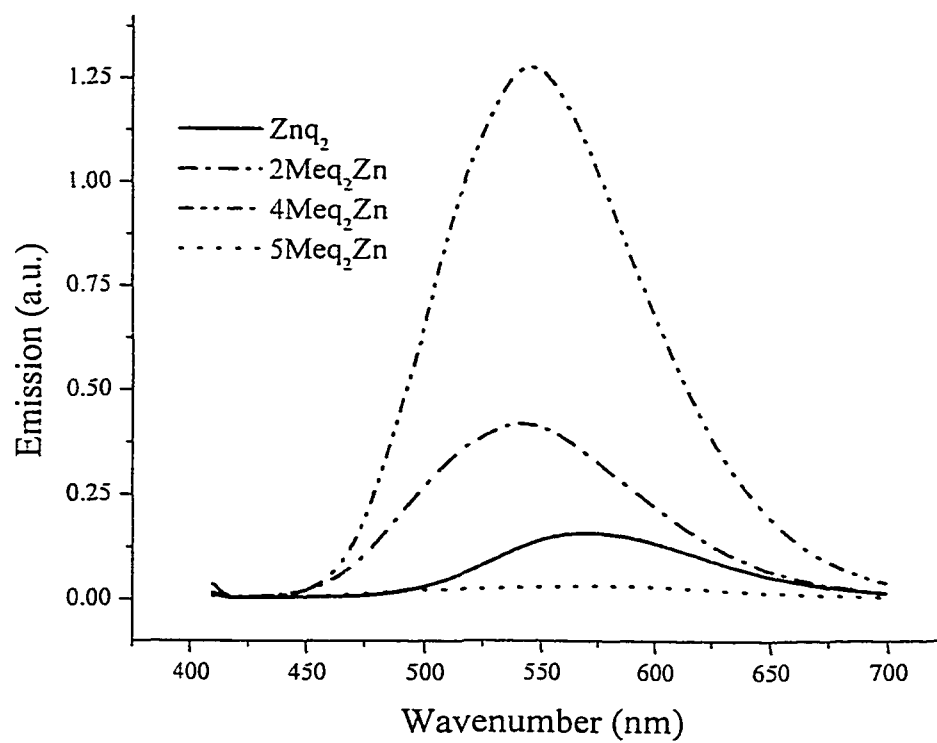


Figure C-4 Emission Spectra of nMeq₂Zn in CH₂Cl₂.

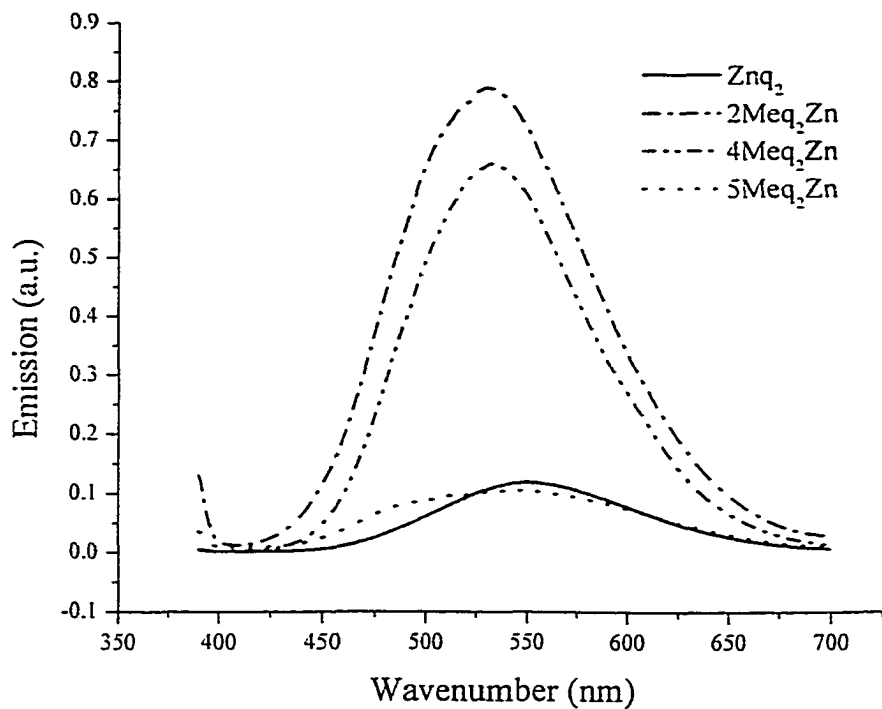


Figure C-5 Emission Spectra of $n\text{Meq}_2\text{Zn}$ in MeOH.

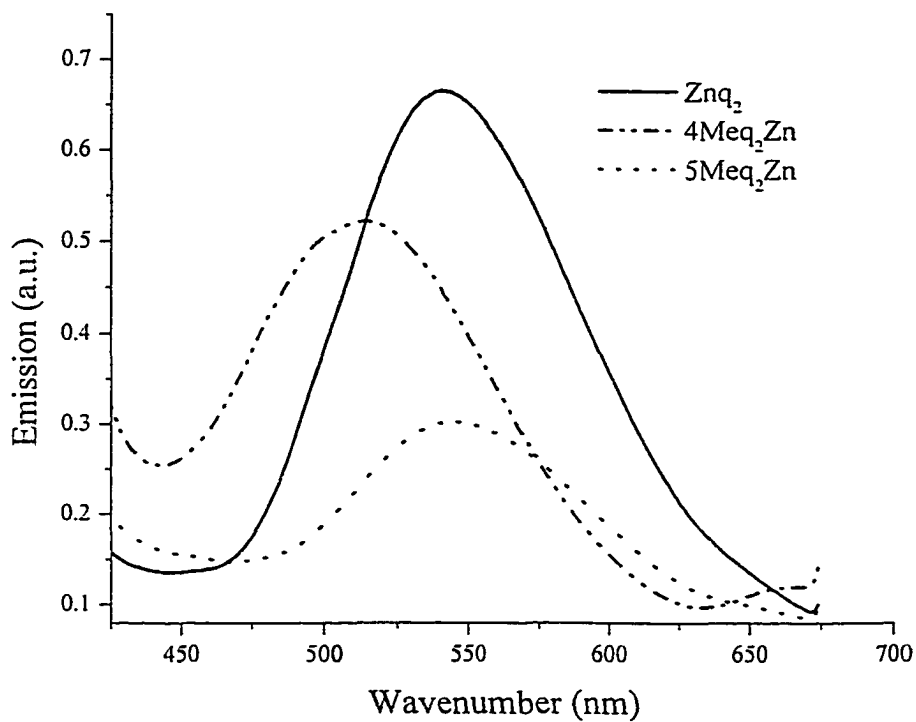


Figure C-6 Emission Spectra of $n\text{Meq}_2\text{Zn}$ on Film.

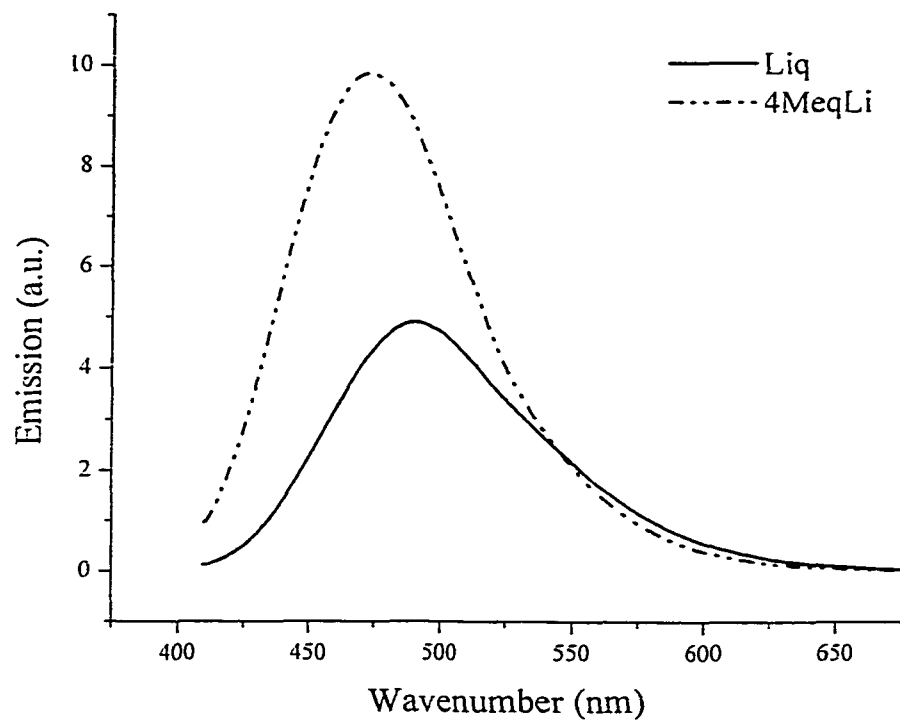


Figure C-7 Emission Spectra of nMeqLi in CH₂Cl₂.

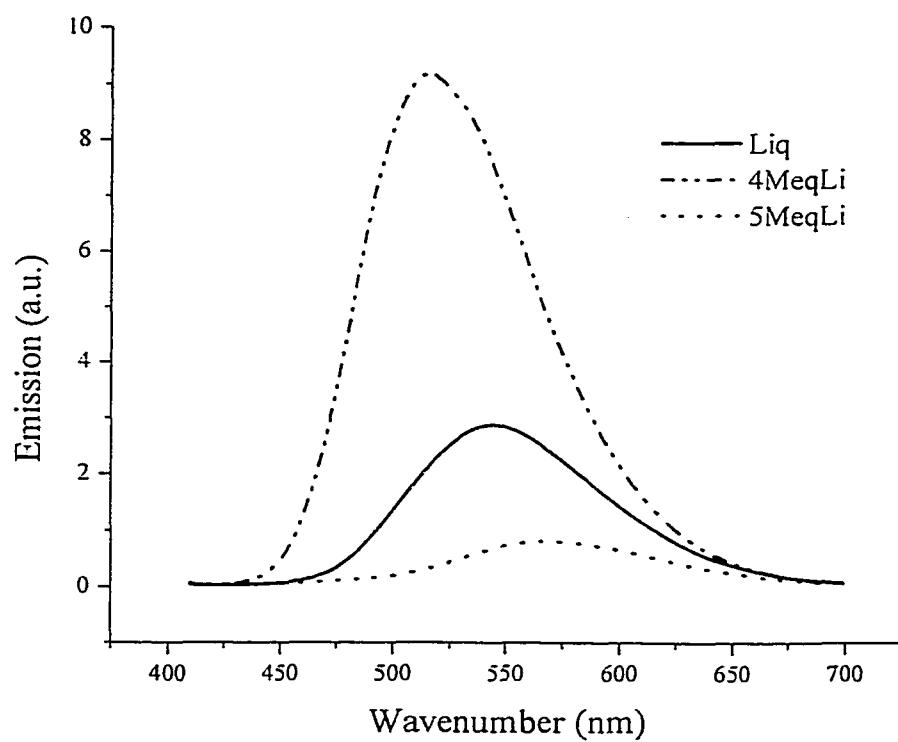


Figure C-8 Emission Spectra of nMeqLi in DMF.

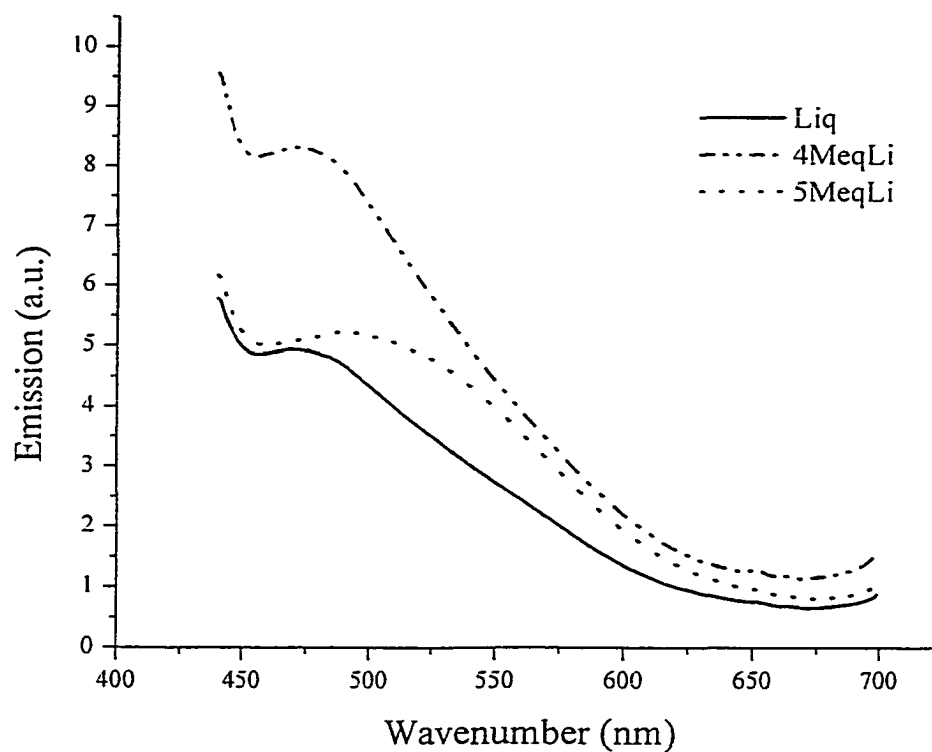


Figure C-9 Emission Spectra of nMeqLi on Film.

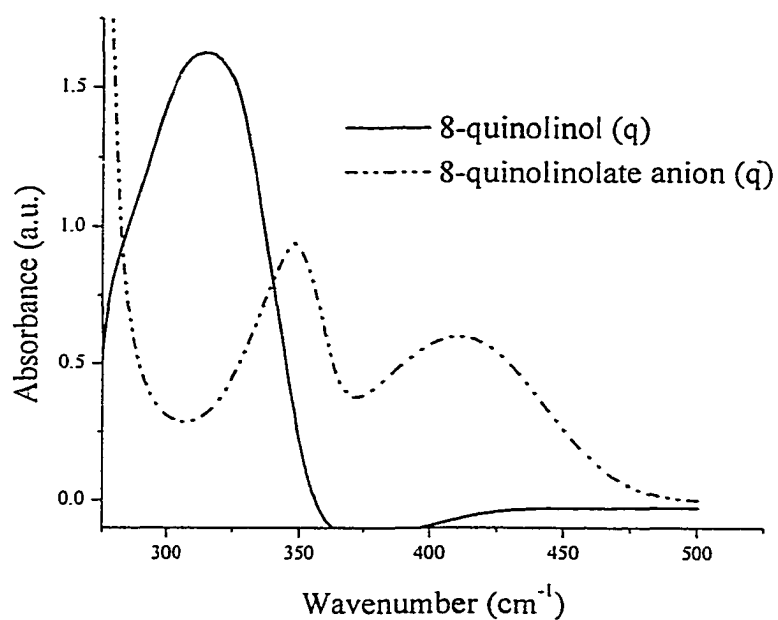


Figure C-10 Absorption Spectra of q and q⁻ in DMF.

APPENDIX IV

DEVICE PROPERTIES

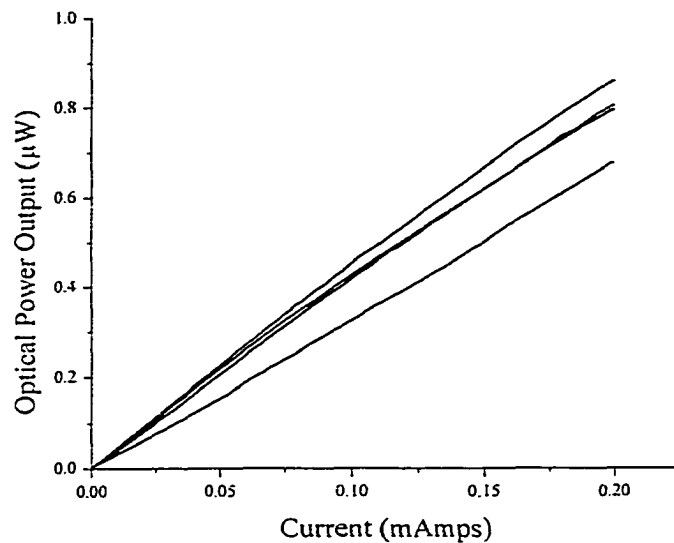


Figure D-1 IV curves for Znq₂.

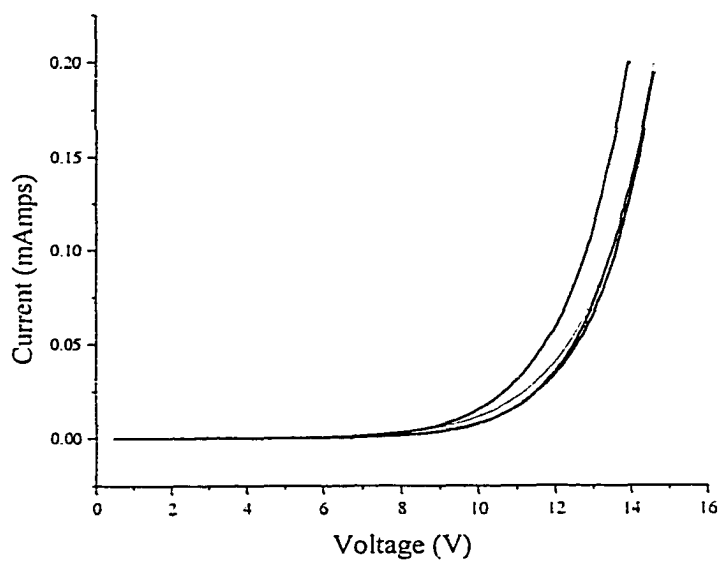


Figure D-2 IV curves for 2Meq₂Zn.

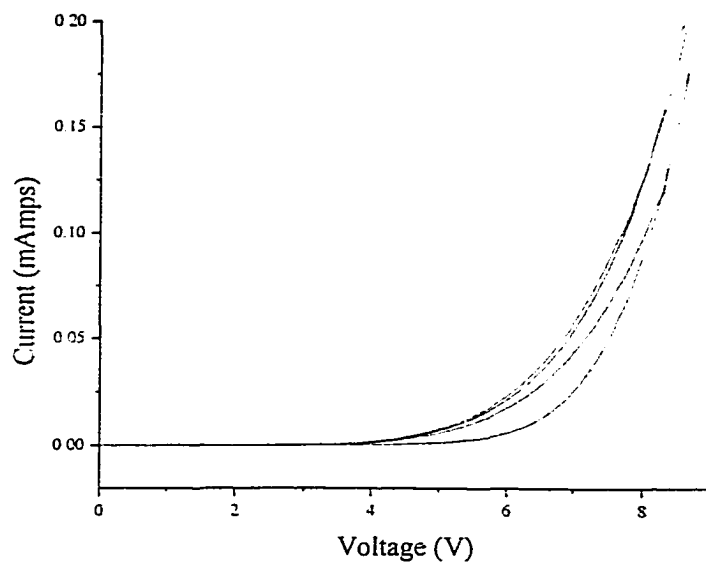


Figure D-3 IV curves for 4Meq₂Zn.

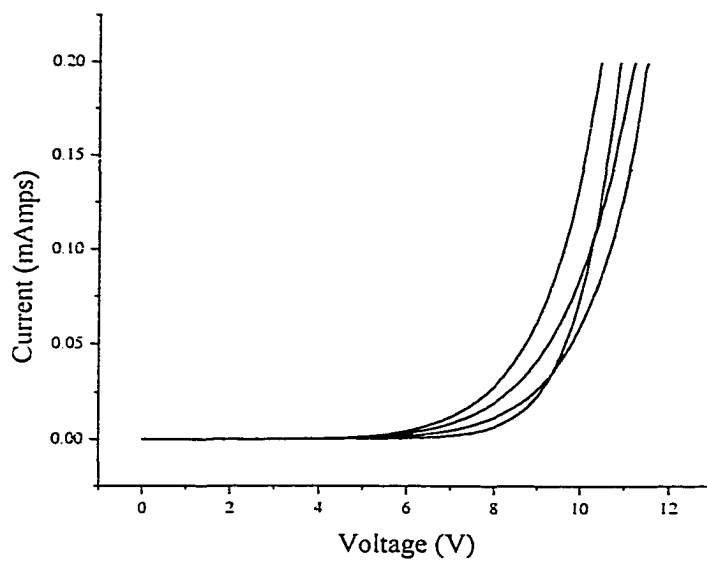


Figure D-4 IV curves for 5Meq₂Zn.

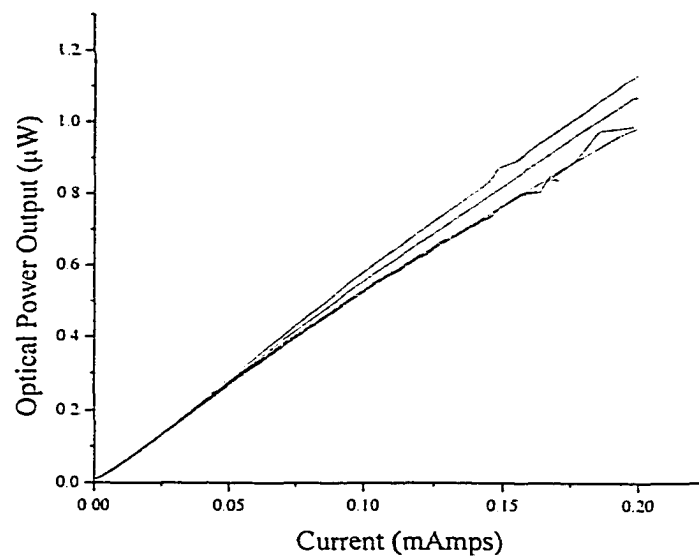


Figure D-5 Light output vs. current for Znq₂.

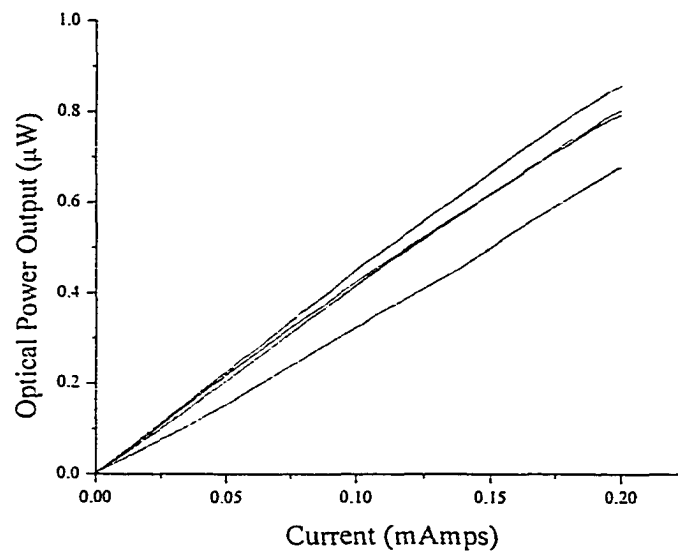


Figure D-6 Light output vs. current for 2Meq₂Zn.

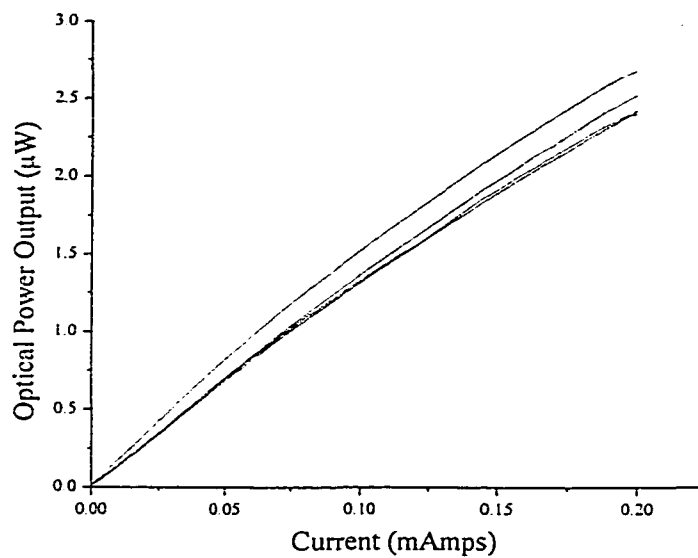


Figure D-7 Light Output vs. current for 4Meq₂Zn.

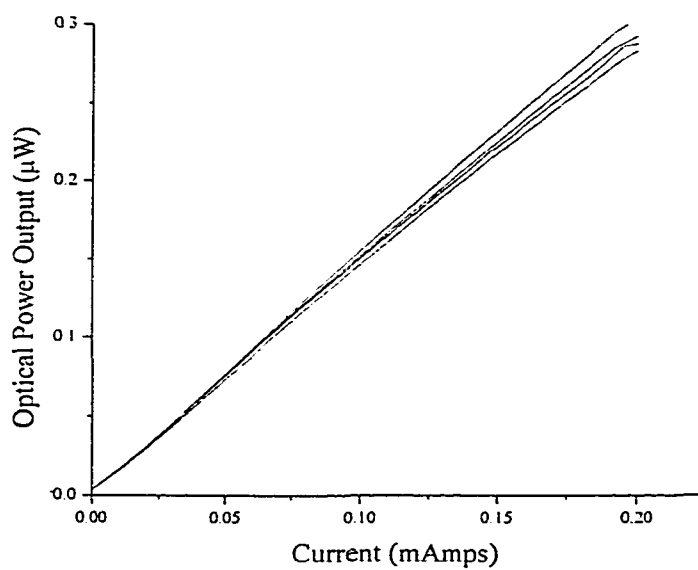


Figure D-8 Light output vs. current for 5Meq₂Zn.

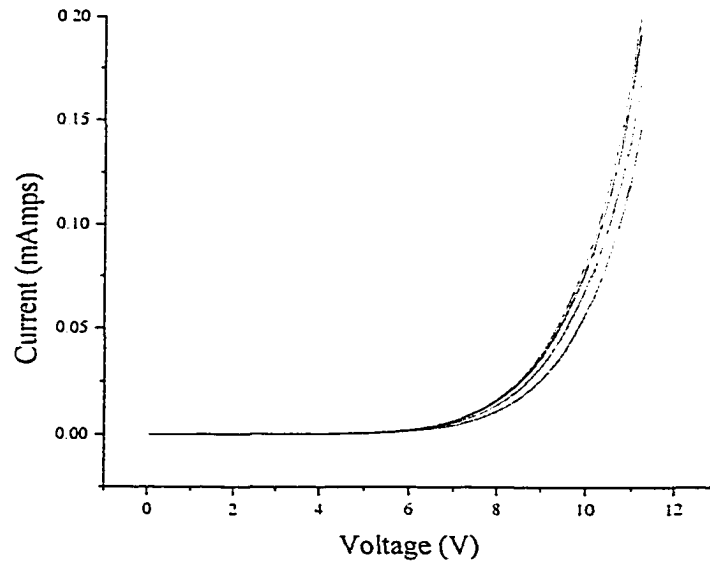


Figure D-9 IV curve for Alq₃.

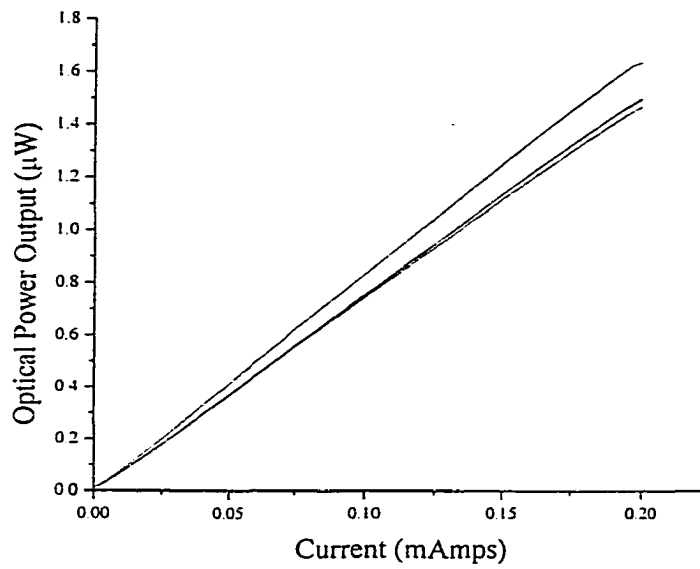


Figure D-10 Light output vs. current for Alq₃.

APPENDIX V

 ^1H NMR DATA

Table E-1. ^1H NMR Chemical shifts in ppm and Coupling Constants for nMeq and nMeqLi in DMSO- d_6 .

Sample	δH2 (ppm)	δH3 (ppm)	δH4 (ppm)	δH5 (ppm)	δH6 (ppm)	δH7 (ppm)	δCH_3 (ppm)
q	8.91 (dd) [J2,3=4.1] [J2,4=2.0]	7.59 (dd) [J3,2=4.1] [J3,4=1.7]	8.36 (dd) [J4,3=8.3] [J3,2=1.6]	7.45 (dd) [J5,6=8.2] [J5,7=1.4]	7.50 (m) [J6,5=8.2]	7.19 (dd) [J7,6=7.5] [J7,5=1.4]	
Liq	8.45 (dd) [J2,3=4.2]	7.30 (m) [J3,4=8.2]	8.07 (dd) [J4,3=8.2]	6.62 (d) [J5,6=7.9]	7.20 (d) [J6,5=7.9]	6.54 (d) [J7,6=7.8]	
4Meq	8.31 (d) [J2,3=3.7]	7.15 (d) [J3,2=3.7]	-----	6.68 (d) [J5,6=7.6]	7.20 (t)	6.54 (d) [J7,6=?]	2.53 (s)
4MeqLi	8.71 (d) [J2,3=4.3]	7.41 (d) [J3,4=4.3]	-----	7.49 (d) [J5,6=8.4]	7.48 (m) [J6,5=8.4]	7.10 (dd) [J7,6=6.8]	2.66 (s)
5Meq	8.87 (dd) [J2,3=4.1]	7.60 (dd) [J3,4=8.5]	8.40(dd) [J4,3=8.5]	-----	7.28 (d) [J6,7=7.7]	6.99 (d) [J7,6=7.7]	2.54 (s)
5MeqLi	8.44 (dd) [J2,3=3.8]	7.34 (m) [J3,4=8.4] [J3,2=4.2]	8.14 (dd) [J4,3=8.4]	-----	7.01 (d) [J6,5=7.9]	6.35 (dd) [J7,6=7.8]	2.38 (s)

Table E-2. ^1H NMR Chemical shifts in ppm and Coupling Constants for q and Liq in CDCl_3 .

Sample	δH2 (ppm)	δH3 (ppm)	δH4 (ppm)	δH5 (ppm)	δH6 (ppm)	δH7 (ppm)
q	8.78 (dd) [J3,2=3.0]	7.38 (dd) [J2,3=8.3]	8.10 (dd) [J4,3=8.3]	7.30 (dd) [J6,5=8.2]	7.44 (m) [J7,6=7.9]	7.21(dd) [J7,6=7.9]
Liq	8.45 (dd) [J2,3=4.2]	7.30 (m) [J3,4=8.2]	8.07 (dd) [J4,3=8.2]	6.62 (d) [J5,6=7.9]	7.20 (d) [J6,5=7.9]	6.54 (d) [J7,6=7.8]

VITA

Graduate College
University of Nevada, Las Vegas

Floerfida Lalo Endrino

Address:

5125 Gray Lane # B
Las Vegas, NV 89119

Degrees:

Bachelor of Science, Chemistry, May 1999 University of Nevada, Las Vegas
Bachelor of Science, Biology, May 1999 University of Nevada, Las Vegas

Publications:

L. S. Sapochak, A. Padmaperuma, N. Washton, F. Endrino, G. Schmett, J. Marshall and D. Fogarty, P. Burrows and S. R. Forrest, "Effects of Systematic Methyl-Substitution of Metal (III) Tris (8-Hydroxy-n-Methylquinoline) Chelates on Material Properties for Optimum Electroluminescence Device Performance," J. Am. Chem. Soc., 2001, submitted.

F. Endrino, L. Sapochak, S. Nanayakkara, N. Washton, J. Marshall and D. Fogarty, "Effects of Coordination Number and Geometry on the Electroluminescence Properties of Metal Quinolate Chelates," Chapter in Molecules as a Component of Electronic Materials, American Chemical Society, book 2001, submitted.

Presentations:

F. Endrino, L. Sapochak, S. Nanayakkara, N. Washton, J. Marshall and D. Fogarty, "Effects of Coordination Number and Geometry on the Electroluminescence Properties of Metal Quinolate Chelates," American Chemical Society, April 2001, San Diego, CA

F. Endrino, G. Schmett, N. Washton, A. Padmaperuma, J. Marshall, and L. Sapochak. Modified Bis-Quinolate Metal Chelates for Electroluminescence Applications. 1999, MRS Fall Meeting, Boston, MA

Thesis Title: Comparative Study of Zinc Bis-Quinolates and Lithium Mono-Quinolates: Investigation of the Effect of Coordination Geometry on Electroluminescence Performance

Thesis Examination Committee:

Chairperson, Dr. Linda S. Sapochak, Ph.D.
Committee Member, Dr. Lydia McKinstry, Ph.D.
Committee Member, Dr. Dave Hatchett, Ph.D.
Graduate College Representative, Dr. Malcolm Nicol, Ph.D.